Assimilation and Forecast Studies on Localized Heavy Rainfall Events Using a Cloud-Resolving 4-Dimensional Variational Data Assimilation System

Takuya Kawabata

Acknowledgements

Abstract

A prototype system of a nonhydrostatic 4-dimensional variational assimilation system (4D-Var) based on the Japan Meteorological Agency (JMA) nonhydrostatic model (JMA-NHM; Saito et al. 2006; 2007; 2012) was made by the development team in the JMA and the Meteorological Research Institute (Honda et al. 2003; Kawabata et al. 2003). For investigating structures of meso convective systems (MCSs) and improving their predictability, this system is subsequently enhanced to a cloud-resolving 4D-Var (NHM-4DVAR) which includes perturbations to water vapor and cloud microphysical variables with new observation operators. This improvement has been done almost by the author (Kawabata et al. 2007; 2011; 2013). In this thesis, the developments of NHM-4DVAR and three case studies with NHM-4DVAR are described.

The first version of NHM-4DVAR (v1) considers perturbations only to the dynamical framework and the advection of water vapor. The second version of NHM-4DVAR (v2) is advanced to consider perturbations to clouds and rainwater. Not only are the tangent linear and adjoint models developed, but the control variables are also extended to water materials. Assimilation for the Doppler radial wind, Global Positioning System (GPS) precipitable water vapor (PWV), and surface observations are implemented in NHM-4DVAR v1, and the direct assimilation method of radar reflectivity is implemented in NHM-4DVAR (v2). Finally, the observation operator of the GPS slant total delay data (GPS-STD) is added. NHM-4DVAR is the first 4D-Var system in the world i) based on a full nonhydrostatic model, ii) with a high horizontal resolution of 2 km, iii) equipped with many kinds of observation operators for remote-sensing observation networks. This system was applied to three case studies, and the initiation and sustainment mechanisms of MCSs on meso β-γ scales are investigated. Through these case studies, predictability of meso β-γ MCSs is discussed.

In the first case study, NHM-4DVAR v1 is applied to the heavy rainfall event induced by an isolated MCS and observed at Nerima, in the northern part of the Tokyo metropolitan area, on 21 July 1999. Doppler radar radial wind data, GPS-PWV data, and surface temperature and wind data are assimilated in the initiation stage of the MCS. The meso-γ scale MCS is reproduced well in the assimilation and subsequent forecast with respect to time sequence of 10-minute rainfall amount and radar reflectivity distribution. This success is provided by assimilating horizontal wind observation observed by Doppler radars (low-level wind convergence) and water vapor observation by GPS before the initiation of the MCS. The result first shows that it is possible for MCSs even in a meso β-γ scale to be predicted with accurate intensity, occurrence time and location, when preferable conditions are assimilated before convection initiation.

Using NHM-4DVAR v2, the effect of assimilating rain water is investigated through single-observation assimilation experiments for isolated deep convection using pseudo-observations.

The results show that assimilating rainwater in a convection-free area is more difficult to interpret because the assimilation alone cannot maintain convection for long periods due to nonlinearity. Furthermore, an assimilation experiment using actual observations of a local heavy rainfall in the Tokyo metropolitan area is conducted. In this experiment, GPS-PWV data, surface and wind profiler data, Doppler radial wind and radar-reflectivity data are assimilated. The 4D-Var assimilation reproduced a line-shaped rainband whose shape and intensity are consistent with those of the observation. Assimilation of the radar-reflectivity data intensified the rainband, suppressed false convection, and improved the quantitative precipitation forecast skill. The simulated rainband lasted for 1 h in the extended forecast, and then gradually decayed. Sustaining the low-level convergence produced by northerly winds in the western part of the rainband is key to prolonging the predictability of the convective system. After the single and actual observation experiments, and the incremental method experiment, it is concluded that assimilating rain water has difficulty to improve forecasting the long-lasting MCSs due to nonlinearity. This means that observing and assimilating environmental information outside MCSs are more important to extend predictability of MCSs.

In order to advance environmental observation assimilation, a method to assimilate GPS-STD is developed and applies to a line-shaped local heavy rainfall event that formed on 19 August 2009 over Okinawa Island, Japan. The GPS-STD assimilation significantly improves the water vapor and temperature fields over a wide area and yields a clearly improved forecast in terms of both rainfall timing and intensity. This result shows that assimilating environmental information has capability to improve predictability of MCSs.

These three studies clarify that i) MCSs are initiated by low-level-wind convergence with moist air over a horizontal scale of approximately 50 km, and ii) predictability of meso β-γ MCSs depends on assimilating observations of wind, humidity, and temperature observations on a 50×50 km area around the MCS at low levels. Assimilating rain water inside cumulonimbus has limitation to expand the MCS's predictability. After these discussions, innovative observations and preferred assimilation systems are proposed.

Contents

List of Figures

xiii

List of Tables

Acronyms and Abbreviations

Acronym	Abbreviation
3(4)D-Var	3(4)-Dimensional Variational Data Assimilation
AMeDAS	Automated Meteorological Data Acquisition System
ECMWF	European Centre for Medium-Range Weather Forecasts
EnKF	Ensemble Kalman Filter
GSI	Geospatial Information Authority of Japan
GEONET	GPS Earth Observation NETwork
GPS	Global Positioning System
JMA	Japan Meteorological Agency
JMA-NHM	Japan Meteorological Agency Nonhydrostatic Model
JNoVA	JMA operational mesoscale Nonhydrostatic four-dimensional Variational Assimilation system
JST	Japan Standard Time: UTC + 9 h
KF	Kalman Filter
MCS	Mesoscale Convective System
Meso-4DVAR	JMA mesoscale 4D-Var system
MM5	Penn State/NCAR (National Center for Atmospheric Research) Mesoscale Model version 5
NMC	National Meteorological Center
NWP	Numerical Weather Prediction
OI	Optimal Interpolation
PWV	Precipitable Water Vapor
QPF	Quantitative Precipitation Forecast
RW	Radial Wind
STD	Slant Total Delay
UTC	Universal Time Co-ordinated
VDRAS	Variational Doppler Radar Analysis System
WRF	Weather Research and Forecasting Model
ZTD	Zenith Total Delay

Chapter 1

General Introduction

In this chapter, a brief history of data assimilation is introduced. In order to realize the progress of data assimilation, a historical forecast of a super-typhoon in 1959 is reviewed, and compared with a forecast of the same typhoon with a state-of-the-art numerical weather prediction (NWP) system. Then, the challenges, even for the state-of-the-art NWP system, to forecast localized mesoscale convective systems are described, and the demand for high-resolution assimilation with high-density observation network is discussed. Finally, the scope of this thesis is illustrated, and the prospect and structure are described.

1.1 Brief history of data assimilation

The first attempt of numerical weather prediction (NWP) was conducted by Richardson (1922). He collected upper-air observations at several observation sites, smoothed them subjectively, and listed them in a table (Fig. 1.1). Using these values as the initial condition for basic meteorological equations, he calculated the atmospheric status after 6 h manually. This work is of supreme importance, because his idea is essentially correct for weather prediction and his trial has been advanced until present day. Unfortunately, he only obtained an unrealistic surface pressure trend: 145 hPa increased over 6 h. This failure was due to noisy initial conditions and the lack of a suppression procedure for short waves in his equations. This problem is known today as the initialization problem. The initialization problem has been solved using different techniques from data assimilation and is currently unified into the data assimilation scheme. Lynch (2006) discussed initialization methods and Richardson's problem in detail. The success of NWP has been called 'Richardson's dream'.

Charney et al. (1950) conducted the first computerized NWP and succeeded in making a 24-h forecast. They had recognized the problem of high-frequency waves (short waves) and eliminated them from their model (the barotropic vorticity equation). This treatment is called the filtering method. The initial conditions were determined in the same manner as Richardson (1922), but they assumed that the noise was smoothed in the model integration, commenting that "an objective analy-

sis would have been preferable". The method for their initial condition, in which a human read a weather map and determined meteorological values, is called 'subjective analysis'; in contrast, objective analysis mathematically provides an initial condition to NWP.

The first generation of objective analysis utilized function-fitting method proposed by Panofsky (1949) and Gilchrist and Cressman (1954). In this approach, observed values are fitted to regularly spaced model grid points using smoothing functions. Atmospheric states are represented by basis functions, and expansion coefficients are determined by square-root fitting using observations. The Japan Meteorological Agency (JMA) used the function fitting in the upper stratosphere analysis until 2001 (Murakami 1997).

The second generation of objective analysis utilized the successive correction method proposed by Bergthorsson and Doos (1955). This method adopts an iterative approach. The first guess or background fields (e.g., previous forecast results and climatological values) are provided first, and then they are corrected using observed values with proper weights. The correction is conducted iteratively reducing the radius of the corrected area. Because this method uses first-guess fields, it may be called 'data assimilation'. Furthermore, it is possible to conduct forecast and analysis steps in turn (an analysis-forecast cycle), as Gilchrist and Cressman (1954) discussed. JMA has used this method in troposphere analysis since the beginning of NWP at JMA, in 1959 (JMA 1968).

Important aspects of data assimilation (e.g., analysis-forecast cycle, handling multivariate relationships) exist both in the successive correction method and the optimal interpolation (OI) method, which is often referred to as 'statistical interpolation'. The weights used in the successive correction method are empirically determined, whereas the weights (errors) in OI are given based on minimum
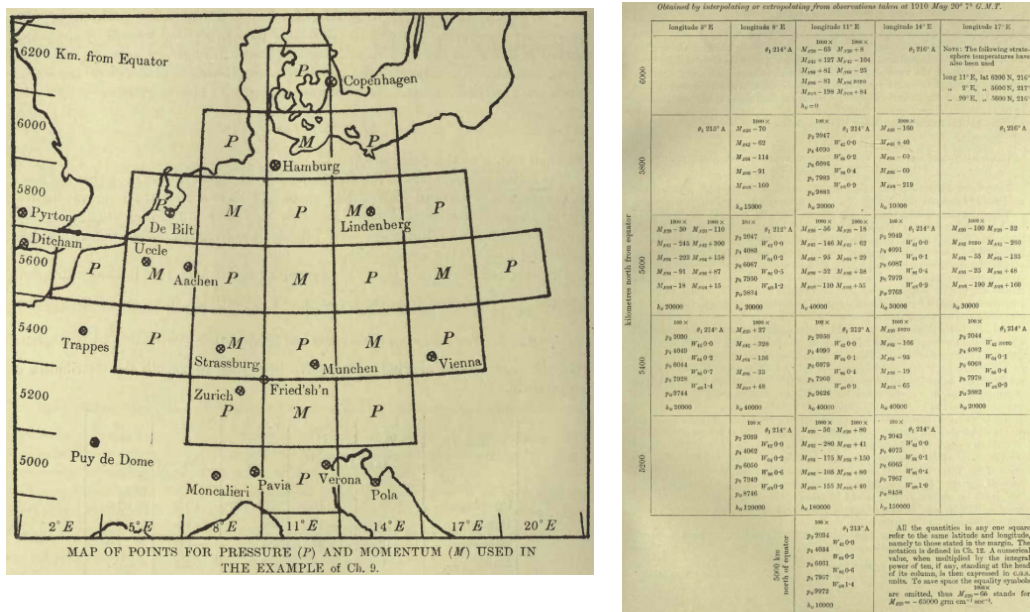
Fig. 1.1. Observation sites and model grid points (left) and the smoothed initial values (right) after pages 184 and 185 of Richardson (1922).

2

variance estimation theory (Eliassen 1954; Gandin 1963). In this means, OI is called as 'data assimilation' in a true sense. OI was expanded to three dimensions (Lorenc 1981), and applied to multivariate analysis using geostrophic balance. These expansion led to be widely used at operational NWP centers throughout the 1970s and 80s. JMA began to operate OI in troposphere analysis in 1982 (Kashiwagi 1983).

Implementation of variational method (Var) to objective analysis was first studied by Sasaki (1958). The Var enabled observations which are not directly related to model prognostic variables to be assimilated. He later expanded the method to four dimensions (4D-Var; Sasaki 1970). The most important advantages of 4D-Var are the time evolution of the background error covariance and consideration of the model-predicted trajectory using tangent linear and adjoint models of a nonlinear forward numerical model. However, since this calculation requires huge computational resources, 4D-Var could not be implemented into meteorology until proposals of adjoint methods (Lions 1971; Marchuk 1975a; 1975b). A detailed description of Sasaki's work is given in Lewis (2009). In 1991, the National Meteorological Center (NMC) in the U.S.A. installed a 3-dimensional variational data assimilation system (3D-Var) into their operational global prediction system (Parrish and Derber 1992). The European Centre for Medium-Range Weather Forecasts (ECMWF) implemented the global 4D-Var system in 1997, and the JMA started to operate the first regional 4D-Var in the world in 2002. A detailed algorithm of the variational method will be given in Section 2.1.

Since the 1990s, data assimilation methods based on the Kalman filter (KF; Kalman 1960) have been extensively studied. The KF basically requires huge computational resources, since the background error covariance is explicitly predicted in this method. However, Evensen (1994) showed that the KF algorithm could be well approximated using limited number of ensemble forecasts (Ensemble Kalman Filter: EnKF), which greatly lessened the computational burden. After his work, several kinds of ensemble-based KF techniques have been developed. The square root filter (SRF) developed by Andrews (1968) is an especially important technique for the expansion of the EnKF. Whitaker and Hamill (2002) is the first application of the SRF to meteorology (Serial Ensemble Square Root Filter). This technique has been expanded to the Ensemble Transform Kalman Filter (Bishop et al. 2001), the Local Ensemble Kalman Filter (Ott et al. 2004), and the Local Ensemble Transform Kalman Filter (Hunt et al. 2004). Currently, EnKF techniques are actively studied and compared to variational methods. Detailed information is given in the special collection of the Monthly Weather Review of the American Meteorological Society "Intercomparisons of 4D-Variational Assimilation and the Ensemble Kalman Filter" (Mitchell 2012).

The ensemble-based variational data assimilation (EnVar) method was recently proposed by Lorenc (2003) and Zupanski (2005). Because this method approximates the gradient of the cost function in the variational method using ensemble forecasts, we can use variational schemes without using adjoint models. Other variational methods using ensemble forecasts have been proposed by

Hamill and Snyder (2000), Lorenc (2003), and Buehner (2005). In their methods, background error covariance is estimated using ensemble forecasts and is merged with statistical covariance. This idea provides flow dependency of meteorological fields into the statistical background error covariance of the variational method.

Currently, data assimilation methods after the Var are called 'advanced data assimilation', because they consider time evolution of the model dynamics and the background error covariance. The former evolution enables assimilation systems to treat properly observation data which observe mesoscale convective systems (MCSs) varying drastically in time. And also nonlinearity of MCSs can be considered using numerical models in the assimilation procedures. Since each MCS is quite different on their structures, these are unable to be represented statistically. Therefore, the background error should not only statistically represented but with flow dependency. The latter, the background error covariance, evolution enables to introduce flow-dependency to the assimilation result. Considering these factors, assimilation systems for MCS forecasting should adopt the advanced data assimilation methods, and the assimilation system described in this thesis is belonging to this generation.

The reader can obtain a detailed description of data assimilation history and theory in Daley (1991), Swinbank et al. (2003), Kalnay (2003), Tsuyuki and Kawabata (2008), and Park and Xu (2009), and so on.

1.2 Examples of forecasts on a historical event, in 1959 or using a current NWP system

1.2.1 A typhoon forecast 50 years ago

In order to realize the progress of NWP systems, the operational forecast on Typhoon Vera in 1959 is reviewed in this subsection and then the forecast using a current NWP system on the same typhoon is described in the next subsection after Kawabata et al. (2012) which the author contributed as the leading author.

Typhoon Vera struck Japan on 26 September 1959 and 5098 were people missed or dead. Vera was one of the strongest tropical cyclones (TC) in recorded history, achieving a minimum sea level pressure of 895 hPa and a maximum sustained wind speed of 70 m s^{-1}. The observed central pressure near the landfall position was 929 hPa. A tide level of 3.89 m was measured at Nagoya Port. This is still the record in Japan at the time of this writing. Vera caused a large storm surge and a terrible disaster in the Ise Bay area (Ise-wan in Japanese) and is thus known in Japan as the Isewan Typhoon. The loss of life from Vera is by far the largest due to a meteorological disaster in the past 60 years.

JMA introduced a large computer system in 1959 and started numerical weather predictions. This was the third operational NWP center in the world. In their operational forecasting procedure for Vera at that time, two tracks from empirical methods, three from numerical models, and one from

a forecaster were drawn on a weather map that was updated twice a day (0900 and 2100 JST; Japan Standard Time: UTC + 9 h). Only the track of the typhoon, not its speed, was forecasted. As a matter of course, the initial conditions were very poor for the three models. One model was initialized with the successive correction method of the first generation of data assimilation methods (see Section 1.1). The other two models were run with a steering current, hence, these simulations were close to ideal numerical experiment. In spite of these insufficient initial conditions, the landfall positions predicted by those models were scattered around the Kii Peninsula (Fig. 1.2). The shaded area in Fig. 1.2 represents the final forecasted track drawn from the five total forecast tracks. That is, the area illustrates the probability of various typhoon directions by a 'handmade ensemble forecast'.

1.2.2 A typhoon forecast with a current NWP system

Kawabata et al. (2012) applied a state-of-the-art NWP system to Typhoon Vera. They conducted a numerical experiment with almost the same initial conditions as the JMA operational mesoscale pre-diction system. The forecast model is the JMA mesoscale nonhydrostatic model (JMA-NHM; Saito et al. 2006; 2007; 2012) with 5-km horizontal grid spacing and a cumulus parameterization scheme (hereafter NHM-5km), and the assimilation system is the JMA operational mesoscale nonhydrostatic four-dimensional variational assimilation system (JNoVA; Honda and Sawada 2009) with 15-km horizontal grid spacing. Observation data assimilated in the experiment were surface, shipboard, up-
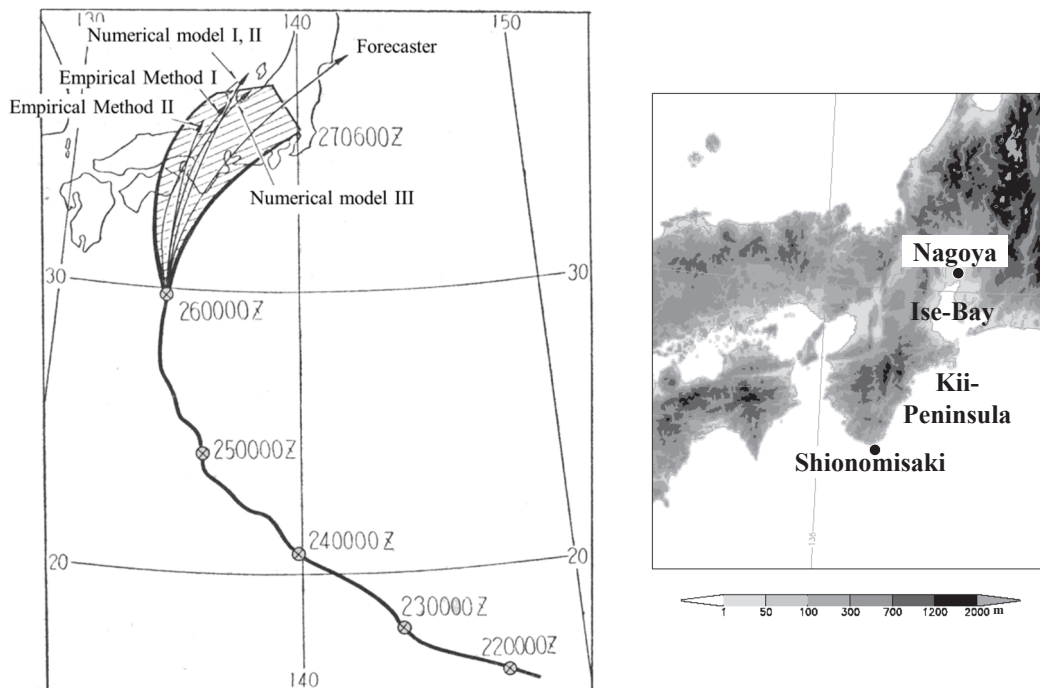
Fig. 1.2. The 24-h forecast of Typhoon Vera's track (left) at 0900 JST 26 September 1959, deter-mined at 1500 JST. Arrows show the track predictions by empirical methods, numerical models, and a forecaster. The dashed gray line illustrates the best track. The shaded area shows the final decision of Vera's track forecast by JMA (modified Fig. 7.1.7 in JMA (1961)). A map (right) of the geographic names in this chapter.

per-air sounding, dropsonde, and aircraft observations. After eight time assimilations with 3-hour windows, a 36-h forecast from 0900 JST on 26th to 2100 JST on 27th September was produced. A storm surge forecast was also made using the Princeton Ocean Model (POM; Blumberg and Mellor 1987) with 2-min horizontal grid spacing.

The horizontal scale and the location of the typhoon and a high-pressure system are similar to the surface weather map at 0900 JST on 26 September (Fig. 1.3a). In the pseudo-satellite image, the eye of the typhoon (Fig. 1.3a) and the outer rainbands (Fig. 1.3b) agree with the observations. Moreover, the cloudy and rainy weather distributions in the surface weather map are almost the same as the distribution of clouds in the pseudo-satellite image (Fig. 1.3a and b). The stationary front on the surface weather map can be seen as a cloud band in the pseudo-satellite image (Fig. 1.3b). Figure 1.2 gives us only information on the typhoon track forecast, while Figure 1.3 gives the forecasts of the track, intensity, and rainfall distribution. This contrast emblematizes NWP developments compared with the forecast 50 years ago.

The storm surge forecast with POM is compared with the observation at Nagoya Port (N35.1, E136.9). The maximum tide levels of 3.89 m (observed) and 3.52 m (POM result) (Fig. 1.4) occur at 2135 JST (observed) and 2120 JST (POM result) on 26 September. The time difference is a mere 15 min. The time series (Fig. 1.4) indicate that observed and modeled tide levels evolve similarly. From these results, we can understand that NWP systems have been added several kind of model such as ocean models further to atmospheric models and their predictable factors have been expanded in last 50 years.

Since 1945, the loss of human life from weather events has decreased, mainly owing to advances in civil engineering and weather-prediction technologies. Meteorology has contributed to disaster prevention by providing quantitative, highly accurate predictions for precipitation, wind speed, and storm surges. As reviewed above, horizontal distributions of many kinds of factors have been able to be forecasted in these times, due to development of various numerical models. In addition, the forecasts have become more and more accurate in time and location due to development of data assimilation techniques. In the Typhoon Vera case, when the assimilation system was eliminated from the experiment, the forecast became worse (not shown). As reviewed in section 1.1, the data assimilation techniques have been highly advanced and the importance of the initial condition problems has been increasing in a last few decades in current meteorology.

6

(a) 1959.09.26　09 JST (FT=00)
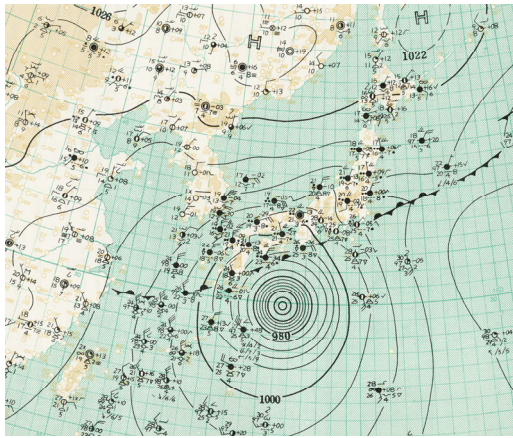
(b) 1959.09.26　21 JST (FT=12)
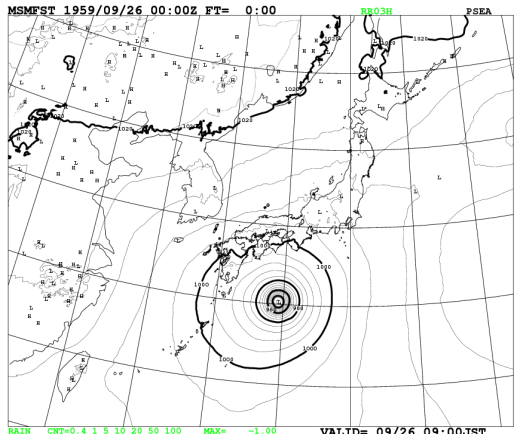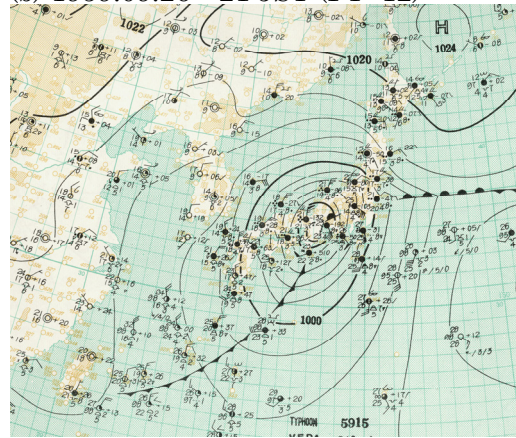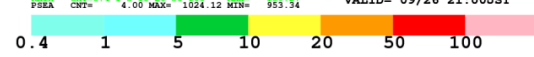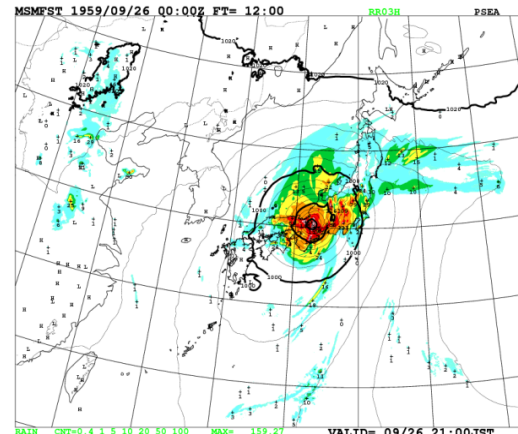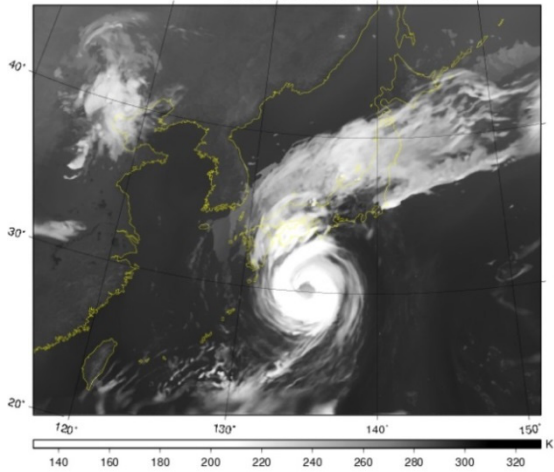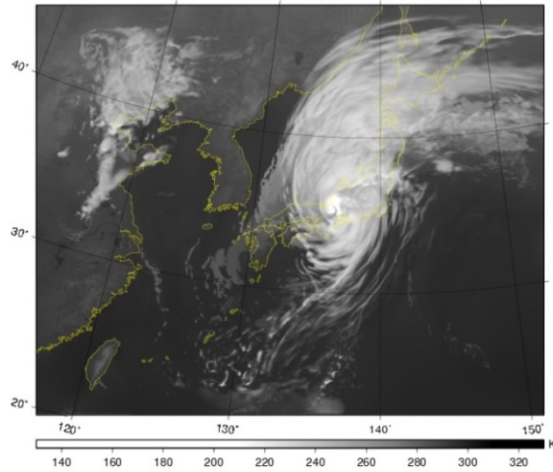
Fig. 1.3. Surface weather maps analyzed by JMA (upper), sea level pressure and 3-h accumulated rainfall amount distributions of NHM-5km (middle), and simulated pseudo-satellite images (lower). Figures in the left column are at 0900 JST, 26 September, 1959, and those in the right column are at 2100 JST. Pseudo-satellite images were made by simulating infrared images from a geostationary satellite using a radiative transfer model (Owada 2006).
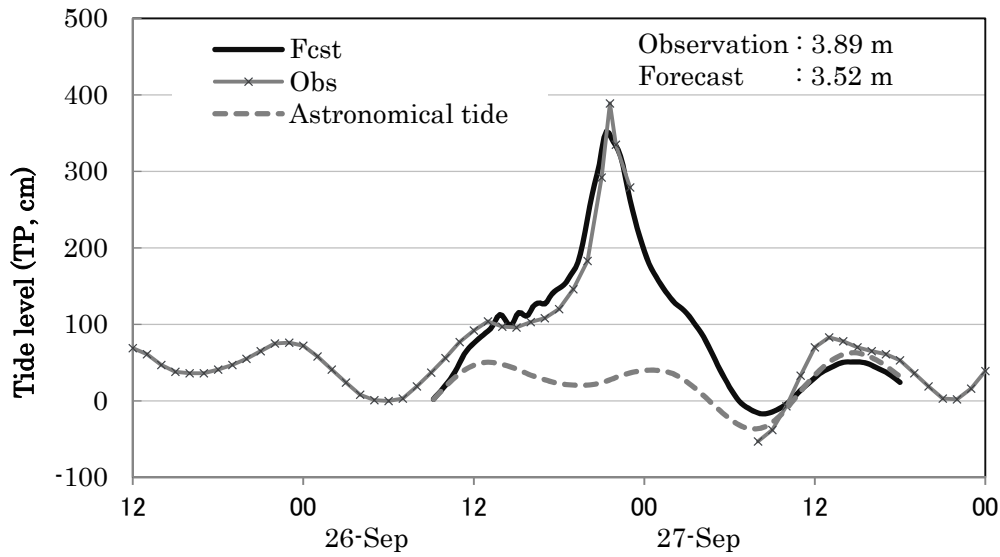
Fig. 1.4. Time sequence of tide levels from observations and the POM forecast. The maximum observed (3.89 m) and forecasted (3.52 m) values are shown in each sequence. Observations from 0000 to 0700 JST are missing.

1.3 Towards localized heavy rainfall forecasts with advanced data assimilation systems

Heavy rainfall is an extreme meteorological phenomenon that often causes fatal disasters. Recent progress in numerical modeling and assimilation techniques has made it possible to predict to a large extent the occurrence of heavy rainfall events induced by strong forcing such as large-scale oro-graphic or synoptic forcing, or typhoons as described in Section 1.2. Figure 1.5 shows a time series of the Quantitative Precipitation Forecast (QPF) performance of the JMA operational mesoscale NWP system using a small (10 km) verification grid. It shows that the QPF of low-intensity rainfall (1 mm 3 h^{-1}) has been improved over the last decade (red lines in Fig. 1.5), whereas the QPF of high-intensity rainfall (20 mm 3 h^{-1}) has not (blue lines in Fig. 1.5). Therefore, it can be said that prediction of localized heavy rainfall events is still a challenge to NWP. So far, localized heavy rain-fall events are primarily forecast using kinematic methods based on temporal extrapolation of radar observations, but such methods have limited accuracy beyond a relatively short timeframe. Thus, dynamical forecasting of localized heavy rainfall events using numerical models is desired.

A primary reason for the difficulty in predicting localized heavy rainfall events is the small size, in both time and space, of MCSs. Conventional observations (e.g. aerological soundings) are unable to capture phenomena at the typical spatial (10 km) and temporal (1 h) scales of deep convection, and it is therefore necessary to use remote sensing technologies to capture the structure of localized heavy rainfall. Furthermore, such remote sensing instruments measuring key factors of MCSs such as wind, temperature, and humidity have to be widely installed and require frequent operation. Suit-

8

able observational instruments for MCSs are therefore Doppler radar, surface observations, and Global Positioning Systems (GPS).

Thunderstorms with a horizontal scale of 10–20 km are often observed over the Kanto Plain in central Japan during the summer. A previous statistical study (Fujibe 2002) noted that thunderstorms form and develop over the surface wind convergence zone between easterly and southerly winds over the Kanto Plain. JMA has deployed a Doppler radar network and a surface observation network, the Automated Meteorological Data Acquisition System (AMeDAS). AMeDAS obtains a mean horizontal resolution of approximately 20 km over Japan. These observations provide measurement of low-level wind and temperature fields. In addition, the Geospatial Information Authority of Japan (GSI) operates the GPS Earth Observation NETwork (GEONET), which covers all of the Japanese Islands at the same resolution. GPS data provides water vapor, temperature, and pressure information. Use of these instruments enables detection of wind convergence with moist air and initiated convection.

Another factor increasing the difficulty of providing accurate predictions is that deep convection is initiated in an unstable atmosphere, and its evolution is very sensitive to small perturbations in the initial conditions of NWP; that is, it exhibits the characteristics of a chaotic system. To reduce the chaoticity, atmospheric condition has to be predicted more precisely using sophisticated NWP models employing cloud microphysics and other physics systems. Moreover, the prediction has to originate from precisely defined initial conditions. Therefore, advanced data assimilation systems with spatially and temporally dense observations are needed.
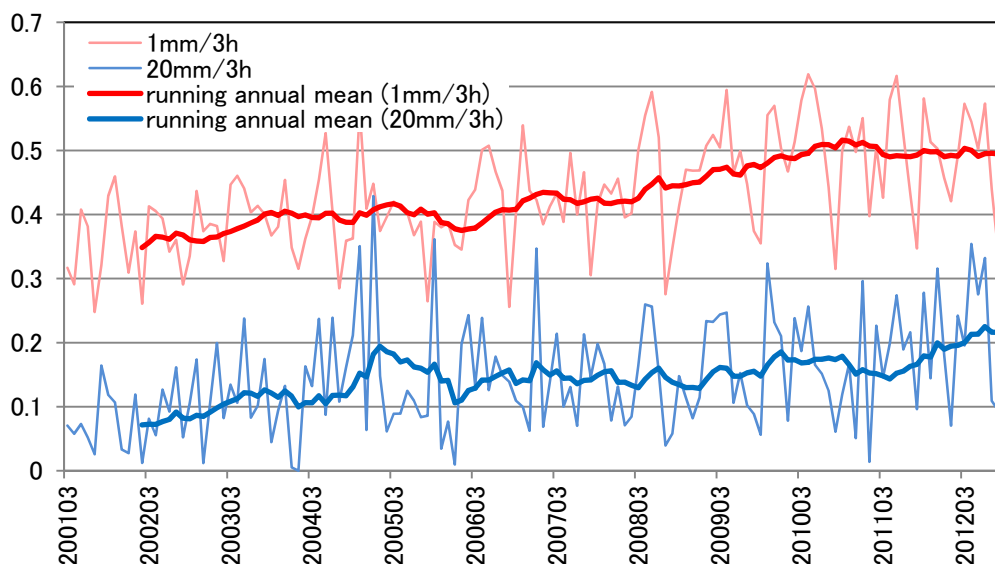
Fig. 1.5. Time series of rainfall forecast skills of the JMA mesoscale NWP system. Threat scores with 10 km verification grid for rainfall intensities of 1 mm 3 h^{-1} (thin red line), 20 mm 3 h^{-1} (thin blue line), one year running means of 1 mm 3 h^{-1} (thick red line), and 20 mm 3 h^{-1} (thick blue line).

Many studies have been conducted to investigate MCSs using non-hydrostatic models with cloud microphysics (e.g., Chang and Yoshizaki 1991; Kato 1998; Minda et al. 2010). These studies were concerned with the characteristics or structures of the MCSs, and did not discuss the timing and locations of the simulated MCSs in detail. Furthermore, downscaled initial conditions are generally not adequate to forecast the locations and timing of the MCSs, and data assimilation techniques are needed to improve them.

Data assimilation techniques connect observations with numerical models. One sophisticated assimilation method is the four-dimensional variational assimilation method (4D-Var), which is able to take the model trajectory into account across an assimilation window. In a pioneering work of mesoscale data assimilation, Zou and Kuo (1996) implemented 4D-Var in a mesoscale numerical model. They developed their 4D-Var based on the Penn State/NCAR (National Center for Atmospheric Research) Mesoscale Model version 5 (MM5; Dudhia 1993) with a horizontal grid spacing of 40 km. The JMA began using the mesoscale 4D-Var system (Meso-4DVAR; Koizumi et al. 2005) in 2002, the first operational regional 4D-Var system in the world, using a horizontal grid spacing of 20 km. In 2009, Meso-4DVAR was replaced with a new 4D-Var system, the JMA Non-hydrostatic Model-based Variational Data Assimilation System (JNoVA; Honda and Sawada 2009). JNoVA is based on non-hydrostatic dynamics and has a horizontal grid spacing of 15 km. The UK Met Office has also been operating a mesoscale 4D-Var system, but with a horizontal grid spacing of 24 km. Huang et al. (2009) developed the WRF (Weather Research and Forecasting Model)-4DVAR with a horizontal resolution of 45 km. Recently, Wang et al. (2013) have improved it to include cloud microphysics (warm rain processes) with a 4 km grid spacing. Gustafsson et al. (2012) developed the HIRLAM 4D-Var system with a 40 km grid spacing.

Non-hydrostatic models are used in almost all of these systems, but their resolutions are not sufficient to reproduce localized heavy rainfall events. In many cases, a higher horizontal resolution is necessary to reproduce such events; Kato and Aranami (2005) showed that a horizontal grid spacing of 1.5 km (storm scale), with the ability to explicitly resolve cumulonimbus, was sufficient to reproduce the Niigata-Fukushima heavy rainfall case in 2004, but a 5 km spacing was not. The clouds in the model must be represented by a microphysical scheme, and including the non-hydrostatic effect is essential for modelling heavy rainfall phenomena caused by deep convection. It is clear that a non-hydrostatic 4D-Var system at storm scale is needed to reproduce thunderstorms.

The only previous example of a storm-scale 4D-Var is the VDRAS (variational Doppler radar analysis system; Sun and Crook 1997), which was developed to retrieve the 3-dimensional dynamic field and cloud microphysics field from Doppler radar data. The VDRAS has a resolution of about 2 km, and was applied to a supercell storm case (Sun 2005), but its nonlinear model adopts an anelastic dynamical framework and simplified cloud microphysical processes. This means that the model

can't be employed for regions with complex terrain, and is at a disadvantage in realistic simulations. In addition, no observations except Doppler radar are assimilated into the VDRAS.

Due to lack of a storm-scale 4D-Var with suitable observations for MCSs at a meso β-γ scale, it has not yet been determined whether such small-scale MCSs can be predicted. Sophisticated numerical models with detailed cloud microphysics and other physics, remote sensing observation networks, and an advanced data assimilation system at a storm-scale are required for investigating the structure of MCSs and improving their predictability.

1.4 Scope and structure of this thesis

As described above, an advanced data assimilation system with a storm-scale resolution should be developed for investigating mechanisms of small-scale MCSs and improving predictability of MCSs. However, the intrinsic nonlinearity of MCSs and the associated numerical models is an important issue in this development process. A 4D-Var system with a simple framework based on JMA-NHM, called the 'NHM-4DVAR', was developed for tackling this nonlinearity, and has subsequently been advanced further. NHM-4DVAR with simple dynamics (dry dynamics and water vapor advection) was developed first, and warm-rain cloud microphysics were included later. The assimilation of GPS-derived water vapor observations was first implemented by the assimilation of precipitable water vapor observations and then advanced to include the assimilation of GPS slant total delay observations. Assimilation of Doppler radar observations was originally based on the assimilation of radial wind observations and later of radar reflectivity. Improvements in the predictability of MCSs were confirmed in three case studies which investigated the mechanisms of MCSs with a particular focus on convection initiation. Major attention was given to water vapor, temperature, and wind structures at low altitude.

In the first case study, a version of NHM-4DVAR that considered perturbations to water vapor advection in the adjoint model was developed (hereafter NHM-4DVAR v1). Observation operators of radial wind (RW) by Doppler radar, precipitable water vapor derived from GPS (GPS-PWV), and surface observations were developed. NHM-4DVAR v1 was then applied to a heavy rainfall event in the north of Tokyo on 21 July 1999 (hereafter the Nerima heavy rainfall event; Kawabata et al. 2007). This case study focuses on two subjects: forecasting an isolated thunderstorm with accurate location and timing, and clarifying the lifecycle of the thunderstorm.

In the second case study, a warm rain process was added to the adjoint model of NHM-4DVAR v1 (hereafter NHM-4DVAR v2), and an observation operator for radar reflectivity was developed. Radar observations provide very useful information for high-resolution assimilation systems, because radars are deployed to cover the whole area of the Japanese Islands and can capture MCSs with high temporal and spatial resolution. One of the most important quantities observed by radars is the RW; as most MCSs are induced by the low-level convergence of water vapor, detecting low-level

convergence is a key to the successful prediction of MCSs. The assimilation of the RW at low elevation angles strongly contributes to the reproduction of low-level wind fields. Another important quantity observed by radars is reflectivity; in this study, the direct assimilation method of radar reflectivity was incorporated and applied to a heavy rainfall event that occurred in the Tokyo metropolitan area on 4-5 September 2005 (hereafter the Suginami heavy rainfall event; Kawabata et al. 2011b). In this case study, (i) improvement in the QPF after the inclusion of radar data assimilation will be shown, and (ii) a first attempt at capturing the nonlinearity of deep convection through data assimilation with cloud microphysics will be discussed.

Although GPS-PWV was used in both cases, this dataset only provides accumulated water vapor amount at each receiver site. As an alternative measure, GPS slant total delay (GPS-STD) provides the atmosphere-affected delay of radio waves traveling from GPS satellites to ground-based receivers, and GPS zenith total delay (GPS-ZTD) yields atmospheric delay above the receivers only. GPS-STD has an advantage in that it includes information about several atmospheric parameters (pressure, temperature, and humidity) in specific directions. Therefore, the assimilation of GPS-STD influences the water vapor field by informing the thermodynamic field in the model above and around observation points, especially at the storm scale. To apply this advantage to heavy rainfall forecasts, the assimilation of GPS-STD with NHM-4DVAR was employed in the third case study using a newly developed method. Prior to this study, Järvinen et al. (2007) and Bauer et al. (2011) developed an assimilation method of GPS-STD with regional 4D-Var systems, but the horizontal grid spacing of their systems was quite coarse. As such, the use of this data would have been no better than assimilation of GPS-ZTD data. A high-resolution assimilation system is necessary to realize the benefits of GPS-STD assimilation, and no studies adequately investigating the impact of GPS-STD assimilation have yet been conducted. In this work, GPS-STD assimilation was conducted on a heavy rainfall event that occurred at Okinawa Island on 19 August 2009 (hereafter the Naha heavy rainfall event; Kawabata et al. 2013b) as the first application of GPS-STD assimilation at the storm scale. In this case study, (i) the impact of the assimilation on the precipitation forecast will be discussed and (ii) factors for the initiation of line-shaped MCSs on Okinawa Island will be investigated.

These three studies provide discussion of both the predictability and initiation/sustainment mechanisms of localized MCSs with respect to the size of the environmental fields. The preferred observation and assimilation systems are identified in the general discussion section.

Variational assimilation theory, assimilation systems, and observation operators are described in Chapter 2. The relatively simple version NHM-4DVAR (v1) and the more complex version NHM-4DVAR (v2) are described in Sections 2.2 and 2.3, respectively. These were developed by Kawabata et al. (2007; 2011b). The observation operators (RW, surface observations, GPS observations, and radar reflectivity) are described in Section 2.4. These were developed by Kawabata et al.

(2007; 2011b; 2013b). The three case studies by Kawabata et al. (2007; 2011b; 2013b) are described in Chapters 3, 4, and 5, respectively. Because the motivation and development of the NHM-4DVAR systems and observation operators are deeply linked in each of the case studies, detailed information is given in introductory sections. A general discussion and general conclusions are given in Chapters 6 and 7, respectively. Relationships among case studies, associated developments, related papers, and the noted sections are listed in Table 1.1.

Contributions from the author to the development of the NHM-4DVAR were as follows. Initially, a development team was organized in 2002 as a collaboration between MRI and JMA to develop a non-hydrostatic 4D-Var based on JMA-NHM. The author contributed to the development of tangent linear and adjoint program codes at this stage. The collaboration resulted in the creation of a prototype non-hydrostatic 4D-Var with dry dynamics. A detailed description of this development is given in Section 2.2.2. Subsequently, the tangent linear and adjoint models of the prototype were advanced to that of the NHM-4DVAR (v1 and v2) by the author and Dr. T. Kuroda (MRI). Furthermore, the author designed control variables in the NHM-4DVAR (v1 and v2) and developed the observation operators, with the exception of the surface observation operators. The three case studies given in this thesis were also primarily conducted by the author.

Table 1.1. Relationships among case studies, corresponding developments on data assimilation systems and observation operators, and the structure of this thesis.

Case studies and papers	Developments (systems and observation operators)	Sections
Kawabata et al. (2007) Nerima heavy rainfall event on 21 July 1999		Chapter 3
	NHM-4DVAR with water vapor advection	Section 2.2
	Surface observation	Section 2.4.1
	Radar radial wind	Section 2.4.2
	GPS precipitable water vapor	Section 2.4.3
Kawabata et al. (2011b) Suginami heavy rainfall event on 4-5 September 2005		Chapter 4
	NHM-4DVAR with warm rain process	Section 2.3
	Radar reflectivity	Section 2.4.4
Kawabata et al. (2013b) Naha heavy rainfall event on 19 August 2009		Chapter 5
	GPS slant total delay	Section 2.4.5

Chapter 2

Nonhydrostatic Cloud-Resolving 4-dimensional Variational Data Assimilation System

In this chapter, detailed descriptions of the NHM-4DVAR system are given. A theoretical topic on the variational method is reviewed in Section 2.1. In Sections 2.2, formulations, control valuables of NHM-4DVAR v1 are described. NHM-4DVAR v1 considers perturbations to dynamical core and the advection of water vapor. Its horizontal resolution is 2 km, which is cloud resolving. Extension to cloud microphysics with warm rain is described in Section 2.3. Single-observation experiments described in Sections 2.3.4 and 2.4.5 are the first experiments which examined the efficiencies of rain water assimilation. Through these experiments, it is clarified that assimilating rainwater in a convection-free area is inefficient because the assimilation alone cannot maintain convection for long periods due to nonlinearity. In Section 2.4.5, the development of GPS slant total delays (STDs) at a cloud-resolving horizontal resolution is first described. Through single-observation experiments, it is clarified that the magnitude of the increment of GPS STD assimilation is large because all of the slant paths are within a narrow area of the lower troposphere above the observation site.

2.1 Theory

The four-dimensional variational method was adopted in this study because it can consider flow-dependency in the background error covariance under model integration within an assimilation window. In this section, the basic formulations of 4D-Var are reviewed.

First, the concept of data assimilation is introduced using minimum variance estimation. When x is the true value, unbiased observations y_1 and y_2 and their errors e_1 and e_2 are given as follows:

$$y_1 = x + e_1, \qquad\qquad (2.1)$$

$$y_2 = x + e_2, \tag{2.2}$$

$$E\langle e_1 \rangle = 0, E\langle e_2 \rangle = 0, E\langle e_1{}^2 \rangle = \sigma_1{}^2, E\langle e_2{}^2 \rangle = \sigma_2{}^2,$$

where σ_1 and σ_2 are standard deviations of e_1 and e_2, respectively, and $E\langle\ \rangle$ represents the expectation value of a quantity. For instance, y_1 and y_2 are temperature measured by different thermometers, and e_1 and e_2 are observational errors including measurement and representativeness errors. The measurement error is related to the instrument error while the representativeness error depends on the measuring location, measuring methods, averaging time, and other factors. The unbiased best estimation x^a is given as weighted average of observations using weights of a_1 and a_2:

$$x^a = a_1 y_1 + a_2 y_2, \tag{2.3}$$

$$\begin{aligned} E\langle x^a \rangle &= E\langle a_1(x + e_1) + a_2(x + e_2) \rangle \\ &= E\langle a_1 x + a_1 e_1 + a_2 x + a_2 e_2 \rangle \\ &= a_1 x + a_2 x \\ &= x, \end{aligned} \tag{2.4}$$

therefore,

$$a_1 + a_2 = 1. \tag{2.5}$$

The variance of the estimation is given as follows:

$$\sigma_a{}^2 = E\langle (x^a - x)^2 \rangle = a_1{}^2 \sigma_1{}^2 + a_2{}^2 \sigma_2{}^2, \tag{2.6}$$

where we further assume that e_1 and e_2 are uncorrelated. The best estimate occurs at the minimum of Eq. 2.6:

$$x^a = \frac{\sigma_2{}^2}{\sigma_1{}^2 + \sigma_2{}^2} y_1 + \frac{\sigma_1{}^2}{\sigma_1{}^2 + \sigma_2{}^2} y_2. \tag{2.7}$$

Thus we obtain the estimation as the average of both observations weighted with the rate of error variances of the observations. The variance of the estimate is given as follows:

$$\frac{1}{\sigma_a{}^2} = \frac{1}{\sigma_1{}^2} + \frac{1}{\sigma_2{}^2}, \tag{2.8}$$

This estimation is called the best linear unbiased estimator (BLUE).

As another approach, we introduce a cost function as a measure that represents the distance between the observations and the true value, with the error variances as follows:

$$J(x) = \frac{(x - y_1)^2}{\sigma_1{}^2} + \frac{(x - y_2)^2}{\sigma_2{}^2}. \tag{2.9}$$

The minimum value of J is given at the point at which the gradient of J is equal to zero:

$$\frac{dJ}{dx}(x^a) = 2\frac{(x^a - y_1)}{\sigma_1{}^2} + 2\frac{(x^a - y_2)}{\sigma_2{}^2}$$

$$= 0. \tag{2.10}$$

Therefore, this analysis gives a best estimate

$$x^a = \frac{\sigma_2{}^2}{\sigma_1{}^2 + \sigma_2{}^2}y_1 + \frac{\sigma_1{}^2}{\sigma_1{}^2 + \sigma_2{}^2}y_2, \tag{2.11}$$

that is equivalent to Eq. 2.7.

In this case, we consider both two pieces of information as observations, but one can be non-observational information, e.g., background or first guess. One general approach for optimal estimation is the maximum a posteriori (MAP) estimation. When a certain meteorological state $\mathbf{x}$, a first-guess field $\mathbf{x}^b$, and observations $\mathbf{y}^o$ are given, an optimal estimate $\mathbf{x}^a$ is determined at the maximum point of the conditional probability density function (PDF) $p(\mathbf{x}|\mathbf{x}^b, \mathbf{y}^o)$. Using Bayes' theorem, the PDF is represented as follows:

$$p(\mathbf{x}|\mathbf{x}^b, \mathbf{y}^o) = \frac{p(\mathbf{x}^b, \mathbf{y}^o|\mathbf{x})p(\mathbf{x})}{p(\mathbf{x}^b, \mathbf{y}^o)}$$

$$= \frac{p(\mathbf{x}^b|\mathbf{x})p(\mathbf{y}^o|\mathbf{x})p(\mathbf{x})}{p(\mathbf{x}^b, \mathbf{y}^o)}, \tag{2.12}$$

where $p(\mathbf{x})$ represents the climatological PDF. Because it is difficult to give a specific functional form to $p(\mathbf{x})$, we assume it as uniform. Therefore, it is enough to consider the maximum point of $p(\mathbf{x}^b|\mathbf{x})p(\mathbf{y}^o|\mathbf{x})$. Furthermore we assume that the PDF of $p(\mathbf{x}^b|\mathbf{x})$, and $p(\mathbf{y}^o|\mathbf{x})$ have Gaussian distributions,

$$p(\mathbf{x}^b|\mathbf{x}) = \frac{1}{\sqrt{2\pi}^n \mathbf{B}^{\frac{1}{2}}}\exp\left(-\frac{1}{2}(\mathbf{x}^b - \mathbf{x})^{\mathrm{T}}\mathbf{B}^{-1}(\mathbf{x}^b - \mathbf{x})\right), \tag{2.13}$$

$$p(\mathbf{y}^o|\mathbf{x}) = \frac{1}{\sqrt{2\pi}^m \mathbf{R}^{\frac{1}{2}}}\exp\left(-\frac{1}{2}(\mathbf{y}^o - H(\mathbf{x}))^{\mathrm{T}}\mathbf{R}^{-1}(\mathbf{y}^o - H(\mathbf{x}))\right), \tag{2.14}$$

where n denotes the degrees of freedom of the first guess field and m denotes the number of observations. H is the nonlinear observation operator, which is the interpolation operator from the first guess to the observational points; it may also be the nonlinear conversion operator from the first-guess values to observational values. When $\mathbf{x}^t$ denotes the true state, $\mathbf{B}$ represents the background error covariance matrix defined by $E\langle(\mathbf{x}^b - \mathbf{x}^t)(\mathbf{x}^b - \mathbf{x}^t)^T\rangle$, and $\mathbf{R}$ represents the observational error covariance matrix defined by $E\left((\mathbf{y}^o - H(\mathbf{x}^t))(\mathbf{y}^o - H(\mathbf{x}^t))^T\right)$.

When the terms in parentheses in Eqs. 2.13 and 2.14 are minimized, the PDF reaches at the maximum point. The point is given by minimizing the following equation:

$$J(\mathbf{x}) = \frac{1}{2}(\mathbf{x}^b - \mathbf{x})^{\mathrm{T}}\mathbf{B}^{-1}(\mathbf{x}^b - \mathbf{x}) + \frac{1}{2}(H(\mathbf{x}) - \mathbf{y}^o)^{\mathrm{T}}\mathbf{R}^{-1}(H(\mathbf{x}) - \mathbf{y}^o). \tag{2.15}$$

This optimal estimate of $\mathbf{x}$ occurs at

$$\nabla J(\mathbf{x}) = \mathbf{B}^{-1}(\mathbf{x}^b - \mathbf{x}) + \mathbf{H}^{\mathrm{T}}\mathbf{R}^{-1}(H(\mathbf{x}) - \mathbf{y}^o) = 0, \tag{2.16}$$

where $\mathbf{H}$ is the linearized observation operator. The first term of Eq. 2.15 is the difference between the first-guess field and the analysis field; it is called the 'background term'. The second term is the difference between observations and the analysis field; it is called the 'observation term'.

To expand Eq. 2.15 to time, the first-guess field is propagated into the future with a numerical model. This predicted field is compared to observations using the following cost function:

$$J(\mathbf{x}_0) = \frac{1}{2}(\mathbf{x}_0{}^b - \mathbf{x}_0)^{\mathrm{T}}\mathbf{B}^{-1}(\mathbf{x}_0{}^b - \mathbf{x}_0) + \frac{1}{2}(HM\mathbf{x}_0 - \mathbf{y}^o)^{\mathrm{T}}\mathbf{R}^{-1}(HM\mathbf{x}_0 - \mathbf{y}^o), \tag{2.17}$$

where M denotes a nonlinear numerical model and its subscript denotes the time level, with 0 indicating the initial time. The time period over which the comparison is conducted is called the 'assimilation window'. The distance between the first guess and analysis fields is evaluated only at the initial time, whereas the distances between the observations and the analysis fields are evaluated through the entire assimilation window. The gradient is given by

$$\nabla J(\mathbf{x}_0) = \mathbf{B}^{-1}(\mathbf{x}_0{}^b - \mathbf{x}_0) + \mathbf{M}^{\mathrm{T}}\mathbf{H}^{\mathrm{T}}\mathbf{R}^{-1}(HM\mathbf{x}_0 - \mathbf{y}^o), \tag{2.18}$$

where $\mathbf{M}^{\mathrm{T}}$ is the transpose of the tangent linear model and $\mathbf{M}$ is called the 'adjoint model'. The adjoint model carries information about the difference between the model-predicted field and the observations backward.

To obtain the solution of Eq. 2.17 and Eq. 2.18, we must calculate the inverse of matrices $\mathbf{B}$ and $\mathbf{R}$, whose dimensions exceed 10^{12} (number of horizontal grids × number of vertical layers × number of model prognostic variables) and 10^6 (number of observations), respectively. In general, because $\mathbf{R}$ is diagonal, solution of its inverse matrix is comparatively straightforward, but solution of the inverse matrix of $\mathbf{B}$ is impossible given present computing resources. Here, we introduce a control variable $\mathbf{v}$: $(\mathbf{x}_0{}^b - \mathbf{x}_0) = \mathbf{U}\mathbf{v}$. Here $\mathbf{U}$ is selected so that it satisfies $\mathbf{B} = \mathbf{U}^{\mathrm{T}}\mathbf{U}$. Thus, Eq. 2.17 can be rewritten as follows:

$$J(\mathbf{v}) = \frac{1}{2}\mathbf{v}^{\mathrm{T}}\mathbf{v} + \frac{1}{2}(HM\mathbf{x}_0 - \mathbf{y}^o)^{\mathrm{T}}\mathbf{R}^{-1}(HM\mathbf{x}_0 - \mathbf{y}^o). \tag{2.19}$$

Usually, the recursive filter (Purser et al. 2003), Choleskey decomposition, and Empirical Orthogonal Function (EOF) analysis are used to define the transformation $\mathbf{U}$. We can also amend the transformation procedure by considering relationships among the model prognostic variables (e.g., geostrophic balance). Here, the practical formulation of the variational method was shown.

2.2 NHM-4DVAR with water vapor advection (v2)

2.2.1 Basic formulation

The cost function of NHM-4DVAR is a function of the initial condition and the lateral boundary condition as follows:

$$J(\mathbf{x}_0, \mathbf{x}_{lbc}) = \frac{1}{2}(\mathbf{x}_0{}^b - \mathbf{x}_0)^\mathrm{T}\mathbf{B}^{-1}(\mathbf{x}_0{}^b - \mathbf{x}_0)$$

$$+ \frac{1}{2}(\mathbf{x}_{lbc}{}^b - \mathbf{x}_{lbc})^\mathrm{T}\mathbf{B}_{lbc}^{-1}(\mathbf{x}_{lbc}{}^b - \mathbf{x}_{lbc})$$

$$+ \frac{1}{2}(HM\mathbf{x}_0 - \mathbf{y}^o)^\mathrm{T}\mathbf{R}^{-1}(HM\mathbf{x}_0 - \mathbf{y}^o), \tag{2.20}$$

where $\mathbf{x}_0$ is the model prognostic variables and the lateral boundary condition at the beginning of the assimilation window, $\mathbf{x}_{lbc}$ the lateral boundary condition at the end of the assimilation window, $\mathbf{x}_0{}^b$ and $\mathbf{x}_{lbc}{}^b$ the first guess of $\mathbf{x}_0$ and $\mathbf{x}_{lbc}$ respectively, $\mathbf{B}$ and $\mathbf{B}_{lbc}$ the background error covariance matrices for $\mathbf{x}_0$ and $\mathbf{x}_{lbc}$ respectively, H the observation operators, $\mathbf{y}^o$ the observation, $\mathbf{R}$ the observation error covariance matrix, and M represents the nonlinear model. Details of the observation operators are explained in Section 2.3. It may be necessary to add a penalty term to the cost function to suppress unrealistic gravity waves, but it is not implemented in this study.

Some transformation methods for model variables are implemented to reduce the calculation of the inverse matrix of the background error covariance, because a dimension of this matrix is huge (~10^{12}). A set of variables presented in Section 2.2.3 is used as the control variables instead of the model prognostic variables themselves to ignore correlations between the control variables in the background error covariance. A transformation by using empirical orthogonal functions (EOFs) is used to remove vertical correlations of the control variables. A preconditioning method based on the Cholesky decomposition is implemented to accelerate the convergence rate of the minimization procedure. In addition, a limited memory quasi-Newton method (L-BFGS method; Zou et al. 1993) is used for a minimization algorithm.

2.2.2 Model specifications

JMA-NHM was developed by the Forecast Research Department of MRI and NPD/JMA (Saito et al. 2001). An operational version has been used as the mesoscale model of JMA since September 2004 (Saito et al. 2006; 2007; 2012). In JMA-NHM, fully compressible equations with map factors and the cloud microphysical processes with three ices (cloud ice, snow and graupel) are implemented. The parameterizations of sub-grid scale turbulence, air-surface interaction and radiative transfer processes are implemented. A terrain-following vertical coordinate (z* coordinate; Gal-Chen and

Somerville 1975) is adopted. The specifications of JMA-NHM are listed in Table 2.1.

In NHM-4DVAR, perturbations to momentums, potential temperature, pressure and the mixing ratio of water vapor were considered. The dry dynamics part of the tangent linear and adjoint models were taken from a prototype version of the JNoVA-4DVAR (Honda et al. 2003), and the advection of water vapor were added by Kawabata et al. (2004). These codes were based on the 2002 version of JMA-NHM. The specifications of the tangent linear and adjoint models are listed in Table 2.1. In this table, circles at the right column mean that the tangent linear and adjoint models follow JMA-NHM, while cross marks mean that the processes are omitted. Perturbations to the cloud microphysical processes, the parameterization of sub-grid scale turbulence, the parameterization of air-surface interaction and the radiative transfer processes are not considered.

Table 2.1. Specifications of JMA-NHM, the tangent linear and the adjoint models.

Category	JMA-NHM	The tangent linear model and the adjoint model
Basic equations	Fully compressible with a map factor	O
Prognostic variables	Momentums, potential temperature, pressure, kinetic turbulent energy, mixing ratio of water vapor, cloud water, cloud ice, rain, snow and graupel, and number density of cloud ice, snow and graupel.	Momentums, potential temperature, pressure, mixing ratio of water vapor
Vertical coordinate	Terrain-following	O
Horizontal coordinate	Lambert	O
Vertical grid structure	Lorenz type	O
Horizontal grid structure	Arakawa-C	O
Advection term	Flux form, second order	Flux form, Second order
Sound waves	Vertically implicit, horizontally split and explicit	O
Turbulent closure model	Deardorff (1980) level 2.5	X
Cloud microphysics	3 ice bulk microphysics (Ikawa and Saito 1991)	Advection of water vapor.
Radiation	Sugi et al. (1990)	X
Surface layer	Monin-Obukhov (Sommeria 1976)) Kondo (1975)	X

In addition, perturbations to the lateral boundary condition are considered. The lateral boundary conditions from an outer model are given at the beginning and end of an assimilation window and the lateral boundary conditions in the assimilation window are calculated with a time interpolation of them. A relaxation lateral boundary method is adopted in NHM-4DVAR.

In NHM-4DVAR, a full model of JMA-NHM is used as the forward nonlinear model, and an adjoint model is given by transposing a tangent linear model which linearized a simplified model of JMA-NHM.

2.2.3 Control variables and background errors

In the development of NHM-4DVAR, a horizontal resolution and the assimilation window in NHM-4DVAR are set to 2 km and 1 hour respectively, because our motivation is to investigate me-so-β scale MCSs with life time of a few hours. A suitable set of control variables is designed after examining the statistical characteristics of the forecast errors (background errors). Horizontal wind (u, v), vertical wind (w), nonhydrostatic pressure, potential temperature, surface pressure and pseudo relative humidity (Dee and Da Silva 2003) are chosen after examining several candidates (Table 2.2). It is assumed that forecast errors of the control variables are uncorrelated with each other.

Table 2.2. A set of control variables for NHM-4DVAR.

Variables	Formula
Wind	u, v, w
No-Hydrostatic pressure	$\pi = \pi_U - \pi_B$
Potential temperature	θ
Surface pressure	P_S
Pseudo relative humidity	$q_u = q/q_s^b$

After examination of several kinds of control variables for moisture, the pseudo relative humidity (q_u) was chosen, because its forecast error distribution is closer to the Gaussian distribution. The pseudo relative humidity is defined as follows:

$$q_u = \frac{q}{q_s^b} \ , \tag{2.21}$$

where q is the mixing ratio of water vapor and q_s^b is the saturation mixing ratio of water vapor given by the background. Relative humidity is usually defined as the ratio of the mixing ratio of water vapor to the saturated mixing ratio of water vapor. Since both of the mixing ratios vary during the iteration cycle of 4D-Var, the relative humidity is not easy to handle.

The nonhydrostatic pressure is chosen instead of the pressure itself except for surface pressure, because spatial auto-correlation of the hydrostatic pressure is very high in the whole region and the pressure itself has large spatial correlation with potential temperature. The pressure is expressed as the Exner function π in JMA-NHM. The nonhydrostatic pressure π_U is defined as follows:

$$\pi_U = \pi - \pi_B. \tag{2.22}$$

And π and π_B is defined as follows:

$$\pi = \left(\frac{p}{p_0}\right)^{R/C_P}, \tag{2.23}$$

$$\pi_B(z) = \pi_{surf} + \int_{surf}^{z} \frac{dz}{\vartheta}, \tag{2.24}$$

where p is the local pressure in the model, p_0 the reference pressure, R the gas constant for dry air and C_P the specific heat of dry air at constant pressure, θ the potential temperature.

The NMC method (Parrish and Derber 1992) is used to calculate the background error covariance. The 1-hour forecast errors of JMA-NHM with a horizontal resolution of 2 km and the vertical levels of 40 (2km-NHM) are calculated from the difference of two forecasts as follows. At first, a 9-hour forecast of JMA-NHM with a horizontal resolution of 5 km (5km-NHM) is performed to obtain the initial and boundary conditions of 2km-NHM. 5km-NHM is nested within the forecasts of the JMA regional spectral model (RSM; a horizontal resolution of 20 km). Then, two forecasts of 2km-NHM were performed; One is a 5-hour forecast with initial condition produced from the forecast of 5km-NHM at forecast time of 4 hours, and another 4-hour forecast with those at forecast time
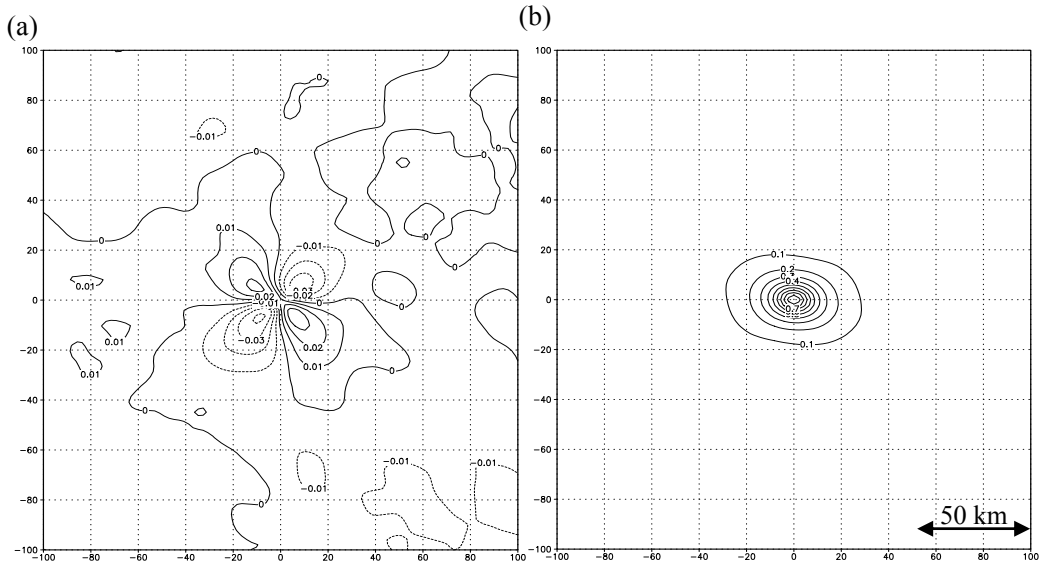
Fig. 2.1. Horizontal pattern of correlations of forecast errors at the 18-th vertical level of JMA-NHM. (a) Cross-correlation between x- and y-component of horizontal winds. (b) Auto-correlation of x-component of horizontal winds.

22

of 5 hours. This procedure is made four times a day for 12 days.

Statistical characteristics of the background error (forecast error) correlations of the control variables are examined. The horizontal pattern of cross-correlation of forecast errors between x- and y-components of horizontal winds is shown in Fig. 2.1a. The horizontal scale of cross-correlation is ~50 km, and the maximum value of the correlation is very small (about 0.03). This result partly supports the assumption that background errors of the control variables are uncorrelated with each other in the background error correlation matrix. Figure 2.1b shows the horizontal pattern of auto-correlation of x-component of horizontal winds. The pattern shows an oval stretched in the east-west direction, and the horizontal scale is ~50 km. Moreover, horizontal scale of cross-correlations between the variables and auto-correlations of each variable are also small and the maximum values are small, except for auto-correlation of pressure. These show the characteristics of the forecast errors of a high horizontal resolution and a short time range.

The one-hour forecast errors of 2km-NHM may be underestimated, because their initial conditions are not produced from an analysis but a forecast of 5km-NHM with the same initial condition. Therefore, the standard deviation of error statistics is inflated by a factor of 2.0, but that of q_u is inflated by a factor of 3.0. These factors were determined from the investigation of forecast errors (Kuroda et al. 2005).

2.3 NHM-4DVAR with warm rain process (v2)

2.3.1 New system

The adjoint model in Section 2.2 considers only dry dynamics and advection of water vapor, but this section implements a warm rain process (see Section 2.3.2).

Perturbations of water substances (the mixing ratios of rain water and cloud water) are considered, and new control variables associated with water substances are installed (see Section 2.3.3). The main prognostic variables and processes of JMA-NHM and perturbations of NHM-4DVAR are listed in Table 2.3. The cost function is formulated as:

$$J(\mathbf{x}_0, \mathbf{x}_{lbc}) = \frac{1}{2}\left(\mathbf{x}_0{}^{\mathrm{b}} - \mathbf{x}_0\right)^{\mathrm{T}} \mathbf{B}^{-1}\left(\mathbf{x}_0{}^{\mathrm{b}} - \mathbf{x}_0\right)$$

$$+ \frac{1}{2}\left(\mathbf{x}_{\mathrm{lbc}}{}^{\mathrm{b}} - \mathbf{x}_{lbc}\right)^{\mathrm{T}} \mathbf{B}_{lbc}{}^{-1}\left(\mathbf{x}_{\mathrm{lbc}}{}^{\mathrm{b}} - \mathbf{x}_{lbc}\right)$$

$$+ \frac{1}{2}(HM\mathbf{x}_0 - \mathbf{y}^{\mathrm{o}})^{\mathrm{T}} \mathbf{R}^{-1}(HM\mathbf{x}_0 - \mathbf{y}^{\mathrm{o}}). \tag{2.25}$$

In NHM-4DVAR, perturbations of water substances are considered in the initial field but not in the lateral boundary conditions. Therefore, $\mathbf{B}_{lbc}$ does not include the covariance associated with wa-

ter substances, but uses instead pseudo-relative humidity.

Because the forward model of NHM-4DVAR is a full-blown nonlinear model whereas the adjoint model is based on a "simplified" tangent linear model, there is an inconsistency between the forward and the adjoint models. Sometimes this inconsistency may cause solution divergence in the minimization procedures. In this study, we adopted short-term assimilation windows and a spin-up process to improve first-guess fields and prevent solution divergence (see Section 4.4). Since the full nonlinear model can represent a more realistic field than the simplified tangent linear model, especially in a highly nonlinear situation, the full nonlinear model can be used to evaluate a precise cost function J for assimilation of such a highly nonlinear situation. This point is important for convergence of minimization. In our discussion of this problem, we will describe an incremental 4D-Var system that adopts the tangent linear model as a forward model (Section 4.6.2).

Table 2.3 Specifications of NHM-4DVAR. [*] and [**] denote processes and variables which are considered in the adjoint model. [**] denotes perturbations and processes developed in this study.

Category	Specifications
Basic equation	fully compressible equation
Variables	Momentums*, potential temperature*, pressure*, mixing ratios of water vapor*, cloud water**, rain water**, cloud ice, snow, graupel and turbulent energy*.
Physics	Three-ice bulk cloud microphysics (warm rain process**), turbulent closure model, surface process, radiation, etc.

2.3.2 Warm rain process

We developed an adjoint model of the warm rain micro physical process that includes a Kessler-type parameterization scheme. A technique developed by T. Kuroda (2007, personal communication) was employed to detect nonlinear branches in this microphysical scheme. In this method, the results of all branches in particular subroutines are stored in memory and their influences are investigated. Using this method, an "IF" branch in FORTRAN program codes with strong nonlinearity was found in the warm rain process of the original JMA-NHM code. This branch was added to prohibit the evaporation of rainwater at a grid point where cloud water exists.

With careful treatment, a nonlinear IF branch can exist in a tangent linear model (Xu 1996), but such treatment has a high development cost. Tsuyuki (1996a; b) determined that removing the discontinuity from a nonlinear process can improve the linearity of a tangent linear model. This nonlinear IF was removed from the forward, tangent linear, and adjoint models of NHM-4DVAR after confirmation that its removal led to only very trivial differences in the simulation results.

2.3.3 Control variables

In an assimilation system in which water substances are not treated as control variables, cloud water and rainwater are absent at the initial time and are produced from water vapor during the model time integration. The time lag that is needed to create water substances is called the spin-up time. Assimilation of the radar reflectivity at the start time of an assimilation window thus allows the spin-up time to be minimized. For this reason, we added control variables associated with water substances to NHM-4DVAR.

One challenge in including water substances in the control variables is treatment of their background errors. We assumed that the background errors had a horizontally uniform distribution. However, water substances in the model often exist very locally, thus, the shapes of their background errors may not follow a Gaussian distribution.

In MM5-3DVAR and VDRAS, the control variable associated with water substances is total water, which is the sum of the mixing ratios of water vapor q_v, cloud water q_c, and rainwater q_r. Adopting total water requires separating it into q_v, q_c, and q_r. In VDRAS, total water is used as a prognostic variable in the forward nonhydrostatic model, so separation is handled during the model integration. The prognostic variables of water substances in MM5 are q_v, q_c, and q_r as in JMA-NHM. In MM5 and JMA-NHM, it is necessary to employ a separation process so that the control variables can be converted into the model prognostic variables. Separation of q_v and q_c is a linear process that uses a saturation adjustment. However, separation of q_r is a nonlinear process because of cloud microphyscs and it is inconvenient to perform the separation for the assimilation.

To implement microphysical processes in NHM- 4DVAR, we examined several candidate control variables considering the aspects of background errors and nonlinearity. Finally, we chose two variables: total water excluding q_r (i.e., $q_v + q_c$) and the relative mixing ratio of rainwater (q_r /q_{vs}^b), where q_{vs}^b is the saturation mixing ratio of water vapor given by the background). A probability density function (pdf) of the background error of total water ($q_v + q_c$) is presented in Fig. 2.2. The shape is not Gaussian but it is much closer to Gaussian than pdfs of the individual variables (q_v, q_c). The shape of the q_v error is similar to that of total water, but the q_c error is spiked shaped (not shown). The individual variable q_r is also spike shaped, whereas the relative mixing ratio of rainwater becomes Gaussian,
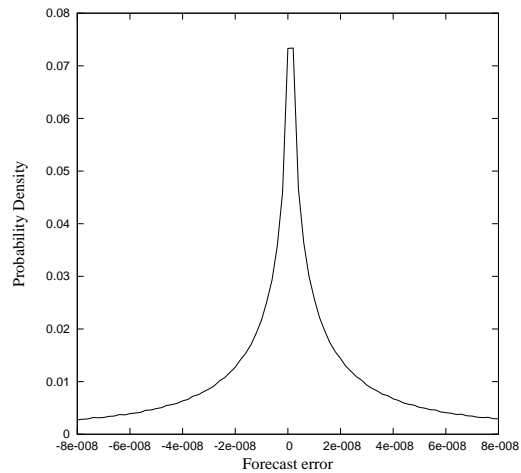
Fig. 2.2. Probability-density function of the background error of total water ($q_v + q_c$).

25

similar to relative humidity. We confirmed that the correlations between the two chosen variables and other variables were not large. Specifically, the correlation between potential temperature and total water is about 0.2, that between total water and the relative mixing ratio of rainwater is less than 0.1, and that between potential temperature and the relative mixing ratio of rainwater is 0.4.

Background errors were determined by the NMC method. One-hour forecast errors of JMA-NHM with 2-km grid spacing were calculated from the difference between two forecasts initiated at different times. These forecasts were initiated using the downscaled initial fields from the relatively coarse contemporary JMA operational regional model. As shown in Fig. 2.1, the horizontal scales of the errors were suitable for the cloud-resolving assimilation system, but their standard deviations were too small. Therefore, the standard deviations of the errors were inflated by a factor of 2.0 for dynamical variables and by a factor of 3.0 for variables related to water vapor and water substances. Section 2.2 presents detailed information and figures regarding this topic.

Table 2.4 lists the new control variables. Pseudo relative humidity (Dee and Da Silva 2003, q_v /q_{vs}^b), which was employed in the former version of NHM-4DVAR, is used as a control variable only for lateral boundary conditions, while total water is adopted as the control variable related to water vapor for the initial condition.

Table 2.4. Control variables of NHM-4DVAR. π is exner function defined as $\pi = \left(\frac{p}{p_0}\right)^{R/C_P}$. π_B is hydrostatic pressure defined as $\pi_B = \pi_{surf} - g \int_{surf}^{z} (\frac{dz}{\theta})$ q_v, q_c and q_r denote the mixing ratios of water vapor, cloud water and rain water, respectively. θ denotes virtual temperature. q_s^b denotes saturation mixing ratio of water vapor of the background field.

Variables	Formula
Wind	u, v, w
Potential temperature, surface pressure	θ, P_S
Nonhydrostatic pressure	$\pi - \pi_B$
Total water (for ICs)	$q_v + q_c$
Relative mixing ratio of rain water	q_r / q_{vs}^b
pseudo relative humidity (for LBCs)	q_v / q_s^b

2.3.4 Single-observation experiments

Before real observation assimilation experiments, we conducted single-observation data assimilation experiments without using the observation operator described in Section 2.4.4 to verify whether the responses of our assimilation system were reasonable. In these experiments, the result of the numerical simulation of an isolated deep convection described in Chapter 3 (the Nerima heavy rainfall)

was adopted as the first-guess field. The length of the assimilation window was set to 5 min, and we assumed that the mixing ratio of rainwater was observed at the start and end times of the assimilation window, separated by 5 min. We used two observations, the first at the start and the second at the end of the assimilation window, because this configuration was determined to incorporate the tendency of the observed convection into the analysis. The case of one observation carried out only at the start is equivalent to the 3DVAR case, a configuration not suitable for our study. Furthermore, if a single observation is carried out only at the end, then the data is not sufficient for determining whether the convection is in the development or decay stage. We examined three cases by changing the amount and location of the pseudo-observation data. The assimilation was carried out on a $24 \times 24 \times 40$ grid. The horizontal resolution was 2 km.

Fig. 2.3 illustrates the horizontal distribution of the mixing ratio of rainwater, divergence, and horizontal wind at the end time of the assimilation window. Here, Fig. 2.3a shows the first-guess field, and Figs. 2.3b–d present the results for cases 1, 2, and 3, respectively, as explained below. The pseudo-observation data are introduced at the crisscross mark ($\times$) in each figure, and the height z* of each figure (3.17 km in Fig. 2.3b, c; 1.7 km in Fig. 2.3d) corresponds to the height of the observation data.

Figs. 2.4 and 2.5 present vertical cross-sections of the mixing ratios of q_r and q_c and the wind along the line A–B in Fig. 2.3a at the start and end times, respectively, of the assimilation window. In the first-guess field (Fig. 2.4a and Fig. 2.5a), a convective updraft is seen at the center of the model domain, and cloud water is being generated by the updraft. The surrounding low-level water vapor is also being lifted up, producing more cloud water.

a. Case 1: Enhancement

In the enhancement case, 10 g kg^{-1} of rainwater was introduced at the center of the convection cell. This experiment was conducted to determine the response of the assimilation system when the observed rainwater exceeded the first guess. The result showed that the horizontal wind convergence is intensified and the convective cloud becomes bigger (Fig. 2.3b). The maximum value of the mixing ratio of cloud water at the start time is located around the assimilation point (Fig. 2.4b).

When a large amount of rainwater must exist in order to fit the observation, water vapor increases until saturation pressure causes excess water vapor to be converted to cloud water in the separation process. The large amount of cloud water seen in Fig. 2.4b is provided by this process. The cloud water is then converted to rainwater by a cloud microphysical process. At the end of the assimilation window (Fig. 2.5b), rainwater is descending and a downdraft is seen in the lower part of the convection cell.

From this result, we can expect that the underestimation of convection is adjustable by data assimilation if proper observations of rainwater are obtained near the convection.

b. Case 2: Decay

In the decay case, 0.01 g kg^{-1} of rainwater was introduced at the center of the convection. This experiment was conducted to see the response of the assimilation system when the observed rainwater was less than the first guess. In this case, the convection is weakened (Fig. 2.3c). Not only is the rainwater directly reduced, but also the updraft around the convection is weakened (Figs. 2.4c and 2.5c). The cloud water does not decrease as much as would be expected from the small amount of rainwater. This result shows that data assimilation of a small amount of rainwater weakens convection. We can expect that undesirable convection in a first guess can be weakened by assimilation of
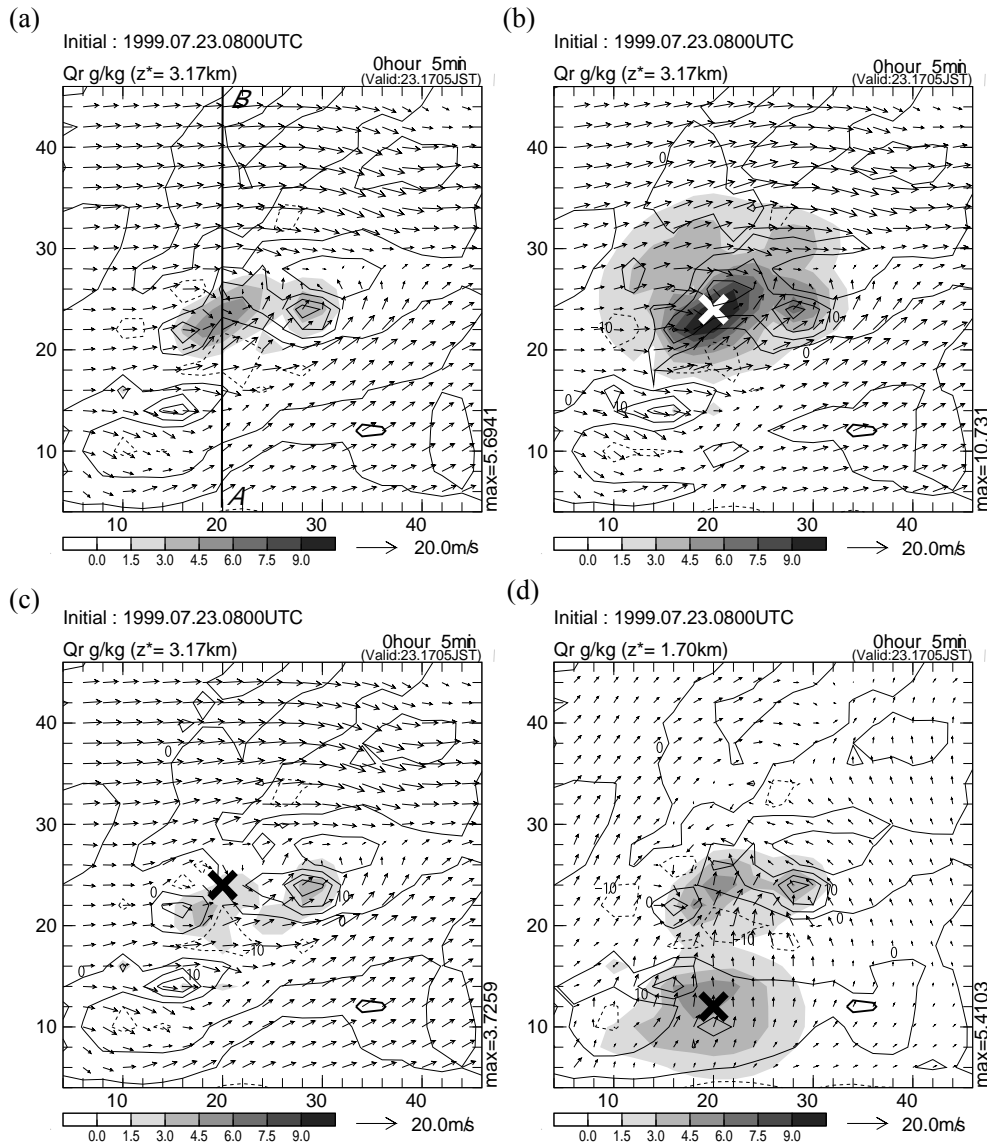
Fig. 2.3. Mixing ratio of rain water (shade), divergence (contours) and wind (vectors) at the end of the assimilation window. Cross marks (x) in (b)-(d) show the grid points where q_r observation data are put. Each figure's height corresponds to the level of observation data. (a) First guess field (z*=3.17km). (b) Enhancement case (z*=3.17km). (c) Decay case (z*=3.17km). (d) Generation case (z*=1.70km). Line A-B in (a) shows the line of the vertical cross section in Figs. 2.4, 2.5, and 2.6.

small or no reflectivity.

c. Case 3: Generation

In this case, 10 g kg^{-1} of rainwater was introduced at a point away from the convection. This experiment was conducted to see the response of the assimilation system when the observed rainwater is in a convection-free area or has a large positional error. Figure 2.3d depicts the generation of rainwater around the observation point. At the start time of the assimilation window, rainwater is produced above and below the observation point (Fig. 2.4d). A large amount of cloud water is seen above the observation point, but its height is lower than in the enhancement case and little updraft is observed. At the end of the assimilation window (Fig. 2.5d), rainwater is descending below the observation point. A downdraft has developed, and the cloud water has disappeared.
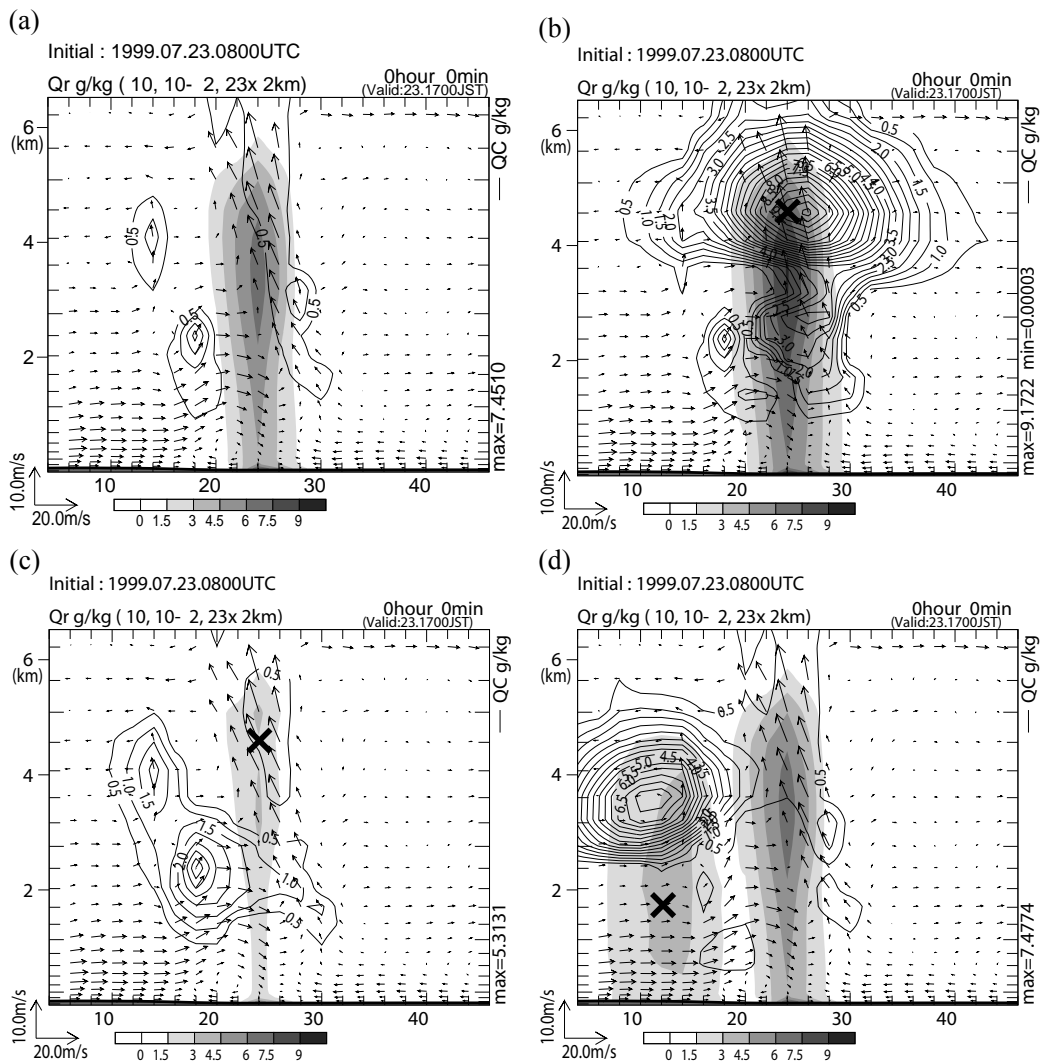
Fig. 2.4. Vertical cross sections of mixing ratios of q_r (shade), q_c (contours), and winds (vectors) along the line A-B in Fig. 2.3 at the start time of the assimilation window. Experiment cases (a)-(d) are the same as in Fig. 2.5.

29

The shading in Fig. 2.6 illustrates the differences of mixing ratio of water vapor, the vertical wind speed, and the potential temperature between case 3 and the first guess at the end of the assimilation window, except the vectors in Fig. 2.6 show the wind field of the generation case. Water vapor (Fig. 2.6a) increases in the upper levels above the observation point, and potential temperature (Fig. 2.6c) increases around the observation point. These features are consistent with typical environmental fields upon initiation of convection. However, a downdraft is generated at the end of the assimilation window. Since potential temperature around the observation point is increased compared with the first-guess field, it can be inferred that this downdraft is caused by the effect of rainwater drag. It is difficult to create and maintain new convection with just the assimilation of single observations of rainwater.

The case 1 and case 2 experiments clarified that the assimilation of rainwater has a positive impact in enhancing and decaying convection. However, case 3 is more difficult to interpret because
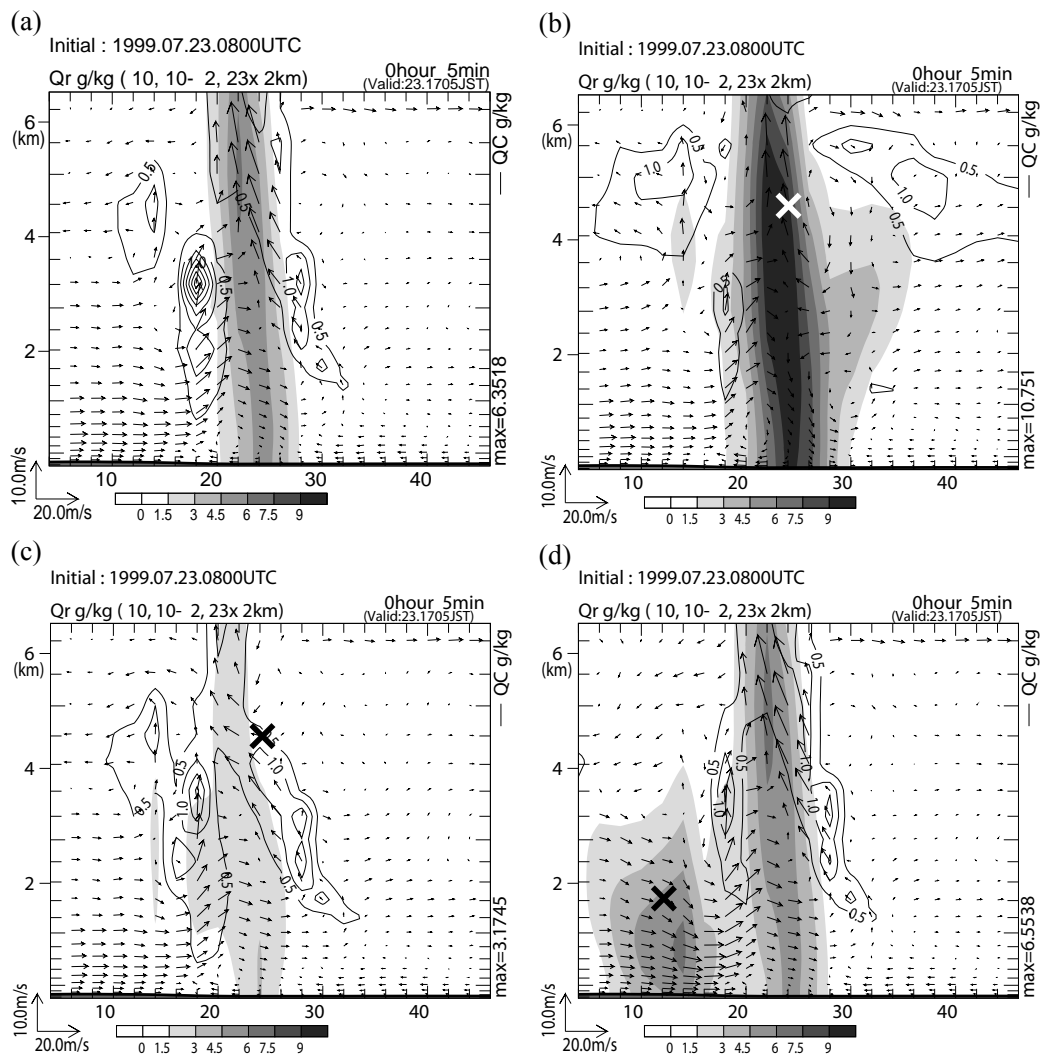
Fig. 2.5. Same as Fig. 2.4, but at the end time of the assimilation window.

30
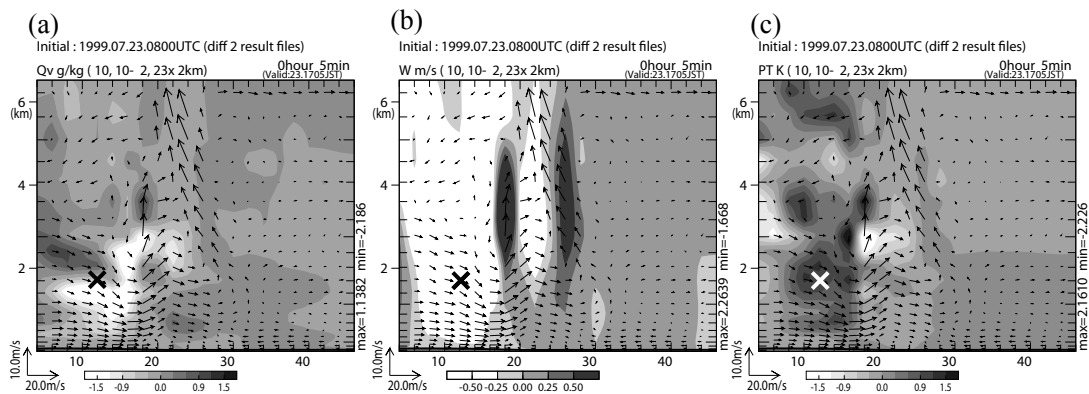
Fig. 2.6. Vertical cross sections of difference between the generation case and the first guess along the line A-B in Fig. 2.3a at the end of assimilation window. Shade indicates mixing ratio of water vapor in (a), vertical wind speed in (b), and potential temperature in (c). Vectors indicate the wind field of the generation case.

the assimilation of rainwater alone cannot maintain convection for a long time. However, the reproduced environmental field seems to be harmonious with natural convection. The assimilation of radar reflectivity would thus have a positive impact on modifying the first guess.

d. Summary

The cloud-resolving nonhydrostatic four-dimensional variational assimilation system (NHM-4DVAR) was evolved in order to directly assimilate radar reflectivity. Modifications included the development of an adjoint model of the warm rain process, the extension of control variables, and the development of an observation operator for radar reflectivity using the $Z-Q_r$ relationship.

Single-observation assimilation experiments were conducted to observe the responses of the modified NHM-4DVAR. A case of isolated deep convection was adopted as a first-guess field. Three experiments were performed using pseudo-observations of rain water at the start and end times of a 5-min assimilation window for specific enhancement, decay, and generation situations. When 10 g kg^{-1} of rain water was introduced at the center of the convection, the convergence of horizontal wind intensified and the convective cloud became larger. When 0.01 g kg^{-1} of rain water was introduced at the center of the convection, the convection was weakened. This result demonstrates that the underestimation of convection can be corrected by data assimilation if appropriate rain water observations are obtained near the convection, and that assimilating a small amount of reflectivity or none at all suppresses undesirable convection in the first guess. When 10 g kg^{-1} of rain water was introduced at a distance from the convection, rain water was produced above and below the observation point at the start time of the assimilation window, but by the end of the assimilation window, downdrafts had developed and the rain water descended below the observation point. It is likely to be difficult to create and maintain new convection by assimilation of only single observations of rain water.

2.4 Observation operators

2.4.1 Surface observations

For the surface temperature and winds observed by AMeDAS, the observation operators were developed by Nishijima (2005) for JNoVA-3DVAR. In these observation operators, parameterization scheme of surface-air interaction processes in JMA-NHM and their adjoint processes are considered. They were transplanted to NHM-4DVAR and modified the wind observation operator to treat observations as 10 minutes averaged data in the same manner as the observations. The observations are not assimilated in the case that the difference between the altitudes of an AMeDAS observation site and the model orography exceeds a threshold value (50 m for temperature, 20 m for winds), in consideration of the representativeness of the observational data. The observation errors of surface temperature and winds are set to 0.5°C and 1 m s^{-1}, respectively, as same as ones using in Meso 4D-Var. Surface temperature and winds are assimilated every 10 minutes.

2.4.2 Radial wind by Doppler radars

RW data are observed by the Doppler radars at the Haneda and Narita airports (for their locations, see Fig. 3.10c). The observation operator in NHM-4DVAR is same as that in the Meso 4D-Var developed by Seko et al. (2004a). Since the number of RW observation is much larger than that of the model grids, a super observation method is introduced. In this method, observed RW data are inserted to each horizontal grid point of the model as 'super observation'. Horizontal winds in the model are converted to radial winds and interpolated vertically under assumption that the spread of radar beam intensity from the center of beam has the Gauss distribution in vertical. Since it is difficult to separate the vertical velocity of air from the terminal velocity of raindrops, we neglect high elevation angle (over 5.4°) observations so that only horizontal motion of raindrops for RW is considered. The observation error of RW data is set to 1 m s^{-1} in consideration of one of the surface wind. RW data are assimilated every minute.

2.4.3 GPS precipitable water vapor data

GPS-PWV data used in this study were observed by GEONET of GSI, and reanalyzed by Shoji et al. (2004). Since they are the vertically integrated amount of water vapor from the altitude of a GPS receiver to the top of atmosphere, the observation operator of GPS-PWV is expressed as follows:

$$PWV\_\text{model} = \sum_{k=p}^{k=model\_top} q_k \rho_k \Delta Z_k + (correction term), \qquad (2.26)$$
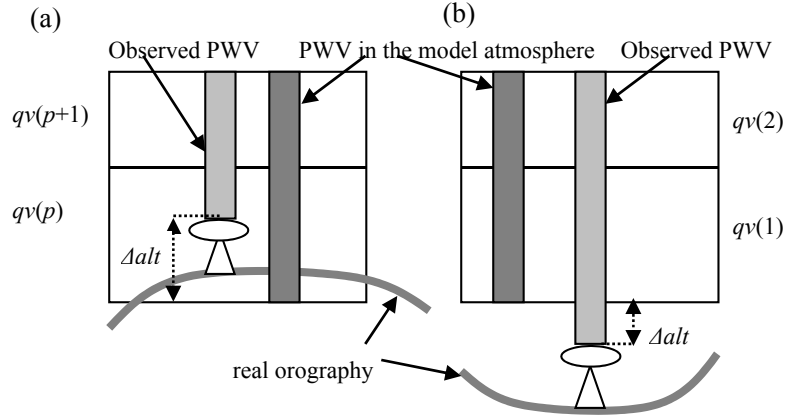
Fig. 2.7. Schematic diagram of the correction of model PWV. (a) In case that the GPS receiver altitude is larger than that of the model orography, model PWV is corrected by subtracting the extra water vapor, $q_v(p)\rho(p)\Delta alt$. (b) In case that the GPS receiver altitude is less than that of the model orography, model PWV is corrected by adding the deficient water vapor, $q_v(1)\rho(1)\Delta alt$.

where q is the mixing ratio of water vapor, ρ is the air density and Δz_k is the thickness of the k-th vertical layer. Since there is very small amount of water vapor in the atmosphere above the height of 'model_top' (about 22,000 m), water vapor above that height is ignored. A schematic diagram of this observation operator is shown in Fig. 2.7. Generally, the model orography is different from the altitude of a GPS receiver. When the altitude of the GPS receiver is higher than that of the model orography, the model PWV is corrected by subtracting the extra water vapor of the model PWV under the altitude of the GPS receiver. p is the number of the model layer at which a GPS receiver exists. When the GPS receiver altitude is lower than that of the model orography, the model PWV is corrected by adding the deficient water vapor by extrapolation of the model PWV to the altitude of the GPS receiver. In this case, p is the number of the lowest vertical layer. It is assumed that the mixing ratio of water vapor at the p-th layer is constant in both cases. If the difference between the altitudes of the model and actual orography exceeds a specified threshold value of 50 m, the GPS-PWV data is not used in the assimilation. The observation error of GPS-PWV is set to 1 mm. This value is smaller than Seko (2004a), because the horizontal grid spacing is smaller than the Meso 4D-Var. GPS-PWV data are assimilated every 5 minutes.

2.4.4 Radar reflectivity

We adopted the Z–Qr relationship from Sun and Crook (1997) as the observation operator for assimilating radar reflectivity:

$$10^{\left[\frac{Z-43.1}{17.5}\right]^{-3.0}} = \rho q_r, \tag{2.27}$$

where Z is the observed radar reflectivity (Z), ρ is the density of the model atmosphere (kg m^{-3}), and q_r is the mixing ratio of rainwater (kg kg^{-1}).

33

An alternative approach is to use a *Z–R* relation to relate the reflectivity to the precipitation accumulation *R*, but this involves weak nonlinearity. In contrast, Eq. 2.27 is perfectly linear because the lhs is a model variable and can be calculated prior to the assimilation process.

To avoid the uncertainty of weak reflectivity (i.e., the uncertainty in discriminating rainwater from other possible targets), observations below 10 dBZ were given special treatment, as described in Section 4.5.4. The observational error includes a measurement error and a representativeness error. The instrument error, which is provided by the manufacturer, is about 1 dBZ, but the error in actual observations will be larger than the instrument error. Moreover, the observational error will be larger than the measurement error alone because of the representativeness error and the use of a simplified observation operator (Eq. 2.27) and an adjoint model in the data assimilation system. To confirm the typical magnitude of the observational error of our system, the departure (observation vs first guess) was determined, and the standard deviation was found to be about 15 dBZ. The specific value of 15 dBZ is used in NHM- 4DVAR via Eq. 2.27.

In addition, in a preliminary study, we performed impact tests (results not shown) in order to determine the specific value of the observational error, testing values from 5 to 20 dBZ. In the impact test using the value of 5 dBZ, the rainband did not last as long as predicted by the result of this paper, whereas in the impact test using the value of 20 dBZ, the reproduced rainband was very weak. In light of these results, we set the observational error to 10 dBZ. Observational data are transformed into "super observations" by interpolating the data to model grids for each elevation angle. A similar treatment was used in the assimilation of Doppler velocity observations.

2.4.5 GPS slant total delay data

a. Observational operator

GPS-STD is affected by the atmosphere along the ray path. Shoji et al. (2004) decomposed GPS-STD data into three components, isotropy, first-order horizontal gradient, and higher order inhomogeneity, and showed that the horizontal scale of each component was different, about 600, 60, and 2–3 km, respectively. GPS-ZTD data represent only the isotropic component of GPS-STD data observed at the same time at the same site, and GPS-PWV data consist of only the isotropic water vapor information contained within the GPS-ZTD data. This study represents an attempt to fully utilize the GPS-STD data. In this section, we describe an observation operator for GPS-STD data.

Radio waves from GPS satellites in orbits higher than 20,000 km are delayed by various factors, and GPS meteorology applications that take advantage of this atmospheric delay have been developed (e.g., Shoji 2009). The speed of radio waves is smaller in the atmosphere than in a vacuum. This atmospheric delay effect can be described in terms of the refractive index *n*, as follows:

$$n = \frac{c_0}{c} > 1, \qquad (2.28)$$

where c_0 and c represent the speed of light in a vacuum and the atmosphere, respectively. The general equation for the radio refractive index is

$$n = 1 + \left(K_1 \left(\frac{P_d}{T} \right) + K_2 \left(\frac{P_v}{T} \right) + K_3 \left(\frac{P_v}{T^2} \right) \right) \times 10^{-6}, \qquad (2.29)$$

where P_d (hPa) and P_v (hPa) denote the partial dry atmospheric pressure and the partial water vapor pressure, and T (K) denotes the temperature. K_1 is 77.60 K hPa^{-1}, K_2 is 71.98 K hPa^{-1}, and K_3 is 3.754×10^5 K^2 hPa^{-1} (Boudouris 1963). Equations 2.28 and 2.29 both show that a radio wave traveling in the atmosphere takes a longer time to go a given distance than one traveling in a vacuum. The delay can be measured in terms of distance (L) as follows:

$$\Delta L = \int_{Model\_surface}^{Model\_top} (n-1)ds. \qquad (2.30)$$

Here, ΔL denotes the atmospheric delay (m), ds is the path length (m) in each model grid cell, and n denotes the averaged refractive index along the path in a grid cell.

In this study, the effect of the earth's curvature was considered but the radio waves were assumed to be propagated along straight pathways; thus, the bending effect is ignored. This assumption may lead to errors at low GPS satellite elevation angles. As described in Section 2.4.5b, we applied large observational errors to low elevation angles so that the linear assumption would not lead to serious problems. First, the linear path from the receiver to the GPS satellite is determined. Then the coordinates of the middle point of the path within the model grid cells are calculated. Delays at eight points surrounding the middle point are interpolated to the point and averaged with each distance. The delay at the point is multiplied by the length of the path within the model cell, and then the delays in cells along the path are integrated from the surface to the top of the model. We used GPS-STD observations with path elevation angles of 5° or more in this study. The World Geodetic System 1984 (WGS84; National Imagery and Mapping Agency 1997) is adopted as the reference GPS coordinate system. Therefore, WGS84 is used in the observation operator.

It is necessary to add the atmospheric delay above the model top (22 km in this study) to the left side of Eq. 2.30. We assumed that the delay decreased to $1/e$ every 10 km height from the model top to 200 km height (Bean and Thayer 1959) and that above 200 km the amount of delay was zero.

We also ignored perturbations in the dry atmospheric pressure (P_d) in the adjoint code of the observation operator (Eq. 2.29) because such perturbations sometimes produce noise in pressure in NHM-4DVAR, which contains no penalty term to alleviate such noise. We also ignored perturbations in the air density in the GPS-PWV assimilation for the same reason (Section 2.4.3). In prelimi-

nary sensitivity experiments, we confirmed that inclusion of pressure perturbations had a negligible impact on the rainfall forecast (not shown).

b. Observational error

Because the average distance between GPS receivers in Japan is about 20 km, high cross-correlations may exist in observational errors between receivers if the slant paths are close together. We examined correlations among GPS-STD values as follows. First, we constructed data sets of GPS-STD values derived from two GPS satellites observed by a single GPS receiver and calculated the correlation between the two sets of observations. Observations were made every 5 min from 0900 to 1500 JST on 19 August 2009 by the method of Shoji (2013). The resulting correlation coefficient averaged over all observations was –0.02. Even when the angle between the paths from the receiver to each of the two satellites was less than 30°, a situation that accounted for only 6% of all the data, the correlation coefficient was just 0.4. Therefore, correlations between individual GPS-STD observational errors are generally small. Thus, for simplicity, we assumed that the GPS-STD observational error covariance matrix was a diagonal matrix.

"Observational errors" in data assimilation are composed of measurement error and observation operator error. To evaluate the latter error, we constructed another data set of model-predicted STDs. A JMA-NHM simulation was carried out using a 2-km horizontal grid spacing and the JMA operational mesoscale analysis was used for the initial and boundary conditions. The examination domain was almost the entire area of the Japanese islands (not shown). We then plotted the predicted GPS-STDs against the observed slant delay values (Fig. 2.8) without applying any quality controls to the data. Although the data do not exhibit any apparent bias, the difference between the predicted and observed delay values is large for values larger than 12 m, and the difference distribution is bimodal at delay values from 5 to 10 m (Fig. 2.8). This bimodal distribution may be a problem for rigorous assimilation, but we are still investigating its cause, which may be, for example, an insufficient sample size or an inappropriate observation operator.

It is difficult to determine the GPS-STD measurement error because no comparable reliable observations exist. Upper soundings are comparable only in the zenith direction, and because few are available, they cannot be examined statistically. Consequently, we based the value of the observational error mainly on values used by previous studies and on comparisons with GPS-PWV assimilation results.

Bauer et al. (2011) used 1 mm of precipitable water vapor, which is equivalent to 6 mm of GPS-ZTD, as the observational error in the zenith direction. They calculated this error using data from a German observation network and European mesoscale model predictions. Järvinen et al. (2007) inferred a ZTD error of 11 mm from a comparison of modeled and observed STDs.

36

In this study, we first set the GPS-ZTD observational error to 11 mm, under the assumption that the cost function value of GPS-ZTD should be a few times larger than the GPS-PWV cost function value, because GPS-ZTD data contain more meteorological information than GPS-PWV data.

Because GPS-ZTD uses mapping functions to average several GPS-STDs, GPS-ZTD observations are considered to be more reliable than individual GPS-STDs, even if the elevation angle is high. Furthermore, the observational error depends on the elevation angle. Järvinen et al. (2007) and Bauer et al. (2011) used the same type of error model. By comparing GPS-STD assimilation with GPS-PWV assimilation and considering the GPS-ZTD error, we estimated that the GPS-STD error in the zenith direction was 50 mm and adopted the error model below;

$$\text{ObsError} = \frac{50 \, mm}{\sin^4 \theta}, \tag{2.31}$$

where θ denotes the elevation angle. When we used Eq. 2.31 to compute the observational error, GPS-STD observations at low elevation angles had only a small impact on the assimilation result. Both the 50 mm value and the error calculated with Eq. 2.31 are large compared with the values suggested by Järvinen et al. (2007) and Bauer et al. (2011), but we chose to use a conservative value and function for this first GPS-STD assimilation trial, because our assumption of linear propagation (see Section 2.4.5a) might result in large observational errors at low elevation angles. In addition, when the elevation angle exceeds 85°, the standard deviation of the departure value (observation minus model; Fig. 2.8) is 35 mm, which is comparable to the 50 mm used in Eq. 2.31.
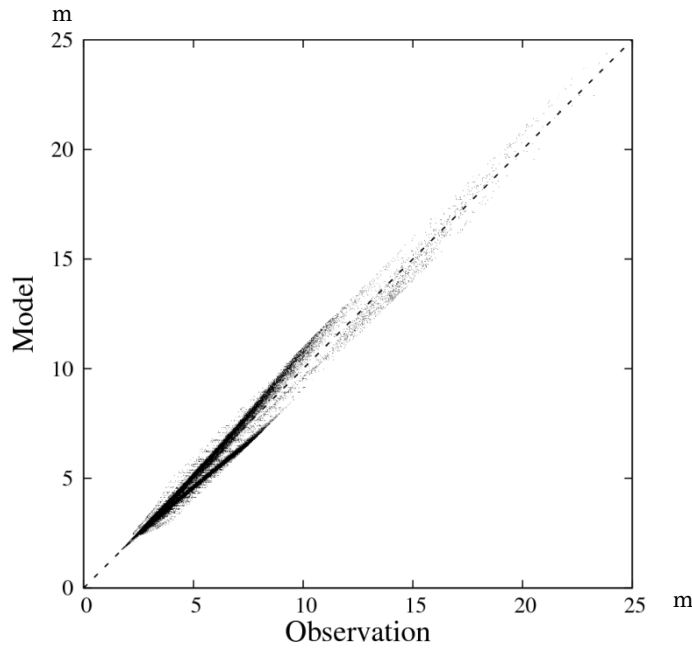
Fig. 2.8. GPS slant total delay values (m) in simulations (vertical axis) and observations (horizontal axis).

37

On the basis of these considerations and the results of our investigations, we adopted the following quality controls. When the elevation difference between an observation site and the modeled topography exceeded 50 m, the observations were not used as the same criterion in Kawabata et al. (2007; 2011b). We also discarded data when the observed delay exceeded 10 m and the absolute value of the departure value exceeded 1 m.

c. Data thinning

The cost function value of GPS-STD is still large, despite the use of a large observational error model, because the number of GPS-STD data is very large; therefore, we thinned the GPS-STD data. When two slant total delays from a GPS satellite were observed by two adjacent receivers, one STD value was eliminated, and the remaining one was selected. Similarly, if two or more slant delays were observed at the same time, STD values were thinned approximately in half. The thinning procedure halved the value of the cost function.

d. Impact on single analyses at a single site

First, we performed three experiments using NHM-4D-VAR with a 2-km horizontal grid spacing in which three GPS-STD observations (SO_STD), one GPS-ZTD observation (SO_ZTD), or one GPS-PWV observation (SO_PWV) from a single observation site were assimilated. As mentioned in Section 2.4.5a, the GPS-ZTD and GPS-PWV observations were derived from the GPS-STD observations. The purpose of these experiments was to verify the effects of GPS-STD assimilation on a single analysis result and to examine the differences among GPS-STD, GPS-ZTD, and GPS-PWV assimilations. The length of the assimilation window was 10 min, and the observations were assimilated at 5-min intervals (at 0, 5, and 10 min in the assimilation window). The observation data were selected by considering their horizontal distributions, elevation angles, and the first-guess field from an experimental data set.

Figure 2.9 illustrates the propagation paths of radio waves from three GPS satellites to a receiver in the model atmosphere in both the horizontal (Fig. 2.9a) and the vertical plane (projected from the south; Fig. 2.9b). Path I has the smallest angle of elevation among the three paths and is also the longest path, whereas path II, which has an angle of elevation near 90°, is very short. Large delays occur mostly at low altitudes.

The distributions of the analysis increments (analysis minus first guess) of precipitable water vapor in SO_STD (Fig. 2.10a) and SO_ZTD (Fig. 2.10b) at the end of the assimilation window differ. In SO_ZTD, the increment distribution (Fig. 2.10b) is elliptical and almost axisymmetric (i.e., isotropic). Although 4D-Var is capable of producing flow-dependent (anisotropic) analysis increments, the 10-min assimilation window is too short to capture the model dynamics. As a result, the analysis increment distribution in SO_ZTD is almost isotropic. In contrast, the inhomogeneous shape of the analysis increment distribution in SO_STD (Fig. 2.10a) reflects the distribution of the slant paths. In

addition, the maximum analysis increment value is much larger in SO_STD (10 mm; Fig. 2.10a) than in SO_ZTD (6 mm; Fig. 2.10b). The increment distribution in SO_PWV was similar to that in SO_ZTD (not shown).

In vertical cross sections of the analysis increments of the mixing ratio of water vapor (Qv) and potential temperature (θ) along path III (Fig. 2.11), the increment distributions of SO_ZTD and SO_PWV are similar, and the increment magnitudes are nearly the same: the distributions of both Qv and θ increments extend vertically from 1 to 5 km height and horizontally a distance of 5 to 8 km. In contrast, in SO_STD the increment distribution along path III extends horizontally a distance of 15 km and vertically to a height exceeding 8 km; moreover, the increment magnitudes are much greater, especially at low altitude (around 3 km). The magnitude of the assimilation increments is large because all of the slant paths are within a narrow area of the lower troposphere above the ob-
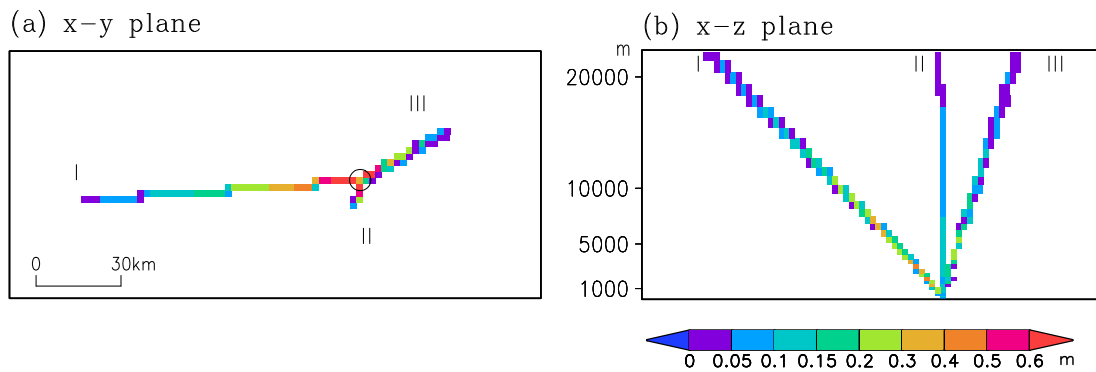
Fig. 2.9. Propagation paths of radio waves from GPS satellites (I, II, and III) to a receiver in the model atmosphere, viewed in the horizontal plane (a) and the vertical plane (b). Colors indicate the delay value in each grid cell (each model grid cell is represented by one pixel). The open circle in (a) shows the position of the GPS receiver (the observation site).
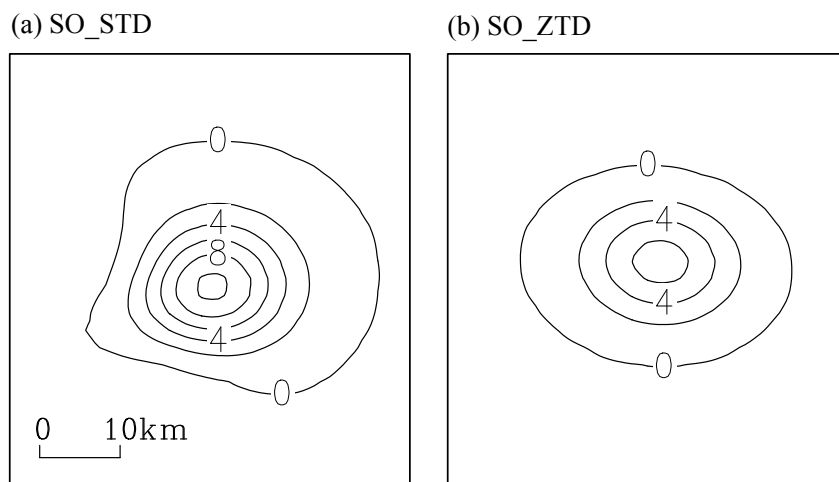
Fig. 2.10. Analysis increments of precipitable water vapor (mm) at the end of the assimilation window for SO_STD (a) and SO_ZTD (b).

servation site. Total weights in the cost function were similar among the SO_STD, SO_ZTD, and SO_PWV assimilations, but their effects are seen at different places.

e. Summary

The observation operator for GPS-STD assimilation was developed. In this method, the linear propagation of the radio waves was assumed. And we also adopted an elevation-dependent observation error model and data thinning to keep the magnitude of the GPS-STD cost function reasonable compared with that of the GPS-PWV cost function.

Differences in the impact of assimilations of GPS-STD, GPS-ZTD, and GPS-PWV observations were examined through single observation site on a single analysis result. The GPS-ZTD and GPS-PWV assimilation results were similar in their basic features. The distributions of the analysis
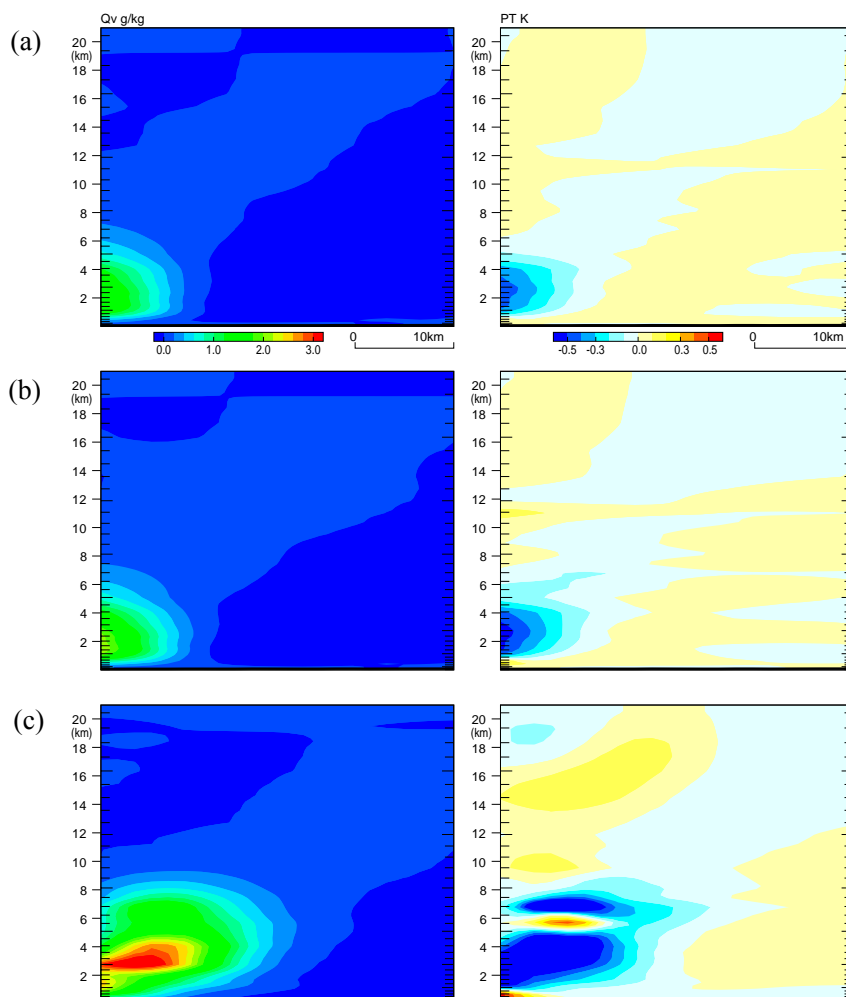
Fig. 2.11. Vertical cross sections along path III. Analysis increments of the mixing ratio of water vapor are shown in the left column and potential temperature in the right column. SO_PWV (a), SO_ZTD (b), and ST_STD (c). The observation site is at the lower left corner of each panel, and path III leaves the model top at the upper right corner.

40

increments obtained by the GPS-PWV and GPS-ZTD assimilations were approximately circular, whereas the increment distribution obtained by GPS-STD reflected the inhomogeneous data distribution. Moreover, analysis increments at low altitudes were larger in the GPS-STD assimilation than in the GPS-ZTD or GPS-PWV assimilations. These results demonstrate that more horizontal atmospheric information is included in GPS-STD assimilation, and that the effects of GPS-STD assimilation are large at low atmospheric levels above the observation site.

Chapter 3

Assimilation Experiment using NHM-4DVAR v1 with Radial Wind and GPS Precipitable Water Vapor Data

- Nerima Heavy Rainfall Event on 21 July 1999 -

A case study on the Nerima heavy rain fall event occurred in the north of Tokyo on 21 July 1999 using the cloud-resolving 4D-Var system (NHM-4DVAR v1; see Section 2.2) is shown. This study is the world-first experiment assimilating multiple observations of surface, Doppler radial wind, GPS precipitable water vapor data (see Section 2.4.1-2.4.3) at a cloud-resolving horizontal resolution. Initiation and development mechanisms of an isolated thunderstorm are discussed. Analysis of observational data and forecasting results clarified that a surface convergence line of horizontal winds was caused by sea breeze and north-easterly winds. Consequently, the wind convergence was enhanced around Nerima. An air mass of high equivalent potential temperature was lifted over this enhanced convergence line to generate cumulonimbi that caused the Nerima heavy rainfall. The result first shows that it is possible for MCSs even in a meso β-γ scale to be predicted with accurate intensity, occurrence time and location, when preferable conditions are assimilated before convection initiation.

3.1 Introduction

In the Nerima heavy rainfall event, which occurred on 21 July 1999, the maximum one-hour rainfall amount of 111 mm was recorded at Nerima, near the central part of Tokyo metropolitan area over the Kanto plain. The flood caused by this rainfall claimed one person and damaged about 800 houses. This heavy rainfall was caused by developed cumulonimbi (hereafter, 'Nerima cells') that organized into an MCS. JMA-NHM with the initial condition produced from the forecast of the JMA hydro-

static mesoscale spectral model (MSM) could not reproduce this event.

The MSM with a horizontal resolution of 10 km and a 4-dimensional variational assimilation (4DVAR) system for the MSM (Meso 4D-Var, Koizumi at al. 2005) have been operated at JMA since 2001 and 2002 respectively. This system is the first operational 4DVAR system aimed at mesoscale analysis, and considerably improved the forecast skill of the MSM, because the 4DVAR technique can assimilate continuous observations and can estimate optimal initial conditions for the MSM more sophisticatedly than conventional assimilation systems such as the optimal interpolation technique. However, horizontal resolution of the MSM (10 km) and the forward and adjoint models in the Meso-4D-Var (20 km) are insufficient to resolve deep convection in MCSs.

Seko et al. (2004a) investigated the Nerima heavy rainfall event by using the Meso 4D-Var. In their study, the precipitable water vapor derived from Global Positioning System (GPS-PWV) data and the Radial Wind (RW) data observed by Doppler radars were assimilated by using the Meso 4D-Var. The shape and location of precipitation areas were well reproduced by the MSM in their assimilation experiment. However, the precipitation intensity was underestimated in comparison with observations. Seko et al. (2004b) also applied a nonhydrostatic 3-dimensional variational assimilation system (Miyoshi 2003) to this event. In this experiment, however, no heavy rainfall area was simulated over the Kanto plain. In a sensitivity experiment in which updrafts in their humid regions are enhanced using a statistical relation between vertical velocity and humidity, heavy rainfall was successfully reproduced. In 4DVAR systems that can resolve MCSs, such a relation can be expressed through the equations of momentum and water vapor.

Some 4DVAR systems based on NHMs have been developed. The MM5-4DVAR (Zou et al. 1996), based on the Pen state/NCAR mesoscale model version 5 (MM5: Dudhia 1993), has been applied to several heavy rainfall events and typhoon cases (e.g., Guo et at. 2000), but its horizontal resolution was about 20 km. The VDRAS (Sun and Crook 1997) was developed to retrieve the 3-dimensional dynamic field and cloud microphysics field from Doppler radar data. The VDRAS with a resolution of about 2 km was applied to a supercell storm case (Sun 2005), but the nonlinear model in the VDRAS adopted an anelastic dynamical framework and simplified cloud microphysical processes.

For successful reproduction for MCSs, the information of horizontal winds and water vapor observed with a high temporal and horizontal resolution is necessary to be assimilated. Over the southern part of the Kanto plain, two Doppler radars are operated at the Haneda and Narita airports. The surface observation network called the Automated Meteorological Data Acquisition System (AMeDAS) is available with a mean horizontal resolution of about 20 km over Japan. Furthermore, the Geospatial Information Authority of Japan (GSI) operates the GPS Earth Observation NETwork (GEONET) which covers all of the Japan Islands with a mean horizontal resolution of about 20 km.

Therefore, RW data, GPS-PWV data and surface observational data can be assimilated by 4DVAR as high temporal and spatial resolution data.

The Numerical Prediction Division (NPD) of JMA and the Meteorological Research Institute (MRI) have been developing 4DVAR systems based on JMA-NHM. Since JMA-NHM is a fully compressible model with cloud microphysical processes, the 4DVAR systems are more suitable to reproduce the structure of convective cells in rainfall systems than the Meso 4D-Var. The collaborating development between NPD and MRI started in 2002, and a proto-type version of the nonhydrostatic 4D-VAR (JNoVA-4DVAR) was presented (Honda et at. 2003; Kawabata et at. 2003). A pre-operational version of the JNoVA-4DVAR with a horizontal resolution of 5-10 km has been under development at NPD. Honda et al. (2005) applied this system to a heavy rainfall event at Fukui in the central part of Japan and showed a successful improvement of the rainfall prediction. In some cases, a higher horizontal resolution is necessary to reproduce heavy rainfall events as shown by Kato and Aranami (2005). The clouds must be represented by the microphysics and the nonhydrostatic effect is essential for the heavy rainfall phenomena caused by deep convection. Based on the proto-type version of the JNoVA-4DVAR, MRI has been developing a cloud-resolving data assimilation system with a horizontal resolution of less than 2 km. Here, we call this system as the 'NHM-4DVAR'. NHM-4DVAR is designed to provide the initial conditions to the cloud-resolving model, where the initial conditions are optimized with the temporally and spatially high resolution observation data and the model time integration.

In this case study, the first motivation is to present NHM-4DVAR based on JMA-NHM to resolve MCSs. The second motivation is to clarify the formation mechanism of the Nerima heavy rainfall by using NHM-4DVAR. The formation mechanism of heavy rainfall can contribute to the prevention of disasters and the safe air transportation. NHM-4DVAR is already described in Section 2.2. In Section 3.2, the overview of the Nerima heavy rainfall event is presented, and the environ-
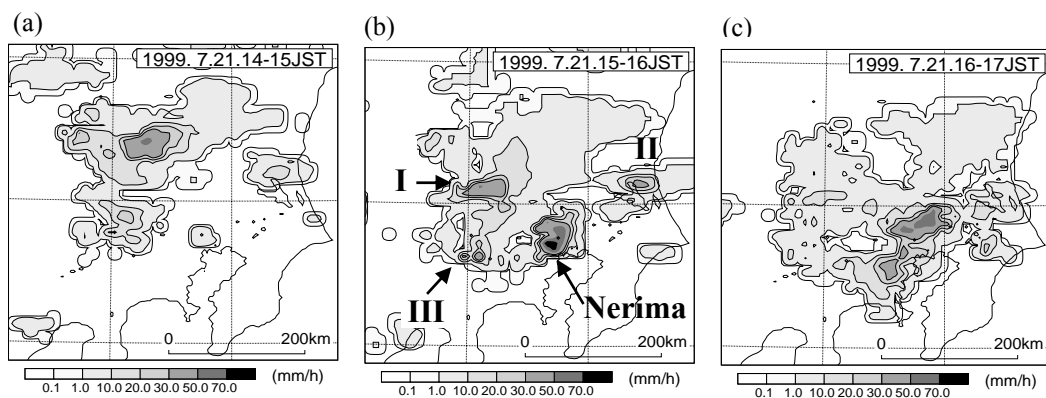
Fig. 3.1. Distributions of hourly accumulated rainfall amount, from Radar-AMeDAS. (a)14-15 JST, (b)15-16 JST and (c)16-17 JST at 21 July 1999. Symbols of **I**, **II** and **III** denote other rainfall areas with intense precipitation, except for the Nerima heavy rainfall.

45

mental field is examined using observational data. In Section 3.3, the structure of the Nerima cells is discussed through assimilation and forecast results by NHM-4DVAR. Conclusion in this study is given in Section 3.4.

3.2 Overview of the Nerima heavy rainfall event

The Nerima heavy rainfall was observed on 21 July 1999 at Nerima, north part of Tokyo, and the maximum rainfall amount of 111 mm was recorded at the Nerima AMeDAS observation station. Figure 3.1 shows the horizontal distribution of hourly rainfall amount of the Radar-AMeDAS analyzed rainfall between 15 JST and 17 JST, which is the radar-estimated rainfall amount calibrated by AMeDAS rain gage data. An area with precipitation intensity larger than 70 mm h^{-1} is found around Nerima at 16 JST. This heavy rainfall was only observed between 15 and 16 JST, and the horizontal scale of its area was about 30 km. Therefore, heavy rainfall is a phenomenon with the short life time and the small horizontal scale. Furthermore, other rainfall areas with intense precipitation (>50 mm h^{-1}) are found (denoted by symbols of 'Ⅰ', 'Ⅱ' and 'Ⅲ'). The time sequence of 10-minute rainfall amount observed at Nerima between 1510 JST and 1650 JST is shown by gray bars in Fig. 3.2. Very intense rainfall (about 20 mm 10 min^{-1}) was observed between 1530 JST and 1610 JST.
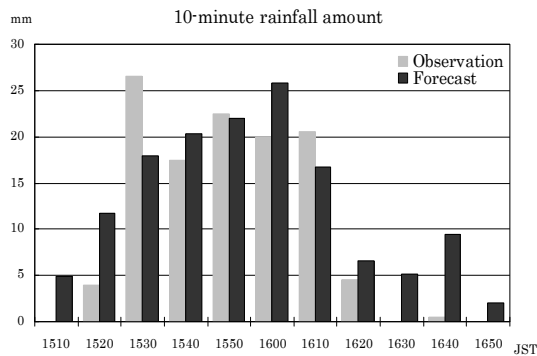
Fig. 3.2. Time series of 10-minute rainfall amount observed by AMeDAS observation (gray) at Nerima and the forecast result (black) at the point indicated by X in Fig. 3.15.
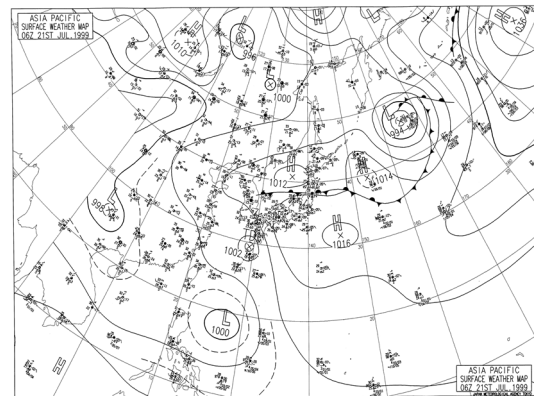
Fig. 3.3. Surface weather map at 15 JST 21 July 1999.
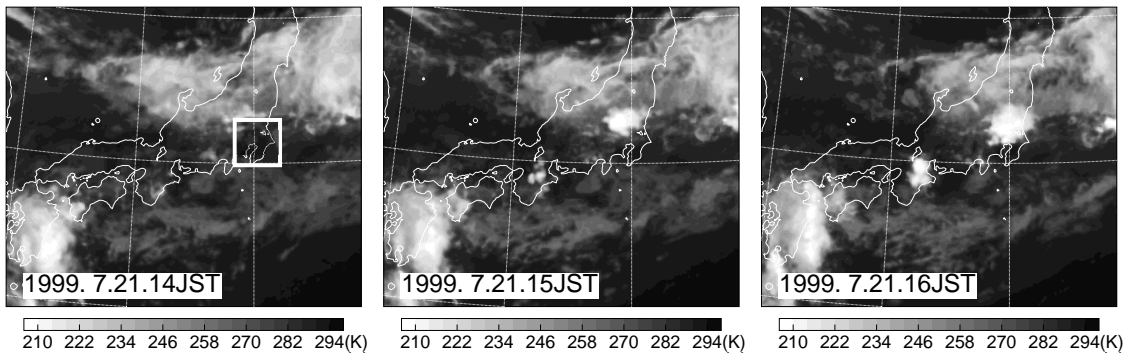
Fig. 3.4. Infrared satellite imaged observed by GMS-5 from 14 to 16 JST 21 July 1999. A white square shows the Kanto plain.

46
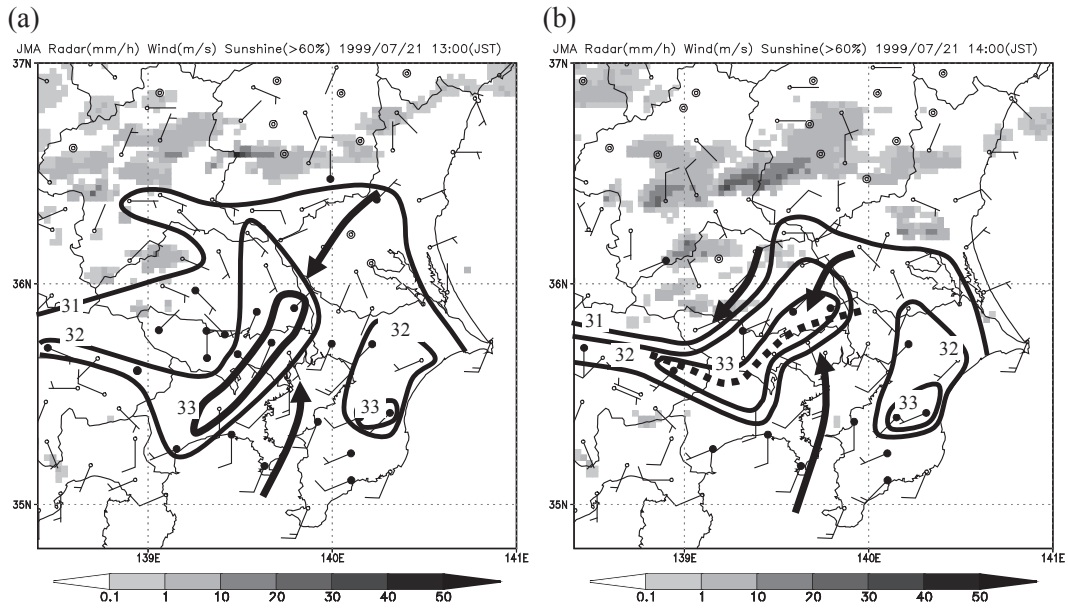
Fig. 3.5. Rainfall intensity estimated by JMA Radar and surface observation by AMeDAS. Rainfall intensity (shade), sunshine over 60% (black circles), temperature over 31, 32 and 33°C (contour) and convergence line (dashed line) are indicated. Double circles show the AMeDAS points which observed only rainfall amount. (a) 1300 JST. (b) 1400 JST.
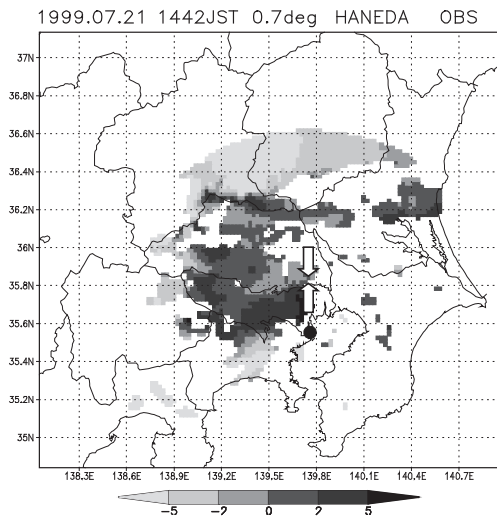
Fig. 3.6. Radial wind field estimated by the Doppler radar observation at the Haneda airport (●) at 1442 JST (generation stage of Nerima cells). The elevation angle is 0.7°. White arrows show the wind direction around the formation point of the Nerima cells.

The surface weather map at 15 JST 21 July 1999 is shown in Fig. 3.3. Two high pressure zones are found over the Pacific Ocean and the Sea of Japan, and the Baiu front extends in an east-west direction across the north of Japan. Figure 3.4 shows the infrared satellite images between 14 JST and 16 JST, observed by GMS-5. Any strong convective activity is not found around the Baiu front at 14 JST. A deep convective cloud system rapidly formed at 15 JST over northern Kanto Plain. The MCS that formed at the southern edge of this system caused the Nerima heavy rainfall.

Figure 3.5 shows the rainfall intensity (mm h^{-1}) estimated from JMA operational radar observations, surface winds, temperature and sunshine over the Kanto plain, observed by AMeDAS at 1300 JST and 1400 JST. A surface wind convergence line formed in the southern part of the Kanto plain between 1300 and 1400 JST. This convergence line is also ascertained in the radial wind field estimated from the Haneda Doppler radar data (Fig. 3.6). Here, its formation mechanism is examined. A weak convergence of horizontal winds was found between southerly sea breeze from the Tokyo

47

bay and northeasterly winds from north-east of the Kanto plain at 13 JST (Fig. 3.5a). Moreover, the surface temperature exceeded 33°C due to strong solar radiation around the convergence zone. However, since weak precipitation areas in the north part of the Kanto plain moved southward at 14 JST, the surface temperature fell around there (Fig. 3.5b). The difference of the surface temperature on the convergence line and its north side became about 3 K. Therefore, the wind convergence around Nerima was enhanced. At 1430 JST, the rainfall was observed at Nerima on the convergence line. After then, the rainfall intensity became strong, and the rainfall area stagnated around Nerima until 1600 JST (not shown).

3.3 Assimilation and forecast experiment

In order to reproduce the Nerima cells, 2km-NHM (Fig. 3.10c) is nested within the forecasts of 5km-NHM (Fig. 3.10b). 5km-NHM is also nested within the forecasts of the MSM (Fig. 3.10a). The initial times of 2km-NHM and 5km-NHM are 11 JST and 10 JST on 21 July, respectively. Schematic view of nesting area is shown in Fig. 3.10. The initial condition of the MSM is provided from the Meso 4D-Var which assimilated the conventional observations, and its initial time is 09 JST on 21 July. 2km-NHM cannot reproduce the Nerima heavy rainfall and other intense precipitation areas (Fig. 3.7). This is because low-level southern winds (sea breeze) spread over the Kanto plain and the convergence line is not reproduced (Fig. 3.8). This failure could be brought from the unsuitable initial condition. In order to improve the initial condition, an assimilation experiment with NHM-4DVAR is conducted. The first guess of NHM-4DVAR is given from the 4-hour forecast of 2km-NHM (14 JST) and its boundary condition is given from the 4-5 hours forecasts of 5km-NHM.
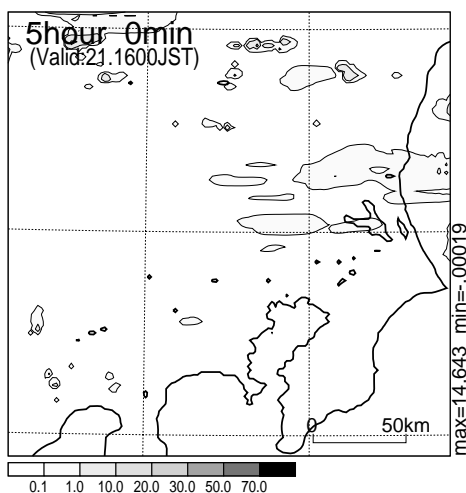
Fig. 3.7. Simulated distribution of hourly accumulated rainfall amount by the 2km-NHM at 16 JST 21 July 1999, corresponding to Fig. 3.1b.
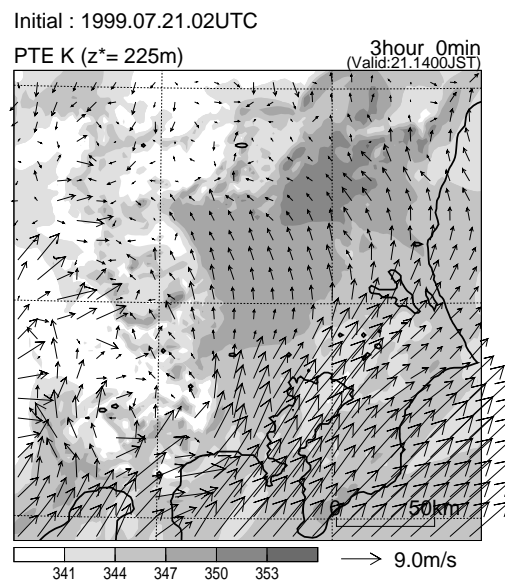
Fig. 3.8. Horizontal distribution of wind and equivalent potential temperature at 1400 JST from the forecast result of the 2km-NHM.

3.3.1 Design of the assimilation experiment

The design of the assimilation experiment and the evolution stage of the Nerima cells are shown in Fig. 3.9. The assimilation window was set to one hour between 14 and 15 JST 21 July 1999. This time window includes the formation stage of the Nerima cells, but not their development and mature stages. The assimilation area (Fig. 3.10) covers the Kanto plain. The number of horizontal grids is 122×122 (about 240 km × 240 km). The vertical grid with a terrain-following coordinate contains 40 levels with variable grid intervals of 40 m near the surface to 1092 m at the top of domain, and the model top is located at about 22 km. After 15 iterations to minimize the cost functions, a 3-hour forecast from 14 JST was performed by 2km-NHM.

Both the results of 'Assimilation result' and 'Forecast result' are examined in the following subsections. The 'Assimilation result' is from the forward model of NHM-4DVAR. Since NHM-4DVAR provides the initial condition optimized for JMA-NHM, which is constrained by the
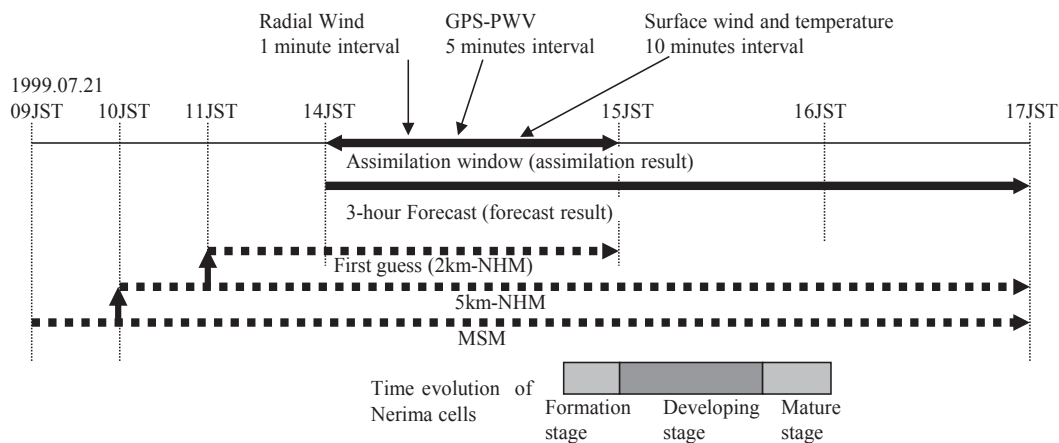
Fig. 3.9. Design of the assimilation experiment: Assimilation window, forecast time, first guess. Time evolution of Nerima cells is also indicated.
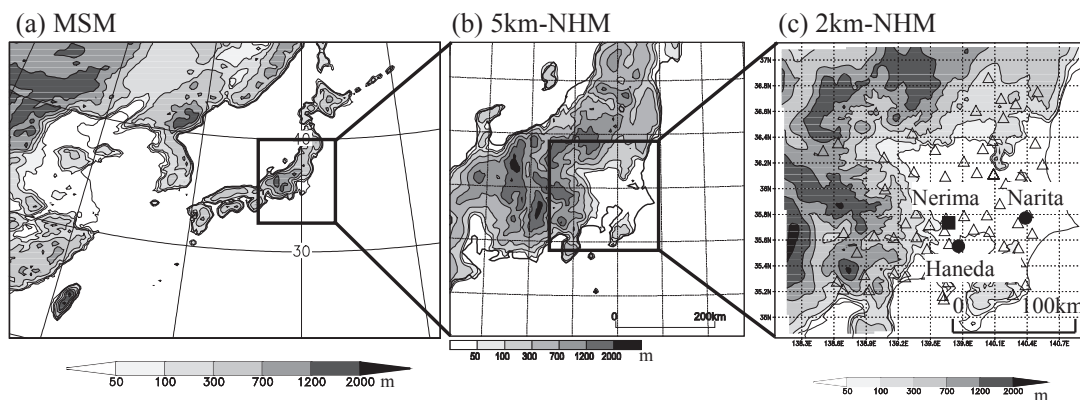
Fig. 3.10. Model domain and orography. (a) MSM. (b) 5km-NHM. (c) 2km-NHM and assimilation area. Observation stations: Nerima AMeDAS station (■), the Haneda and the Narita airport Dopplar radars (●) and the GPS-PWV observation stations (Δ).

observational data and the background field, JMA-NHM starting from the initial condition can provide the best simulation. Namely, the 'Assimilation result' is from the simulation which is constrained by the optimized initial condition and the optimized lateral boundary condition in the assimilation window (14–15 JST). On the other hand, the 'Forecast result' is from a 3-hour forecast (14–17 JST, including assimilation window) by 2km-NHM. This simulation is constrained by the optimized initial condition but the lateral boundary condition provided by 5km-NHM. Since a very short range forecast is mainly determined by the initial condition, the effect of the lateral boundary condition is small. Therefore, both results are very similar. In this study, the 'Assimilation result' is called 'analysis field', and it is verified by comparison with the observation. The 'Forecast result' is used to investigate the formation mechanism of Nerima heavy rainfall, because this result provides a continuous time sequence of the Nerima cells. For assimilated observation data, the locations of the Nerima AMeDAS station, the Haneda airport, the Narita airport and GPS-PWV observation stations are also shown in Fig. 3.10c. AMeDAS stations except for NERIMA are not shown.

3.3.2 Assimilation result

In this section, the variation of the cost functions of 4DVAR is described, and the analysis field is compared with the observations.

The variation of the cost function J corresponding to iteration numbers is shown in Fig. 3.11. Total value of J decreases in logarithmic decrement and reaches 40% of original value at the end of iterations. Most part of this decrease is brought from that of the cost function of RW data, because the number of RW data is large and the variables in dry dynamics is more easily to be optimized by the assimilation than those in other processes. The cost function of GPS-PWV data and the surface data decrease to about 30-80% of original value, respectively. The order of each cost function is the same as that of the number of each observation. These results indicate that the minimization process successfully converged by 14 iterations. Therefore, the estimated initial condition reaches the optimized condition, and the results after 14 iterations are used as 'Assimilation result' in this study.

Figure 3.12 show s analysis field of RW. Although the convergence of horizontal winds is not found at the formation point of the Nerima cells in the first guess field (Fig. 3.8), it is reproduced well in the analysis field (Fig. 3.12), almost corresponding to the observation (Fig. 3.6). The analysis field of surface winds and the observation by AMeDAS are shown in Fig. 3.13. These differences are very small. Moreover, the convergence of the southerly sea breeze from the Tokyo bay and the northerly winds from the north of the Kanto plain is reproduced well in the analysis field. The amount of GPS-PWV is large (> 60 mm) over northern Kanto plain (Fig. 3.14). The analysis field of PWV almost agrees with the observation. Since the amount of GPS-PWV of the background field in the central part of the Kanto plain is about 5 mm smaller than that of the observation (not shown), the assimilation of GPS-PWV data improves the moisture field of the background. These results indicate
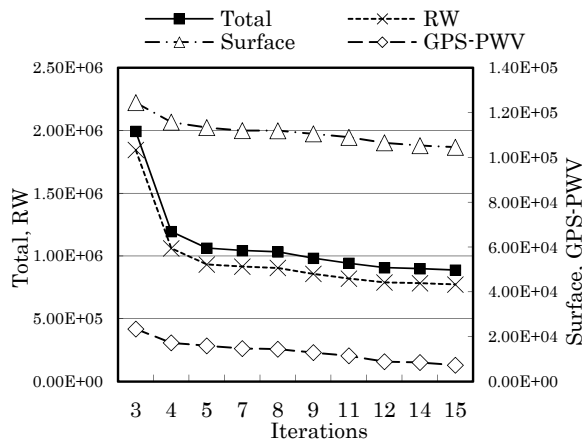
Fig. 3.11. Cost function *J*. Left Y-axis is a scale for the total value of J and the value of RW term. Right Y-axis is a scale for the values of the surface observation term and GPS-PWV term.
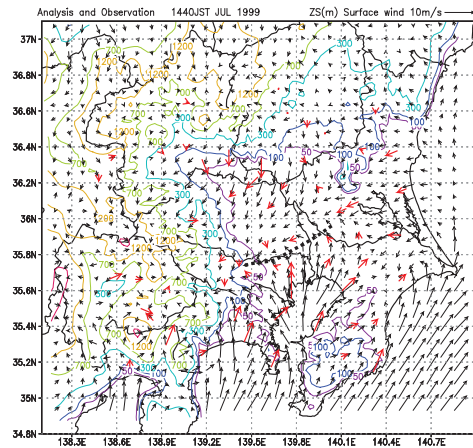
Fig. 3.13. Surface wind field of the observation (red arrows) and the analysis (black arrows) at 1440 JST. Color contours show the model orography. Dotted line indicates the wind convergence line.
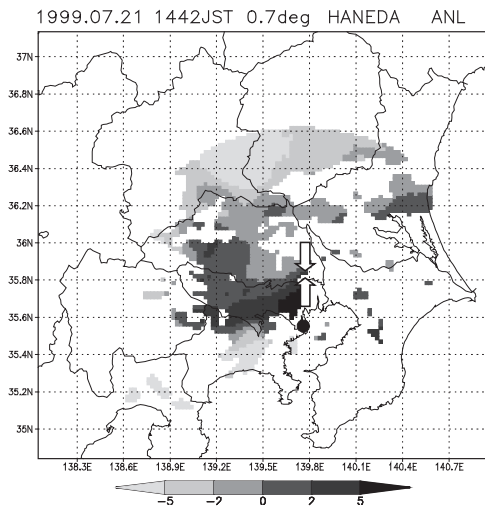
Fig. 3.12. Same as Fig. 3.6, but the analysis field of radial winds.
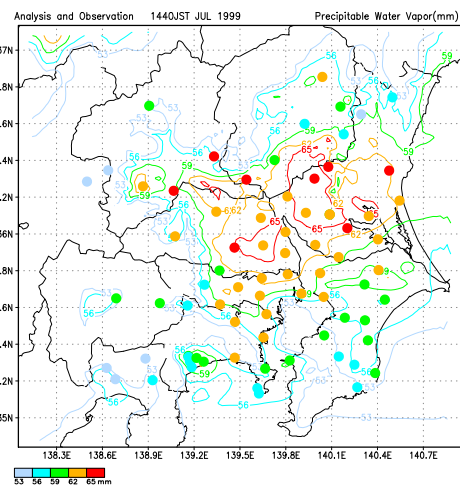
Fig. 3.14. Distribution of PWV in the observation (circles) and the analysis (contours) at 1440 JST.

that low-level winds and water vapor are reproduced well in the analysis fields.

RW data are the most important for this experiment; because the most part of total cost function is determined by the cost function of RW data. Moreover, GPS-PWV data are important as well. This is because a sensitivity assimilation experiment without GPS-PWV data cannot reproduce the Nerima cells (not shown). In contrast, the surface observation data are relatively less important, because the Nerima cells are reproduced in a sensitivity assimilation experiment without surface observations (not shown). However, the assimilation of surface data improves the location and formation time of the Nerima cells.

51

3.3.3 Forecast result

The 3-hour forecast from 14 JST, 'Forecast result', is examined to clarify the formation and development processes of the Nerima cells.

First, the simulated rainfall amount is compared with the observed one Fig. 3.1b. The intensity and area of the Nerima heavy rainfall are well reproduced (Fig. 3.15), although its location is slightly north compared with the observation. Other intense precipitation areas (**I**, **II** and **III**) are also reproduced, although the precipitation intensities of **I** and **II** are weaker and that of **III** is stronger. The point denoted by a cross in Fig. 3.15 shows the formation place of the Nerima cells, near the Nerima AMeDAS station. Black bars in Fig. 3.2 show the time sequence of 10-minute rainfall amount, simulated by 2km-NHM, at this point. Time variation is quantitatively in good agreement between the observation and the forecast. These results induced rainfall amount are well reproduced.
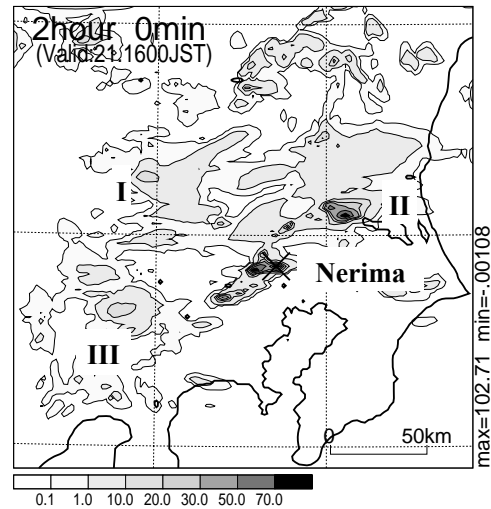
Fig. 3.15. Same as Fig. 3.1, but the forecast result at 16 JST (FT=2). The time series of 10-minute rainfall amount at point X is shown in Fig. 3.2.

Next, we focus on the formation and the development processes of the Nerima cells. Before the comparison, the observed features of MCSs are described with the radar reflectivity observed by the Haneda airport radar (Fig. 3.16a). As mentioned in the introduction (Section 3.1), the horizontal scale of MCS, consisting of the Nerima cells, was very small (about 30 km). The Radar-AMeDAS analyzed rainfall with a 5-km horizontal resolution cannot resolve the detailed structures of the Nerima cells. Thus, the radar reflectivity fields are used instead of the Radar-AMeDAS analyzed rainfall. Figure 3.16a shows the reflectivity fields from 1448 to 1545 JST. A small MCS denoted by **A** formed with a circular shape at Nerima along the wind convergence line at 1448 JST. The MCS **A** that had a circular shape in the formation stage extended westward until 1507 JST. The other MCS **B** formed north of the MCS A at 1507 JST and extended to northwestward. On the southwest side of these MCSs, the MCS C formed along the wind convergence line at 1525 JST. These MCSs produced the heavy rainfall area around Nerima (Fig. 3.1b).

The observed features of MCS **A** that caused the heavy rainfall at Nerima are examined in detail. At 1507 JST, a new radar echo appeared west of the echo at 1448 JST. This evolution of MCS **A** indicates that the MCS **A** consisted of more than 2 cumulonimbi though its horizontal scale was about 30 km. These facts suggest that the MCS **A** had a multi-cell structure. Although the distributions of radar echoes does not clearly show the multi-cell structure near Nerima, two peaks of rainfall intensity were observed at Nerima at 1530 JST and 1550 JST (Fig. 3.15). This variation of rainfall intensity supports the multi-cell structure of MCS **A**.
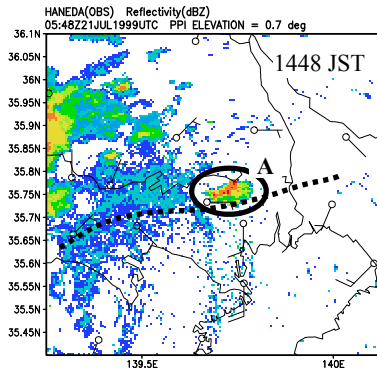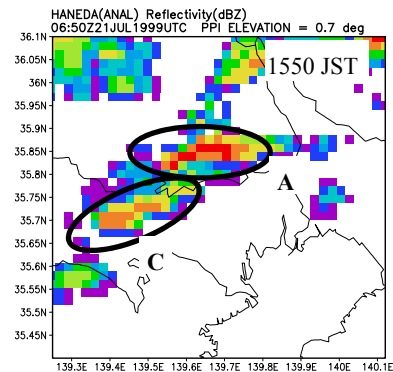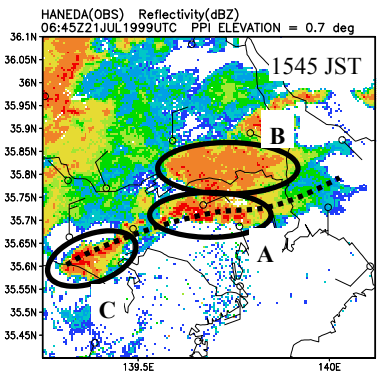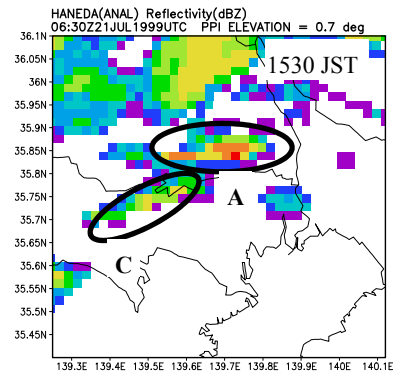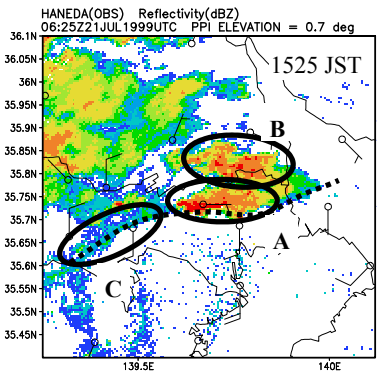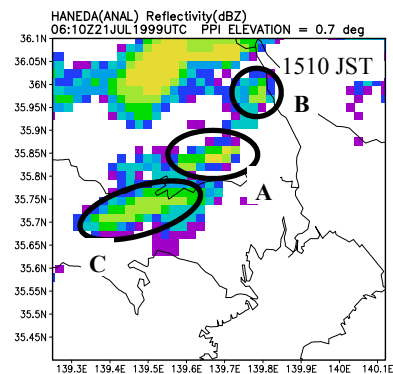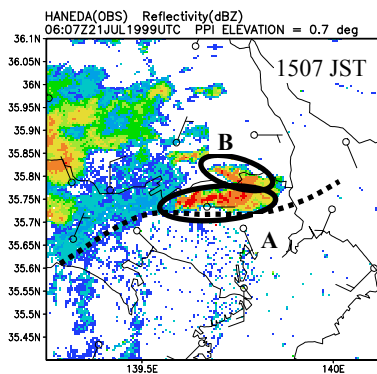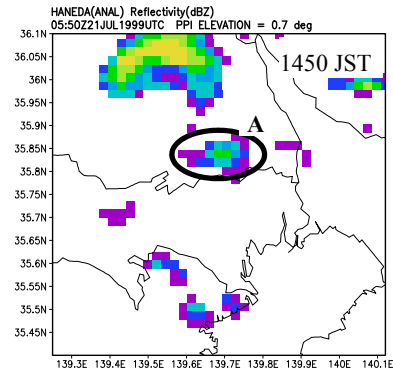
Fig. 3.16. Radar reflectivity (dBZ) at a 0.7° elevation angle. Black circles indicate MCSs. (a) Observations by the Haneda airport radar and observed surface wind by AMeDAS (arrows). Dotted line denotes the convergence line. (b) Forecast results. Symbols of A, B and C denote MCSs.

53

In the forecast result (Fig. 3.16b), the MCS **A** forms at the same time, but its location is a little north in comparison with the observation (Fig. 3.16a). At 1530 JST, two intense rainfall areas are found in the MCS **A**, as in the observation. The MCS **B** also forms north of the MCS **A**, but it does not develop in the forecast. The MCS **C** forms at 1510 JST and develops with a line-shaped structure, same as the observation.

It should be noted that 'non-precipitation echoes', such as blue-colored echoes around the MCS **A** at 1450 JST (Fig. 3.16a), is important to reproduce the Nerima cells in NHM-4DVAR. The 'non-precipitation echoes' are called also as 'clear air echoes'. They are reflected by some objects (e.g., insects). By these echoes, information of a wind field before the formation of the Nerima cells is provided as well as a surrounding wind field after the formation of the Nerima cells is provided. It should be noted that the information of horizontal wind in the non-precipitation echoes is also useful to reproduce the formation process of MCSs.

The environmental fields for the formation of the Nerima cells are examined. Figure 3.17 shows the horizontal distribution of potential temperature, horizontal winds and pressure before the formation of the Nerima cells. At 1410 JST, the wind convergence line forms around the formation point of the Nerima cells between the southerly sea breeze and the northerly winds. The potential temperature on the convergence line is higher than that in surrounding areas, and a low pressure zone is simulated along the convergence line. These features agree with the observation (Fig. 3.6 in Seko et at. 2007). The intensification of this convergence line is shown in Fig. 3.18. A white area in this
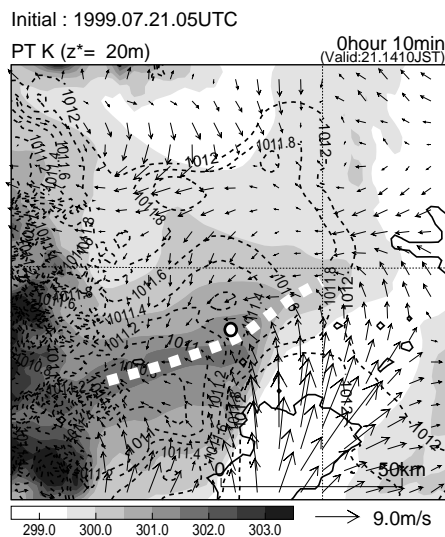
Fig. 3.17. Horizontal distribution of potential temperature (shade), horizontal wind (arrows) at a height of about 20 m from the ground and sea level pressure (dotted contours in hPa) at 1410 JST. White dotted line indicates the convergence line and white circle indicates the formation point of Nerima cells.
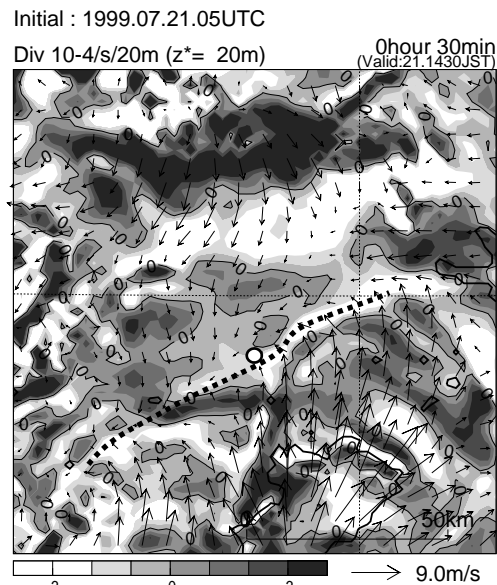
Fig. 3.18. Horizontal distribution of the difference of wind divergence between at 1410 JST and 1430 JST. Dotted line and white circle indicate the convergence line and the formation point of Nerima cells respectively same as Fig. 3.17, but at 1430 JST.

(a) Initial : 1999.07.21.05UTC

PTE K (z*= 686m)   0hour 10min (Valid:21.1410JST)

(b)

PTE K (z*= 225m)   0hour 10min (Valid:21.1410JST)
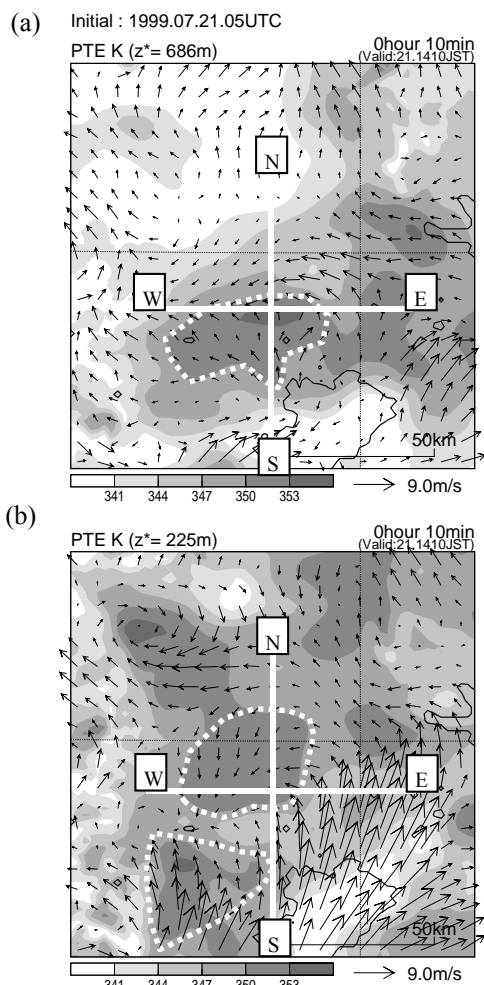
Fig. 3.19. Horizontal distribution of equivalent potential temperature (shade) and horizontal wind (arrows) at 1410JST at heights of (a) 685m and (b) 225m. White dotted lines show high equivalent potential temperature areas discussed in this study. Vertical cross sections along line S-N is shown in Figs. 3.20 and 3.21 and that along line W-E in Fig. 3.22.

Initial : 1999.07.21.05UTC

PTE K (70, 70- 34, 74x 2km)   0hour 10min (Valid:21.1410JST)

Fig. 3.20. Vertical cross sections of equivalent potential temperature (shade) and winds projected on the cross section (arrows) at 1410JST along (a) the line S-N in Fig. 3.19.

figure indicates the place where the horizontal wind convergence becomes stronger between 1410 JST and 1430 JST. Especially, on the east and south sides of the formation point of the Nerima cells, the wind convergence is intensified more than that on the west side. This intense convergence is one of reason why the Nerima cells formed there.

The formation mechanisms of the Nerima cells are examined from the distribution of equivalent potential temperature (θ_e) and the convergence of near-surface winds, because cumulonimbi usually form by a high θ_e air being lifted from the low level over the wind convergence zone. Figure 3.19 shows the distribution of θ_e and the horizontal winds at heights of about 686 m and 225 m from the ground

at 1410 JST. A large area with θ_e higher than 350 K exists around the convergence line of surface wind at a height of about 686 m (Fig. 3.19a). Such area exists more widely at a height of 225 m (Fig. 3.19b), although it is separated on the south and north sides of the wind convergence. These characteristics are not shown in the background field (Fig. 3.8), and the assimilation of RW and GPS-PWV data improves the low level wind field and the moisture field in the forecast result.

Next, the vertical distribution of high θ_e air is investigated with the vertical cross section of θ_e along the line S-N in Fig. 3.19 (Fig. 3.20). The line S-N crosses the formation point of the Nerima cells, and shows that the distribution of θ_e higher than 350 K is mountain-shaped, its top is located at

55

Initial : 1999.07.21.05UTC

PTE K (70, 70- 34, 74x 2km) — 0hour 30min (Valid:21.1430JST)

PTE K (70, 70- 34, 74x 2km) — 0hour 40min (Valid:21.1440JST)

PTE K (70, 70- 34, 74x 2km) — 0hour 50min (Valid:21.1450JST)

PTE K (70, 70- 34, 74x 2km) — 1hour 0min (Valid:21.1500JST)

Axis labels: 2 (km), 1, 1.0m/s, 8.0m/s, 338 341 344 347 350, 0 20km, S, N

Fig. 3.21. Same as Fig. 3.20, but along line S-N in Fig. 3.19 from 1430 JST to 1500 JST. Contours show the mixing ratio of total water (cloud water, rain water, cloud ice and hail (g kg^{-1})).

Initial : 1999.07.21.05UTC

PTE K (50, 90- 54, 54x 2km) — 1hour 10min (Valid:21.1510JST)

PTE K (50, 90- 54, 54x 2km) — 1hour 20min (Valid:21.1520JST)

PTE K (50, 90- 54, 54x 2km) — 1hour 30min (Valid:21.1530JST)

PTE K (50, 90- 54, 54x 2km) — 1hour 40min (Valid:21.1540JST)

Axis labels: 12 (km), 10, 8, 6, 4, 2, 10.0m/s, 32.0m/s, 338 341 344 347 350, 0 20km, W, E
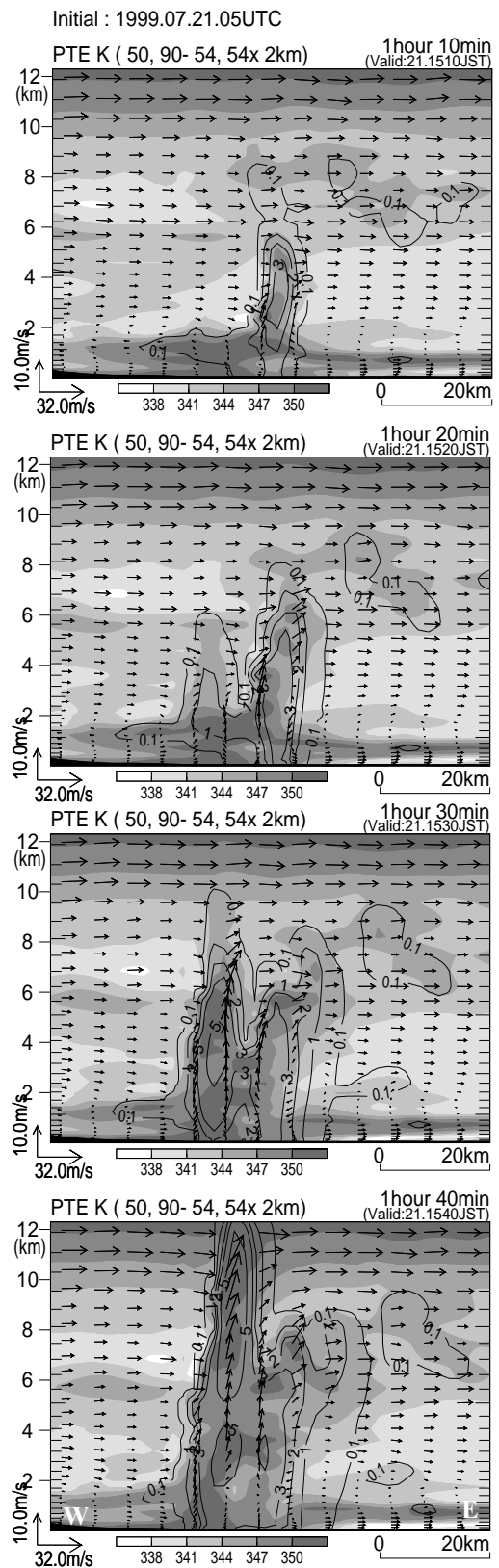
Fig. 3.22. Same as Fig. 3.21, but along line W-E in Fig. 3.19 from 1510 to 1540 JST.

a height of about 1,200 m. The intense convergence of low level wind is produced by the southerly sea breeze, which lifts up a high θ_e air on the north of the convergence line. Figure 3.21 shows the vertical cross section of θ_e and the mixing ratio of the total water on the line S-N from 1430 JST to 1500 JST. A high θ_e air is lifted over the convergence line. At 1440 JST, a cloud forms there and develops to a cumulonimbus (hereafter, the first cell) with the top over 3,000 m at 1500 JST.

Figure 3.22 show the vertical cross section of θ_e and the mixing ratio of the total water on the line W-E in Fig. 3.19 from 1510 JST to 1540 JST. At 1510 JST, the first cell reaches the altitude of 8,000 m and it moves eastward by middle-level westerly winds (Fig. 3.22). At 1520 JST, the northerly winds on the north part of the convergence line have the westerly component due to the development of the first cell. A new cumulonimbus (hereafter, the second cell) is simulated west of the first cell over the near-surface convergence between the northerly winds and the out flow from the cumulonimbus. At 1540 JST, down drafts appear at the low level of the second cell. This variation of the vertical velocity indicates that the second cell is in the mature stage. Since the inflow of high θ_e air continues to flow into the wind convergence line, the second cell sustains its intensity until 1600 JST. These cells organize a MCS with the horizontal scale of about 30 km as well as the observation.

3.3.4 Assimilation-forecast cycle experiment

As described in Section 3.3.3, the precipitation intensity in the rainfall areas **I**, **II** and **III**, shown in Fig. 3.15, were not well reproduced. In order to improve the forecast, an additional assimilation experiment is conducted by using the observation in 15–16 JST. The first guess of this experiment was the result of the 1-2 hour forecast from 1400 JST by 2km-NHM. In other words, this experiment should be called the forecast-analysis cycle experiment. The design of this assimilation experiment is shown in Fig. 3.23. The same kinds of observations were assimilated with same interval, as those described in Section 3.3.1. The experiment explained in the last section is referred to as 'standard experiment'.

Figure 3.24 shows the simulated distribution of hourly accumulated rainfall amount by this experiment. The Nerima cells are reproduced southwest in comparison with those of the standard experiment (Fig. 3.15), which are closer to the observation (Fig. 3.1b). The precipitation intensity in the rainfall area **I** and **II** are stronger, and that of other rainfall area **III** is similar in comparison with the standard experiment (Fig. 3.15). Another area **IV** with intense rainfall is mistakenly simulated, because no strong rainfall is found there in the observation. This additional experiment suggests that the rainfall areas of **I**, **II** and **III**, which were not well reproduced in the standard experiment, become closer to the observed ones by the assimilation of the long period data.

Next, the reason why the reproduction of rainfall areas of **I**, **II** and **III** is more difficult is mentioned. The environmental wind fields before the formation of the Nerima cells, which were reproduced in the standard and the additional experiments, seems to be simple. On the other hand, the
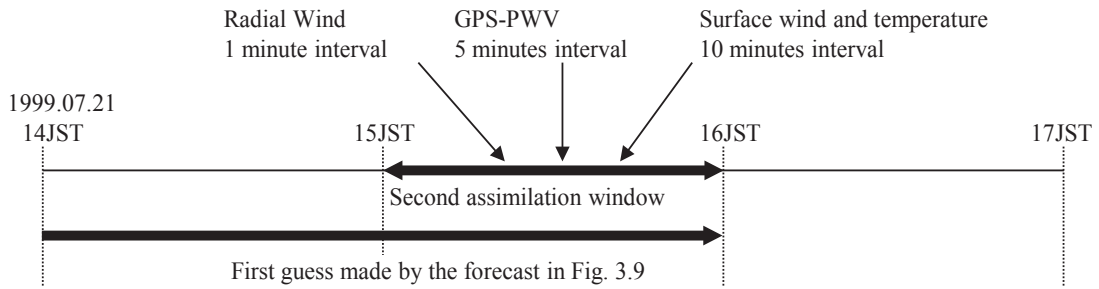
Fig. 3.23. Design of the additional experiment.

wind fields in the MCSs are complex because of the updraft and the downdraft regions existed in one cumulonimbus. It is deduced that the simple environmental wind fields before the formation of the MCSs can be reproduced more easily than that in the developed MCSs. Considering about available observation network, it seems to forecast these cells is not easy. We did not make a detailed analysis of the additional assimilation result, because our objective is to investigate the formation and mechanism of the Nerima cells. Effect of forecast-analysis cycle in NHM-4DVAR is a subject in the future study.

Fig. 3.24. Same as Fig. 3.15, but for the additional experiment. Symbol of **IV** indicates another intense rainfall area.

3.4 Summary

In this case study, it was first shown that a meso β-γ scale MCS can be accurately predicted using a storm-scale 4D-Var with high-dense remote sensing observations. The formation and development mechanisms of the Nerima heavy rainfall, which observed on 21 July 1999 in the central part of Tokyo, were examined through the observations and the assimilation experiments. For this purpose, a horizontal resolution of 2 km and the assimilation window of 1 hour are adopted. The MCS that caused the Nerima heavy rainfall had the horizontal scale of about 30 km, and it formed without the synoptic-scale convergence and the terrain effect. Since the Meso 4D-Var with a horizontal resolution of 20 km based on the hydrostatic model is difficult to reproduce the environmental field in such MCSs, JMA-NHM with a horizontal resolution of 2 km (2km-NHM) cannot reproduce this heavy rainfall with the initial condition from the Meso 4D-Var. On the other hand, NHM-4DVAR can resolve MCSs and assimilate observations with the high temporal and horizontal resolution. The intensity and areas of this heavy rainfall are reproduced well and the simulated rainfall amount is quantitatively in good agreement with the observation.

58

For the reproduction of the Nerima cells, the assimilations of RW data and GPS-PWV data are more important than those of surface wind and temperature observations. Especially, the non-precipitation echoes observed by the Doppler radar is important to improve the environmental wind field, because they provides the information of wind fields before the formation of the Nerima cells and those around the Nerima cells after the formation.

The formation mechanisms of the Nerima heavy rainfall were examined form the observations and the result of 2km-NHM with the initial condition produced by NHM-4DVAR. The surface wind convergence line formed of the southerly sea breeze and northeasterly winds around Nerima. The surface temperature around the convergence line was higher than that in the surrounding areas, because the raise of temperature was suppressed north of the convergence line due to the shield of clouds from sunshine. Therefore, the wind convergence was enhanced due to the low pressure zone that was produced from high temperature. Over this enhanced convergence, a high θ_e air that existed there was lifted to generate a cumulonimbus. The second cumulonimbus formed on the west side of the pre-formed cumulonimbus. These cumulonimbi developed and organized the MCS that induced the Nerima heavy rainfall.

The location of the Nerima cells is simulated north in comparison with the observation. Since the low-level wind field of the analysis is well reproduced, the distribution of high θ_e airs may not be well reproduced in the initial field due to the unsuitable analysis of surface temperature. This is because the parameterization scheme of the surface-air interaction process is not implemented in the adjoint model of NHM-4DVAR. Moreover, the rainfall areas of **I**, **II** and **III** are not well reproduced in the standard experiment. In order to improve this result, the precipitation process should be also introduced to NHM-4DVAR and assimilate the observation of the radar reflectivity.

Chapter 4

Assimilation Experiment using NHM-4DVAR v2

with Radar Reflectivity Data

- Suginami Heavy Rainfall Event on 4-5 September 2005 -

This chapter discusses a case study on the Suginami heavy rainfall event occurred in the Tokyo metropolitan area on 4-5 September 2005 using NHM-4DVAR v2 (see Section 2.3) with the observation operator of radar reflectivity (see Section 2.4.4), Doppler radial wind and GPS precipitable water vapor. The improvement of quantitative precipitation forecast is described, and a sustainment mechanism of MCSs is discussed. The 4D-Var assimilation reproduces a line-shaped rainband with a shape and intensity consistent with the observation. Assimilation of radar-reflectivity data intensifies the rainband and suppressed false convection. The simulated rainband lasts for 1 h in the extended forecast and then decays gradually. The low-level convergence sustained by northerly winds in the western part of the rainband is a key to prolong the predictability of the convective system. The result illustrates that assimilating rain water alone is not sufficient for improving forecast skill of long-lasting MCSs due to nonlinearity. This means that observing and assimilating environmental information outside MCSs are more important to extend predictability of MCSs.

4.1 Introduction

Radar observations provide the most useful data for high-resolution assimilation systems because radars are deployed at many observation sites and can capture MCSs with high temporal and spatial resolution. One of the most important radar observational elements is Doppler radial winds (hereafter RW). Most MCSs are induced by the low-level convergence of water vapor. Therefore, detecting low-level convergence is key to successfully predicting MCSs. The assimilation of RW contributes to the reproduction of low-level wind fields. Another important observational element of radars is

reflectivity. Various methods of using reflectivity for cloud scale assimilation have been examined.

The simplest method for assimilating reflectivity may be to nudge the rain-water produced by the model toward that retrieved from the observed reflectivity. Sokol and Rezacova (2009) assimilated radar reflectivity to Local Model COSMO (Doms and Schaettler 1999) using a nudging method that converted the reflectivity to latent heating, and succeeded in simulating MCSs for several hours. However, with the nudging method, the impact of assimilation usually does not continue for a long time, and the assimilated rain water sometimes vanishes too soon because dynamical and thermodynamical balances are neglected.

Xiao et al. (2007) developed a three-dimensional variational assimilation system (3D-Var) to directly assimilate radar reflectivity. By applying cloud microphysics in the conversion process between the model prognostic variables and control variables in MM5-3DVAR (Barker et al. 2004) with 10-km grid spacing, they were able to improve the forecast of a typhoon. 3D-Var is more sophisticated than the nudging method and can directly assimilate radar reflectivity. However, 3D-Var cannot consider model dynamics in the assimilation procedure.

The pioneers of radar-data assimilation in the cloud scale are Sun and Crook (1997; 1998). Sun and Crook (1997) developed a 4D-Var system called VDRAS (variational Doppler radar analysis system) to assimilate radar reflectivity and RW with an anelastic nonhydrostatic model. They demonstrated the impact of the radar data assimilation using an Observation System Simulation Experiment (OSSE). Their system reproduced winds, thermodynamics, and cloud microphysics fields well. Sun and Crook (1998) applied their system to an actual convective storm, and reported good agreement between the simulation and aircraft observations. However, in their experiment, they used a uniform horizontal field as the initial condition, and convection was first initiated by an artificial warm bubble. Only 5 and 7-min assimilation windows were adopted in a narrow experimental domain of 11.2 km^2, and orography was not considered in the model. Their studies were the first trial of radar-data assimilation in a cloud-scale 4D-Var, but the experimental configurations were unable to support actual full-scale short-range forecasts of local convective rainfall.

Snyder and Zhang (2003) reported the potential of an ensemble Kalman filter (EnKF) for use in radar data assimilation. They used 50 members of the numerical model of VDRAS with 2-km horizontal grid spacing and assimilated radial wind and reflectivity observations with 5-min intervals. The EnKF reduced the analysis error during assimilation cycles and reproduced unobserved variable fields. Xue et al. (2006) also used the EnKF technique to assimilate radar reflectivity data directly with a horizontal resolution of 1.5 km as an OSSE. Aksoy et al. (2009) attempted to assimilate radial wind and reflectivity data obtained by actual radar observations from WSR-88D into an EnKF, which consisted of 50 members of the WRF model with 2-km horizontal grid spacing, and obtained reasonable analysis results for their experiment cases.

Recently, Sun and Zhang (2008) assimilated radar reflectivity from multiple Doppler radars using VDRAS improved in a number of ways with 4-km grid spacing. In their experiment, the forecast of a squall line 4 h after the initial time was improved compared with the background fields, but the reproduced squall line had a horizontal scale of 300 km and was thus more predictable than a local heavy rainfall event.

Kawabata et al. (2007) developed a cloud-resolving 4D-Var based on the JMA nonhydrostatic model (NHM-4DVAR). Although the adjoint model included only dry dynamics and advection of water vapor, they succeeded in reproducing observed cumulonimbi by assimilating RW and GPS-PWV data. Their study was the first to demonstrate the feasibility of short-range forecasting of local heavy rainfall brought about by deep convection, using a full-blown numerical model and a dense observation network. They were able to successfully reproduce deep convection because the convection was initiated by the low-level convergence of a sea-breeze front, and low-level winds were observed by Doppler radars as clear-air echoes around the initiating point of the cumulonimbi. However, it should be noted that low-level features are not always observed by radar instruments.

To prevent disasters caused by heavy rainfall events, JMA issues 33-h mesoscale model (MSM) predictions 8 times a day, and 6-h kinematic very-short-range forecasts every 30 min. A merging method that integrates extrapolations of radar observations and forecasts by MSM with a weighting function is used in this kinematic forecast. It is very difficult, however, to predict convection initiation and decay by such methods. The aim of this study is to issue 2- to 6-h forecasts, because a kinematic forecast is useful only within 1-2 h.

On 4-5 September 2005, a local heavy rainfall event occurred in the Tokyo metropolitan area. A maximum total rainfall of over 200 mm was recorded in the western part of Tokyo. This event was caused by a small-scale line-shaped convective system about 100 km long and 15 km wide. As is discussed in Section 4.3, the Tokyo metropolitan area has a very high density of operational observation networks, including three Doppler radars, more than 30 GPS observation sites, over 30 automated surface-observation sites, and four wind profilers in an area of 150 km^2. We chose this event as a test case for an assimilation experiment of deep convection with a cloud-resolving 4D-Var system.

In this case study, we first modified NHM-4DVAR v1 to assimilate radar-reflectivity data directly, considering perturbations newly in rain water
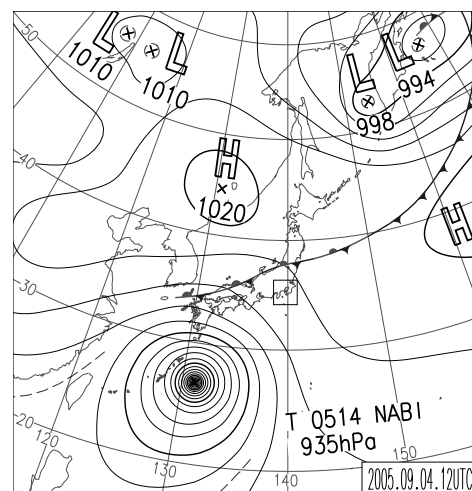
Fig. 4.1. Surface weather map on 2100 JST 4 September 2005. A small rectangular region indicates the assimilation experiment domain in this chapter.

63
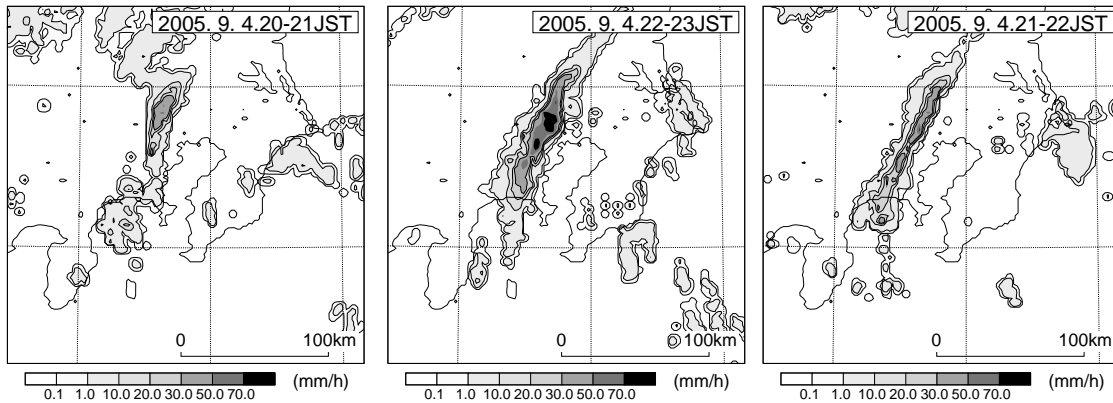
Fig. 4.2. 1-hour accumulated rainfall amount (mm h⁻¹) observed by the JMA operational radars.

and cloud water, and implementing an adjoint model of cloud microphysics (see Section 2.3). Then an observation operator for radar reflectivity was developed (See Section 2.4.4). Here, we demonstrate that radar-reflectivity assimilation with a cloud-resolving 4D-Var improves the reproduction of observed MCSs. In Section 4.2, overview of the event is described, and the results of the 4D-Var experiment is in Section 4.5. In Section 4.6, we discuss

Fig. 4.3. Accumulated rainfall amount during 1200-0600 JST on 4-5 September observed by the Tokyo metropolitan government.

the effect of assimilation of 0 dBZ information and the sustainment of the convective system. Section 4.7 consists of a summary and concluding remarks.

4.2 Overview of the event

An experiment based on actual observations was conducted for a heavy rainfall event that occurred around Tokyo on 4-5 September 2005. The assimilation-experiment domain, shown by the rectangle on a surface weather map (Fig. 4.1), covered the Kanto plain. A stationary front extended from north of Kyushu to the northern part of Japan. Typhoon 0514 (NABI) can be seen over the sea east of Okinawa, but the Kanto plain is 1,500 km away and was not directly affected by the typhoon. Since there were no distinct disturbances around the Kanto plain, meteorological forcing larger than meso α-β scale was weak.

Convective rainfall started in the Kanto plain around noon on 4 September. A line-shaped rainband (hereafter, L1) developed after 1800 Japan Standard Time (JST) on 4 September 2005 in the western part of Tokyo. The 1-h accumulated rainfall amounts from 2000 to 2300 JST are shown in

Fig. 4.2. The rainband, which was oriented north to south-southwest, gradually increased in intensity during this period.

Although, L1 was very small, about 100 km long and 15 km wide, it caused heavy rainfall in a narrow area in the southwestern part of the Tokyo metropolitan area. The maximum total rainfall [2000 to 2400 JST; observed by Automated Meteorological Data Acquisition System (AMeDAS) of JMA; average resolution about 17km] among rain-gage stations was 113mm at Nerima, whereas 10 observation points of local municipalities recorded over 200 mm. A surprising 264 mm was observed at Shimoigusa over 9 h from 2000 to 0500 JST on 4-5 September (Fig. 4.3). The Myoshoji River a branch of the Arakawa River, overflowed and more than 5000 houses were flooded up to their floorboards.

4.3 Observational data

Observations used in the experiment consisted of RW and reflectivity observed by the HANEDA and NARITA airport radars, GPS-PWV observed by GEONET (GPS Earth Observation Network System) of the GSI, vertical profiles of horizontal wind observed by wind profilers of the JMA, and sur-
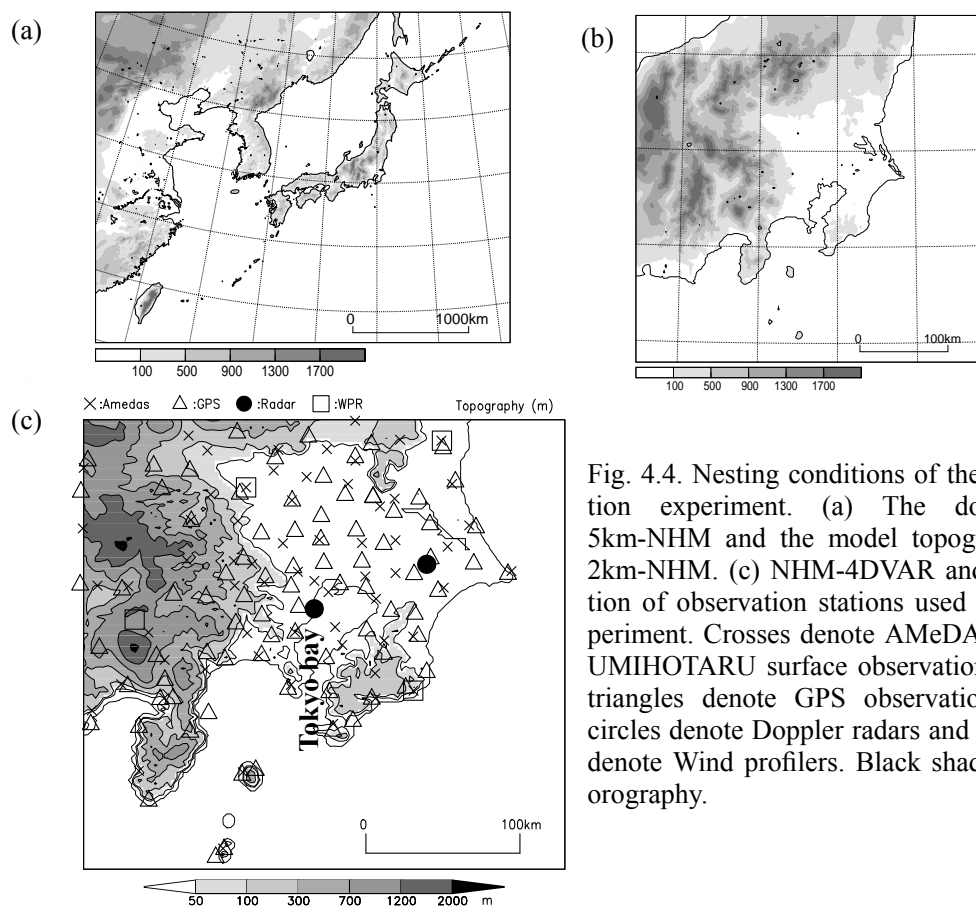
Fig. 4.4. Nesting conditions of the assimilation experiment. (a) The domain of 5km-NHM and the model topography. (b) 2km-NHM. (c) NHM-4DVAR and distribution of observation stations used in the experiment. Crosses denote AMeDAS and the UMIHOTARU surface observation stations, triangles denote GPS observations, black circles denote Doppler radars and rectangles denote Wind profilers. Black shade denotes orography.

face winds and temperature observed by AMeDAS and at UMIHOTARU (an observation site on Tokyo Bay monitored by the Ministry of the Environment of Japan). The locations of these sites are plotted in Fig. 4.4c.

The assimilation methods used in these experiments, except for radar reflectivity, are the same as those used by Kawabata et al. (2007). Radar data (RW and reflectivity) were assimilated at 1-min intervals for data of each level of elevation. GPS-PWV, processed by Shoji (2009), was assimilated at 5-min intervals, and surface and wind profiler data were assimilated at 10-min intervals.

RW can be expressed with 3-dimensional wind velocity components and the mean terminal velocity of water substances, (i.e., hail, graupel, snow, and rain droplets) in the numerical model. Although reflectivity was observed, there are uncertainties in the conversion from reflectivity to the mixing ratio of water substances. The melting of snowflakes in the melting layer also causes uncertainty. We assumed that the uncertainty in vertical velocity was up to 10 m s^{-1} and that the accuracy of the radial wind was around 1 m s^{-1}. When the uncertainty in the radial wind component of vertical velocity (10 m^{-1}) is less than the accuracy of radar beam velocity (1 m s^{-1}), the elevation angle is 5.7°. Therefore, the RW data for an elevation angle of less than 5.4° were used and was treated as horizontal winds instead of as radial winds (see Seko et al. 2004a) in this study. Data for a higher elevation angle will be used in our future studies.

Likewise, the reflectivity observations at high elevations of more than 5.4° were ignored because the high-elevation data are confined to small areas near radar sites. In a preliminary study, we confirmed that the impact of high-elevation-angle data on the forecast results is small.

4.4 Design of the assimilation experiment

First, a simulation by JMA-NHM with 5-km grid spacing (5km-NHM, Fig. 4.4a) was conducted from 0900 to 2400 JST on 4 September 2005 using the Meso-4DVAR analysis for the initial and boundary conditions. Second, a simulation by JMA-NHM with 2-km grid spacing (2km-NHM-L) was performed in a domain of about 400 km^2 (Fig. 4.4b) from 0900 to 2400 JST using the 5km-NHM forecast result for the initial and boundary conditions. Finally, a JMA-NHM simulation with 2-km grid spacing (2km-NHM-S) was conducted in the assimilation domain (244 km^2 ; Fig. 4.4c) from 1000 to 1200 JST using the 2km-NHM-L result for the initial and boundary conditions.

2km-NHM-S result was then used as the first-guess field at 1200 JST in the first assimilation window. A first guess of the lateral boundary conditions of NHM-4DVAR was given by the 2km-NHM-L forecast. As mentioned in Section 2.3.1, the same background covariance matrices can be used for **B** and **B**$_{lbc}$ with the same simulations in first guesses of the initial and lateral boundary conditions.

To minimize the effects of a coarse model, a forecast based on downscaled initial conditions

should be started several hours before the short-range forecast experiment and forecast-analysis cycles have been made. Since a forecast based on downscaled initial conditions failed badly in the forecast of convection (see Fig. 4.7a and d), it is better to set the start time of the cycle during a period of calm weather.

Fig. 4.5. Schematic of the assimilation experiment.

For the above reasons, eight analysis-forecast cycles were performed from 1200 to 2000 JST with 1-h assimilation windows using NHM-4DVAR. In these spin-up windows, considering computation costs, the number of iterations for minimizing J was limited to 10. Since there were few convection areas during the first half of this period, only observations of RW, GPS-PWV, surface observations, and wind profiler data were assimilated until 1800 JST. Radar reflectivity was added between 1800 and 2000 JST.

After the spin-up process, two assimilations with 30-min windows were performed, from 2000 to 2030 JST and from 2030 to 2100 JST. In these windows, owing to computational restrictions, about 50 iterations for minimization were performed. A 1-h free forecast was conducted from 2030 to 2130 JST, using the NHM-4DVAR analysis at 2030 JST provided by the second window as the initial conditions over the same domain with the analysis. In fact, in this configuration, the pure forecast, unconstrained by observation data, is 30-min long. Figure 4.5 presents a schematic chart of this assimilation experiment.

Additional data-denial experiments were conducted to investigate the impact of the observation data. Hereafter, "ref" means the experiment with radar reflectivity, "wo-ref" means that without reflectivity, and "ctl" means the experiment with the first-guess field.

4.5 Results

4.5.1 Examination of QPF

Time series of the threat scores of the reflectivity field on a 0.7° elevation plane are shown in Fig. 4.6. In the ctl case, the scores for both the 15 and 30 dBZ thresholds were very low, below 0.1, at every forecast time. In the wo-ref case, the 15 dBZ score was high, above 0.25, at the first 15 min, but low, below 0.2, at forecast time after 15 min. The 30 dBZ score was low at the forecast start time, but became relatively high, about 0.2, by the forecast end time. In the ref case, the 15 dBZ score was very high, over 0.6, at the forecast start time, but became relatively low, about 0.3, by the forecast end time. The 30 dBZ score was also notably high, about 0.5, during the first 30 min, but became
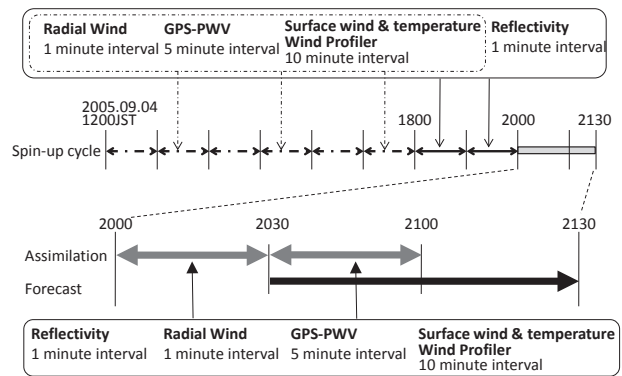
low, about 0.25, by the forecast end time. These results indicate that the assimilation of indirect observations (e.g., GPS-PWV, RW and surface observations) can modify the reflectivity field, and that these observations substantially affect weak convection, but they do not affect strong convection to a large extent. Further, the direct assimilation of reflectivity can substantially modify the forecast of strong convection, especially at early forecast times.

4.5.2 Reflectivity

The distribution of reflectivity observed by the Haneda airport radar and the corresponding simulated reflectivity from the ref, wo-ref, and ctl experiments are shown in Fig. 4.7. The ctl experiment could not simulate the line-shaped rainband, convective cells are only sparsely distributed along the foot of the mountainous region west of the Kanto plain (Fig. 4.7d). In wo-ref (Fig. 4.7c), L1 is reproduced, though with less intensity than the observation. This result was mainly attained by the assimilation of GPS-PWV, RW, and the wind profiler data. Surface observations include information about surface-wind circulation, but in this case their impact on the reproduction of L1 was small. In the experiment, weak convective cells, not found in the observation, also developed around Tokyo bay.

The wo-ref reflectivity field at 2030 JST seems noisy in (Fig. 4.7c), possibly because NHM-4DVAR adopts a control variable related to rain water. Since there was no rain water observation in wo-ref, the minimizer cannot determine the optimal direction of the rain-water state.

In ref (Fig. 4.7b), L1 is well reproduced, with a shape and intensity consistent with the observation (Fig. 4.7a). At 2130 JST, false convective cells appear over Tokyo bay, but their intensity is weak. Compared with wo-ref, assimilation of the reflectivity intensified L1 and assimilation of 0
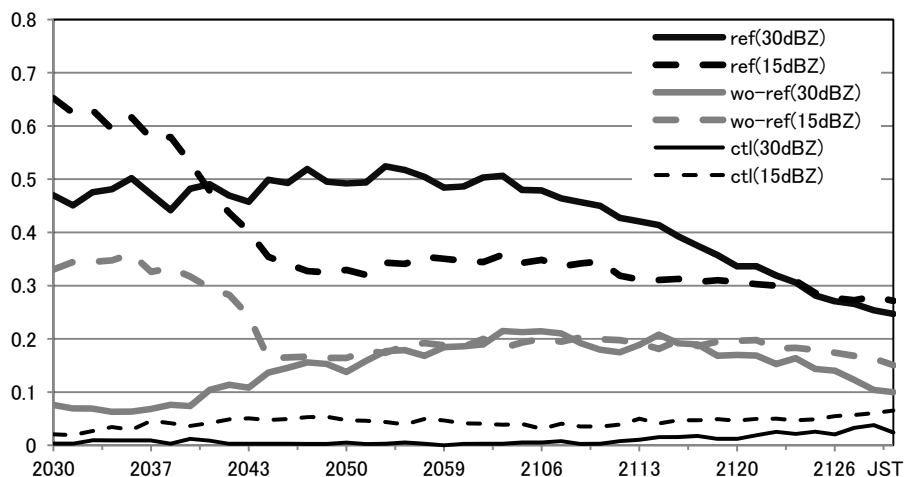
Fig. 4.6. Time series of threat score of reflectivity field on 0.7° elevation plane. Solid lines show the scores of threshold of 30 dBZ and dash lines are threshold of 15 dBZ. Black lines indicate the results of ref, gray lines indicate that of wo-ref, and thin black lines indicate that of ctl.

dBZ (see Section 4.5.4) suppressed the false convection.

Vertical cross-sections of the differences between ref and wo-ref are presented in Fig. 4.8. In the ref experiment, the convective updraft was intensified around L1, and water vapor and potential temperature also increased beneath L1. Thus, the dynamical and thermodynamical fields were modified by the assimilation of observed radar reflectivity, such that the circumstances became suitable for intensification of the rainband.

4.5.3 Evolution of the rainband

In this section, we compare the evolution of L1 as simulated in the ref experiment with the observation.

At 2030 JST, the start time of the assimilation window, the three convection, L1, L2, and L3, recognized in the observation (Fig. 4.7a) are roughly reproduced in the ref experiment (Fig. 4.7b). Areas of weak reflectivity are more widespread in ref, however, than in the observation. Rain water in these areas is produced by horizontal correlation of the background errors. Since these are neither dynamically nor thermodynamically related to the environmental fields, they soon evaporate and vanish.

At 2050 JST, L1 is well reproduced in the ref experiment in terms of intensity, size, and location. L2 has shifted northwestward, and L3 and other precipitation areas have disappeared. Around this time, the observed L1 becomes enhanced (Fig. 4.7a), and a similar tendency is reproduced in the experiment.

At 2111 JST, L1 has moved northward while maintaining its intensity. Convection in the ref experiment is slightly more intense than the observed convection. In the experiment, a few false convective cells appear over Tokyo Bay, but they are weak.

At 2130 JST, L1 remains in the same region because new convection is generated at its southern tip, although each convective cell in L1 has moved northward. L1 thus seems to have a back-building formation mechanism. The intensity of L1 in ref is similar to the observation, but in ref, L1 is entering a decaying stage. After 2130 JST, the intensity and shape of L1 could not be maintained in the extended forecast.

The horizontal distributions of the mixing ratio of q_r and the winds at $z^* = 225$ m in ref are shown in Fig. 4.9, vertical cross sections of the mixing ratio of q_r, winds, and the equivalent potential temperature of ref below 5 km along line A-B (see Fig. 4.9d) are shown in Fig. 4.10. From 2050 to 2110 JST, easterly winds blowing toward L1 are seen in the eastern part of L1 in the assimilation window, and northerly winds west of L1 weaken. As a result, the low-level convergence around L1 decreases, ultimately vanishing at 2130 JST (Fig. 4.9d). However, the distribution of equivalent potential temperature does not change during this period. Thus, the decay of L1 is caused by a change

69
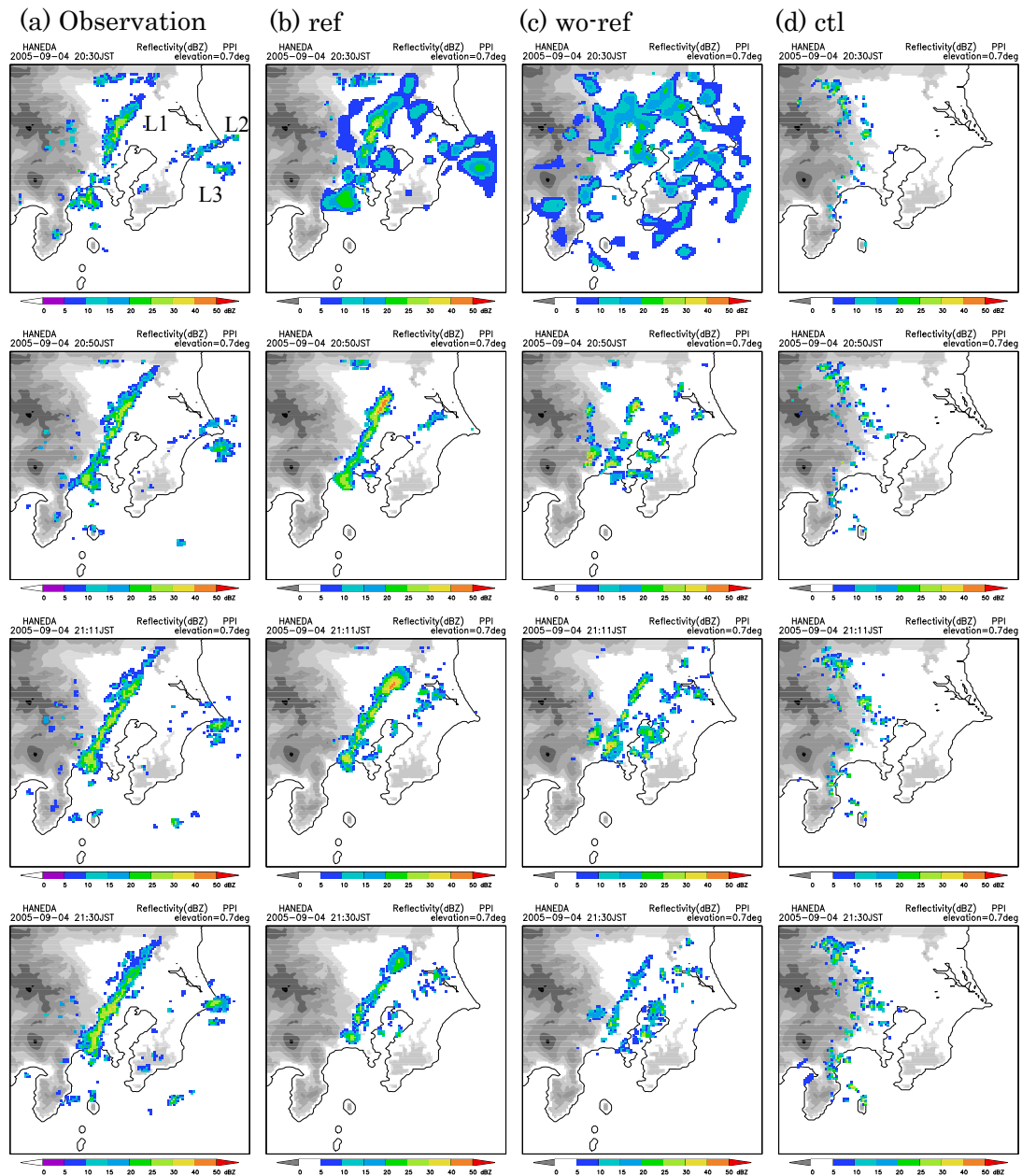
Fig. 4.7. Radar reflectivity on 0.7° elevation plane from 2030 to 2130 JST. (a) Observation from the Haneda airport radar. (b) Assimilation and forecast results with radar reflectivity. (c) Same as in (b) but without the assimilation of reflectivity. (d) First guess field. Black shows orography.

70
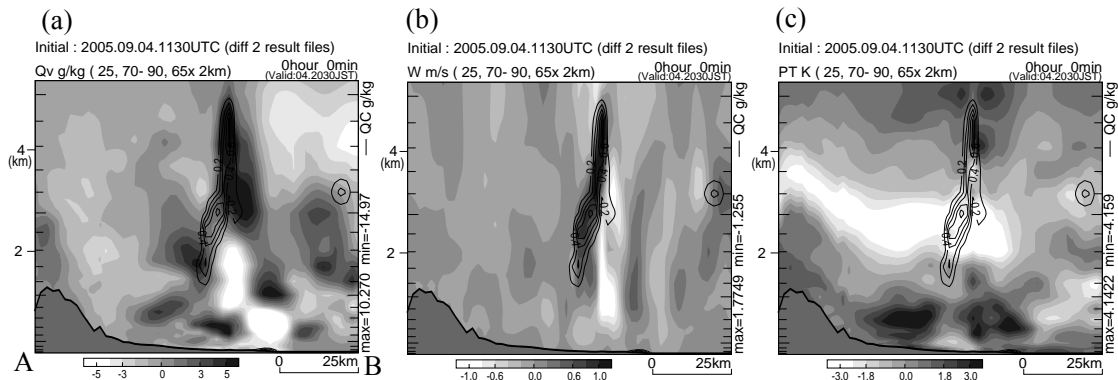
Fig. 4.8. Vertical cross sections of differences between ref and wo-ref experiments at 2030 JST along the line A-B in Fig. 4.9. Shades show differences of mixing ratio of water vapor (q_v) in (a), vertical wind (w) in (b), and potential temperature in (c). Contours show mixing ratio of cloud water (q_c) in the ref experiment.
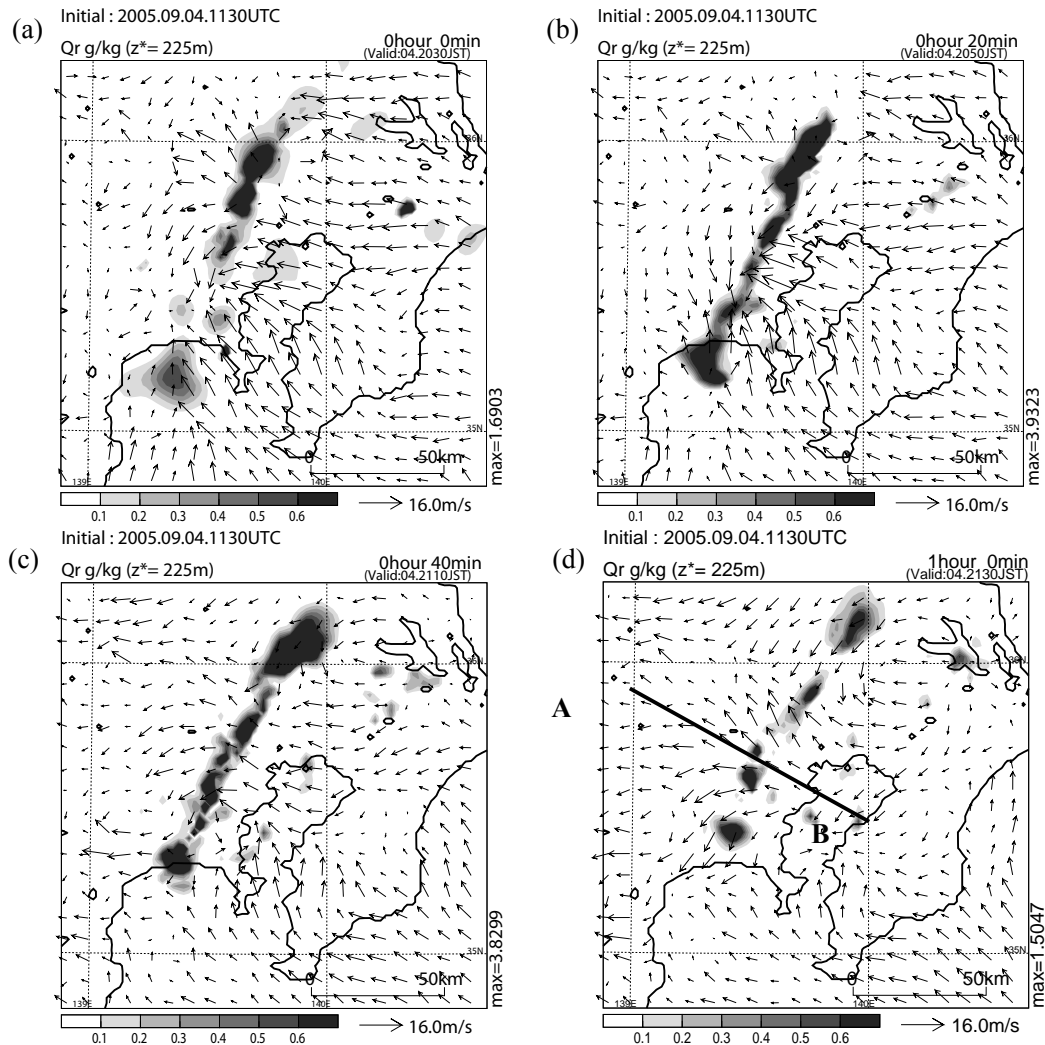
Fig. 4.9. Horizontal distribution of mixing ratio of q_r (shades) and winds (vectors) at z* = 225 m of ref. The line A-B denotes the vertical cross section in Fig. 4.8.
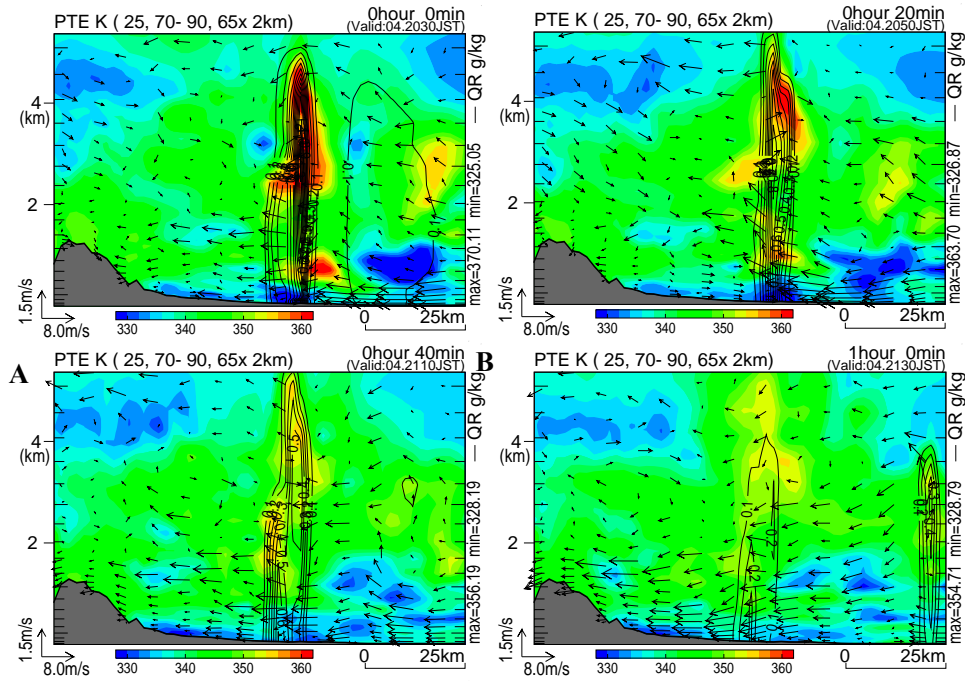
Fig. 4.10. Vertical cross sections of mixing ratio of q_r (contours), winds (vectors) and equivalent potential temperature (shades) in ref along the line A-B in Fig. 4.9.

in the dynamical rather than the thermodynamical environment. Hence, we infer that a northerly wind would have to be reproduced to maintain the low-level convergence, and the rainband, after Regarding the thermodynamical field, a warm, wet easterly inflow with an equivalent potential temperature of more than 350 K can be recognized in the lower part of the rainband (at about $z^* = 1$ km) at 2030 JST (Fig. 4.10, upper left). A small cold pool with an equivalent potential temperature of less than 336 K exists at the surface to the west of the rainband. This cold pool contributes to the maintenance of the rainband. At 2050 JST (Fig. 4.10, upper right), a strong updraft and associated heating are identified in the rainband between 0.5 and 3 km. This inflow and the updraft are important for the rainband maintenance, but they are not sufficient to sustain it for a long time. The updraft weakens after 2110 JST (Fig. 4.10, lower).

4.5.4 Assimilation of 0-dBZ information

In this study, we regarded only reflectivity values greater than 10 dBZ as proper observations. Initially, we neglected weak reflectivity of less than 10 dBZ in order to avoid inappropriate reflectivity caused by materials other than rain water. However, as discussed in Section 2.3.4, such very weak reflectivity data convey the information that rain water is absent or that the amount is very small in the observed area.

To incorporate this information, we assimilated weak reflectivity of less than 10 dBZ as an observation of 0 dBZ. The observational error was set to 30 dBZ for this observation (three times the

normal error) because 0 dBZ is not genuine observational data. In addition, we assimilated 0 dBZ only in regions where the reflectivity in the first-guess field exceeded 10 dBZ.

The impact test results are presented in Fig. 4.11. Reflectivity observed by the Haneda airport radar is presented in Fig. 4.11a, and the first-guess field, the assimilation result of ref with 0 dBZ, and the result without 0 dBZ are illustrated in Figs. 4.11b-d), respectively.

There is a false convective area on the east side of Tokyo bay in the first-guess field (circled in Fig. 4.11b) but not in the observation (Fig. 4.11a). After the assimilation of reflectivity, the reproduction of L1 is improved (Figs. 4.11c and d), but the false cells are still seen in the assimilation result without 0 dBZ. It is clear that the assimilation of 0 dBZ suppressed the false convection. This sup-
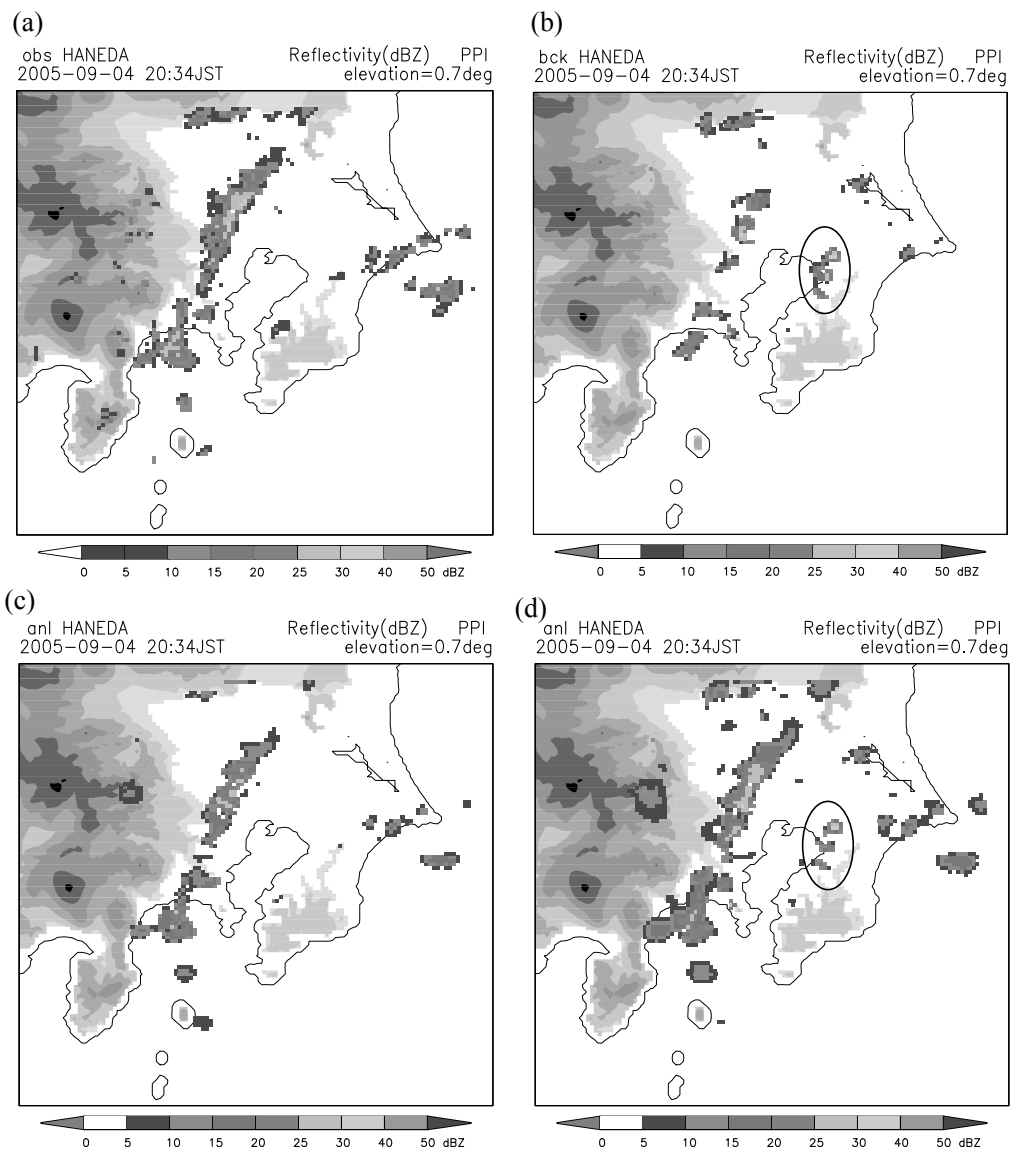
Fig. 4.11. Impact tests of the assimilation of 0 dBZ. (a) Observed reflectivity from the Haneda airport radar. (b) Simulated reflectivity from the background field. (c) Same as in (b) but by the assimilation result with 0 dBZ. (d) Result without 0 dBZ.

73

pression is similar to the case 2 result described in Section 2.3.4.

The area of 0 dBZ is very much wider than other areas, and the cost function tends to be minimized in a direction without convection. Therefore, use of 0 dBZ should be limited, as pointed out by Koizumi et al. (2005).

4.6 Discussion

4.6.1 Sustaining low-level convergence

As described in Section 4.5, the line-shaped rainband L1 is reproduced in the assimilation and in the corresponding extended forecast. Horizontal wind convergence along the reproduced rainband was seen below a height of 2000 m. However, this convergence weakened at 2110 JST and vanished after 2140 JST. This convergence appears to have maintained the rainband.

Figure 4.12 illustrates the differences in horizontal wind and the mixing ratio of rain water between ref and wo-ref at 225 m height at the end time of the first assimilation window. The mixing ratio of rain water in the main rainband L1 increases, and the easterly wind is strengthened in the east of L1. The southerly wind is also strengthened in the inflow region of the rainband. This change in the wind field is caused by the assimilation of reflectivity. Therefore, it is clear that the assimilation of reflectivity changes the low-level wind circulation and contributes to producing the line-shaped rainband.

However, the northerly winds in west of L1 did not continue for a long time, and L1 began to weaken after 2110 JST. This problem was likely caused by insufficient retrieval of the thermodynamical field, as mentioned in Section 4.5.4. To improve this situation, more observations [e.g., wind profiler, radio-sonde, and Aircraft Communications Addressing and Reporting System (ACARS)] are needed in these areas.

To extend the influence of the assimilation of reflectivity and RW, it seems necessary to lengthen the assimilation windows, but because of the strong nonlinearity we could not make them longer than 30 min. A test case with a 1-hr assimilation window did not reproduce the intensity of L1 even
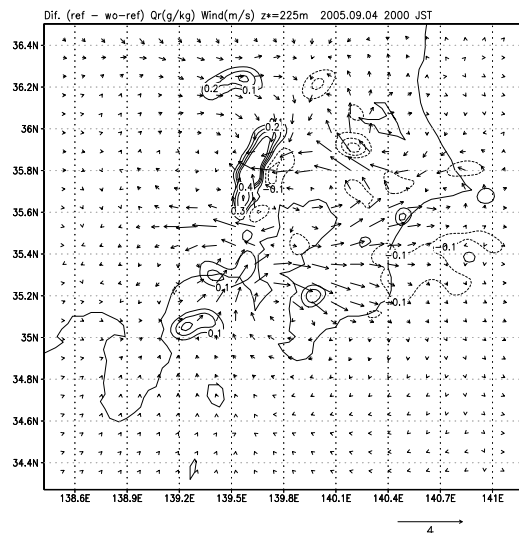
Fig. 4.12. Differences of horizontal winds (vectors) and mixing ratio of q_r (contours) between ref and wo-ref at 225 m height at the end time of the 1st assimilation window.
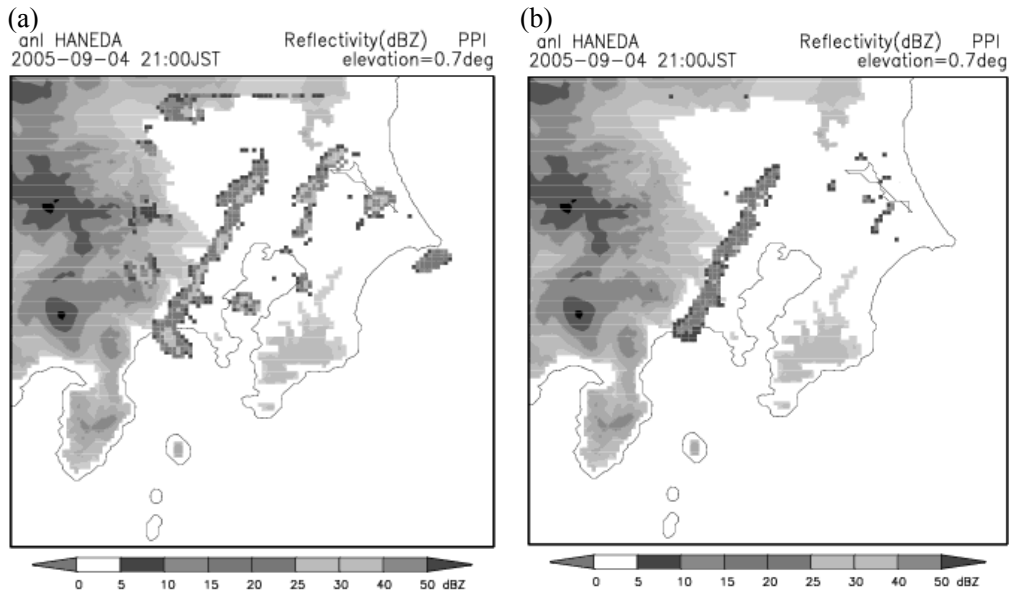
Fig. 4.13. Radar reflectivity field on 0.7°-elevation plane from (a) the original system, and (b) the incremental method.

in the assimilation window (not shown).

4.6.2 Incremental method with a tangent linear model

As described in Section 2.3.1, there is an inconsistency between the forward and adjoint models in NHM-4DVAR. Since this inconsistency caused problems, as described in Section 2.3.1, we attempted to use an incremental method (Courtier et al. 1994), which uses tangent linear and adjoint models in an inner loop and the nonlinear model in an outer loop. In this system, the outer loop trajectory is updated every 10 inner loop iterations. An advantage of this method is that the convergence of the minimization process is improved by the consistency between the forward and adjoint models, and the nonlinearity is taken into consideration by the frequent updating of the outer loop trajectory.

An experiment with 10-min windows was carried out. Figure 4.13 compares the reflectivity fields obtained using the incremental system and the original system. Reflectivity of more than 25 dBZ can be recognized widely in the reproduced rainband in the original system, whereas, reflectivity is less than 25 dBZ in the incremental system. The incremental system using the simplified tangent linear model thus could not reproduce the strong
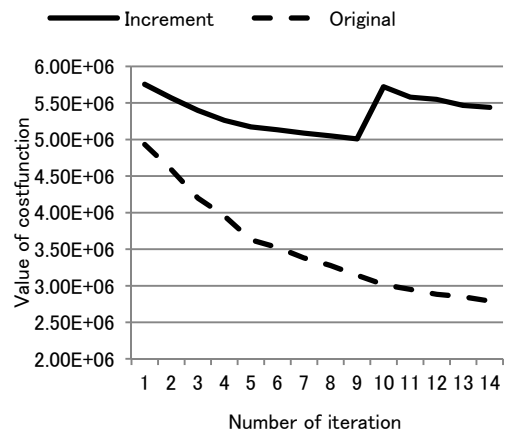
Fig. 4.14. The value of cost function J of the original and the incremental system.

75

rainband. A possible reason for this failure is that the strong nonlinearity of the mesoscale convective rainband cannot be reproduced by the tangent linear system. Figure 4.14 shows the time sequence of cost function J in the two systems. The cost function obtained by the incremental system is sluggish during the iteration process and shows a jump when the outer loop trajectory is updated. Most of this jump is in the observation term, because that term is recalculated with a new trajectory after the updating. Given these results, we did not adopt the incremental system in our study.

4.7 Summary

An assimilation experiment with a horizontal resolution of 2 km based on actual observations of a local heavy rainfall in the Tokyo metropolitan area was conducted. Precipitable water vapor derived from GPS data were assimilated at 5-min intervals during 30-min assimilation windows, and surface data and wind profiler data were assimilated at 10-min intervals. The Doppler radial wind and radar reflectivity were assimilated at 1-min intervals for elevation angles of less than 5.4°.

A line-shaped rainband was well reproduced by the assimilation of reflectivity, with a shape and intensity consistent with the observation. Compared with the wo-ref experiment, the ref experiment intensified an originally weak rainband and suppressed false convection. False convection was controlled by assimilating 0 dBZ, and the results were consistent with the results of the single-observation assimilation experiments.

In the extended forecast, the simulated line-shaped rainband gradually decayed after 1-h. Sustaining the low-level convergence produced by northerly winds in the western part of the rainband seems to be key to maintaining the convective system. RW and reflectivity data can be obtained only in areas where rain water actually exists.

The environmental field should be further modified to enhance the predictability of the observed convective system. This problem corresponds to the inverse problem, in which the environmental field is estimated from the observations. Since this relationship is nonlinear, solving the problem is not easy.

To predict rainbands, it is important to estimate their environmental field. However, we have not carried out sufficient observations outside the rainband, although we have carried out many observations within the rainband. Therefore, we have to estimate the environmental field (thermodynamical and dynamical fields) from the observation data from within the rainband. Reflectivity indicates the existence of rain drops, but information on raindrops in clouds cannot be connected to environmental thermodynamical and dynamical fields directly, because the relationship is not linear. Hence, it is difficult to solve the inverse problem. However, it can be easier to estimate the raindrops from the information on the environmental fields because the information is the source of the raindrops. Thus, more information on environmental fields is needed to improve short-range fore-

casts of local heavy rain events. To enhance the predictability of heavy rainfall, it will be necessary to develop techniques to overcome the nonlinearity. In addition, the introduction of a flow-dependent background error and the consideration of model error are future subjects for study.

Chapter 5

Assimilation Experiment using NHM-4DVAR v2

with GPS Slant Total Delay Data

- Naha Heavy Rainfall Event on 19 August 2009 -

This chapter shows a case study on Naha heavy rainfall event occurred around Okinawa Island on 19 August 2009 with the assimilation method of GPS slant total delay data (See Section 2.4.4) as the first application to a cloud-resolving scale. Moreover, an initiation mechanism of the line-shaped rainband appeared around Okinawa Island is discussed. First, a high-resolution numerical experiment using JMA-NHM with 2-km horizontal grid spacing (NODA) is conducted. Then data assimilation experiments with GPS observations (i.e., GPS zenith total delay (GPS-ZTD), GPS precipitable water vapor (GPS-PWV), and GPS slant total delay (GPS-STD)) at the same resolution are performed. Generally, compared with NODA, the assimilations of GPS-ZTD and GPS-PWV are known to slightly improve the timing of the rainband initiation. On the other hand, the GPS-STD assimilation significantly improves the forecast skill of the water vapor and temperature fields over a wide area as well as the time of the occurrence for the rainfall event. This result shows that assimilating environmental information has capability to improve the predictability of MCSs.

5.1 Introduction

The growth of cities has increased vulnerability to natural disasters. For example, flooding of small rivers within some Japanese cities caused by rapidly developing thunderstorms has become a societal problem. One such urban disaster occurred on Okinawa Island, Japan, on 19 August 2009, when flash flooding induced by a small convective system claimed the lives of four workers assessing the seismic capacity of a bridge. This thunderstorm was difficult to predict due to its small horizontal scale (2 to 4km), although the rainband in which the thunderstorm was embedded was predictable by

advanced numerical prediction systems. Stationary MCSs consisting of several cumulonimbus cloud systems are frequently observed over Okinawa in summer. These MCSs often form a line-shaped rainband, and they develop even in the absence of strong synoptic forcing by a typhoon or a Baiu front.

Such rainbands are likely affected by the orography of the island. For example, Chang and Yoshizaki (1991) simulated an MCS observed over Okinawa with a two-dimensional numerical model and concluded that the initiation and movement of the MCS were forced by interactions between the mountains on the island and a cold pool created by the MCS. Minda et al. (2010) also investigated the initiation process of MCSs over Okinawa by using Doppler radar observations and numerical simulations with a 250-m grid spacing. They conducted impact tests with and without incorporating mountain effects and reported that similar MCSs were reproduced in both simulations, but the sea breeze circulation was somewhat stronger when the mountain effects were included. Mikami et al. (2011) investigated the evolution of a small convective system over Okinawa by conducting a 1-km numerical simulation with wind profiler and radio acoustic sounding system (RASS) observations. They reported that the convective system developed when the sea breeze circulation reduced the vertical atmospheric stability.

Although these various numerical simulations reproduced their target phenomena (MCS or convective system), Chang and Yoshizaki (1991) used a two-dimensional model, whereas Minda et al. (2010) and Mikami et al. (2011) used high-performance numerical models but downscaled (so-called 'cold start') initial conditions in their studies. From the viewpoint of weather forecasting, forecasting the timing and location of an MCS or convective system is particularly important. However, these previous studies did not address timing and location; rather, they were primarily concerned with MCS characteristics or structures. To improve timing and location forecasts, high-performance models that incorporate detailed physical processes (i.e., cloud microphysics and surface processes) and have high horizontal resolution should be used, and observational data should be assimilated to modify the initial water vapor and thermodynamics fields. Therefore, in this study, we used a three-dimensional high-performance model with high horizontal resolution that included cloud microphysics and used an advanced 4D-Var data assimilation system.

To investigate how forecasts of the timing and location of an MCS might be improved, we performed three sets of numerical experiments. First, we examined the effect of the topography of Okinawa Island on the rainfall distribution and timing predicted by JMA-NHM with a 5-km horizontal grid spacing. In general, numerical models with a 5-km grid spacing can reproduce rainfall distributions of MCSs rather well, but their performance in forecasting rainfall intensity and timing is poor. The rainfall intensity forecast can be improved by increasing the horizontal resolution and by considering cloud microphysics. Therefore, we next carried out experiments using a model with a 2-km horizontal resolution and cloud microphysics. To further improve rainfall forecasts, the initial condi-

tions should be improved by using an advanced data assimilation system to assimilate observations with high horizontal and temporal resolution. Therefore, we developed a data assimilation method for GPS-STD observations and used NHM-4DVAR to conduct GPS-STD data assimilation experiments.

GPS-STD is the atmospheric delay of radio waves traveling from a GPS satellite to a ground-based receiver; GPS zenith total delay (GPS-ZTD) is the atmospheric delay directly above the receiver; and GPS precipitable water vapor (GPS-PWV) is the cumulative value of precipitable water vapor observations directly above a receiver. The advantage of GPS-STD is that it includes information about several atmospheric parameters (pressure, temperature, and humidity) in several directions from each receiver. Therefore, the assimilation of GPS-STD data improves the water vapor field with thermodynamics field of the model above and around observation points. The Geospatial Information Authority of Japan has deployed about 1200 GPS receivers throughout Japan that are operated year-round. JMA began to use high-density GPS-PWV observations in its operational mesoscale data assimilation system in 2009. In this study, we used GPS-STD observations obtained by the same observation network.

Ha et al. (2003) carried out an Observation System Simulation Experiment (OSSE) using GPS slant water vapor observations, which are accumulated along slant paths from GPS satellites to receivers (GPS-SW), derived from a virtual GPS observation network. The advantage of GPS-SW data compared with GPS-PWV observations is that information is obtained in various directions from each receiver. Using a fifth-generation mesoscale model (MM5)-4DVar system (Zou and Kuo 1996) with a 27-km horizontal grid spacing to assimilate GPS-SW observations, Ha et al. (2003) obtained good squall-line simulation results. Järvinen et al. (2007) used a High Resolution Local Area Modelling-3D-Var system (HIRLAM; Gustafsson et al. 2001) with a 9-km horizontal grid spacing for GPS-STD assimilation, and demonstrated that the magnitude of the GPS-STD assimilation analysis increments exceeded that of the GPS-ZTD assimilation analysis increments, and that the horizontal distribution of analysis increments differed between the GPS-STD and GPS-ZTD assimilations. Bauer et al. (2011) examined the impact of GPS-STD assimilation on quantitative precipitation forecasting (QPF) with the MM5-4DVar system and found that the GPS-STD assimilation improved QPF scores. They used two types of initial fields for 24-h forecasts, a downscaled initial field based on operational forecasts of the European Centre for Medium-Range Weather Forecasts (ECMWF), and a modified initial field derived from GPS-STD assimilation. Although they were able to demonstrate the advantages of GPS-STD assimilation on the basis of the QPF scores over a one-month period, the horizontal grid spacing of their assimilation system was 18 km. To the best of our knowledge, 4D-Var assimilation of GPS-STD data at storm scale has yet to be performed.

GPS-STD observations include both vertical and horizontal information about the atmosphere, whereas GPS-ZTD and GPS-PWV observations include only vertical information. Thus, in assimila-

tions of GPS-STD observations it is important to take advantage of the horizontal information. For instance, the point at which a slanted path with a 30° elevation angle crosses the troposphere is 17 km (horizontal distance) from the GPS receiver. Thus, if the assimilation system has a 20-km horizontal grid spacing, the GPS-STD data cover only two model grid cells. As a result, the expected assimilation effect would be similar to the GPS-ZTD assimilation effect. The NHM-4DVAR system used in this study has a 2-km horizontal grid spacing. Thus, we expected that our numerical simulations would demonstrate more distinct impacts of GPS-STD assimilation than was possible with the lower resolution systems.

In this case study, we introduce the target rainband in Section 5.2 and already describe the NHM-4D-VAR and the GPS-STD assimilation method in Chapter 2. In Section 5.3, we present downscaled forecasts and results, and we discuss the assimilation results in Section 5.4. Section 5.5 is a summary with concluding remarks.

5.2 Overview of the event

Okinawa is a subtropical island located between the four main Japanese islands and Taiwan (Fig. 5.1). It is 3 to 30 km wide and 110 km long, extending from southwest to northeast. The northern half of the island is characterized by mountains with elevations of more than 200 m above sea level, whereas the southern half is relatively flat and stands at elevations of less than several tens of meters.

The surface weather map for 0900 JST (Japan Standard Time: UTC + 9 h) on 19 August 2009 (Fig. 5.1) shows a high-pressure system over the Japanese islands and a weak low-pressure area south of the islands. No strong synoptic forcing, such as a typhoon or a Baiu front, is visible around Okinawa. The surface wind on this date was dominantly northeasterly; thus, the prevailing wind was blowing parallel to the long axis of Okinawa Island. The wind speeds measured on Okinawa at 0600 JST on 19 August were 3 to 5 m s^{-1}, and the surface temperatures were 26 to 27°C. By 1200 JST, the wind speeds and the surface temperatures had increased to 4 to 7 m s^{-1} and to 29 to 33°C, respectively.

Sporadic convective clouds over Okinawa began to form a line-shaped MCS, aligned along August 2009 (Fig. 5.2). This MCS intensified until 1400 to 1500 JST and then vanished at around 1530 JST. The horizontal distribution of the 1-h accumulated rainfall amounts observed by the JMA
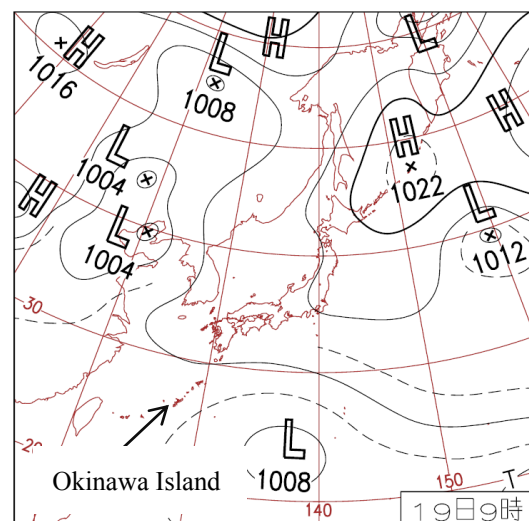
Fig. 5.1. Surface weather map at 0900 JST on 19 August 2009.
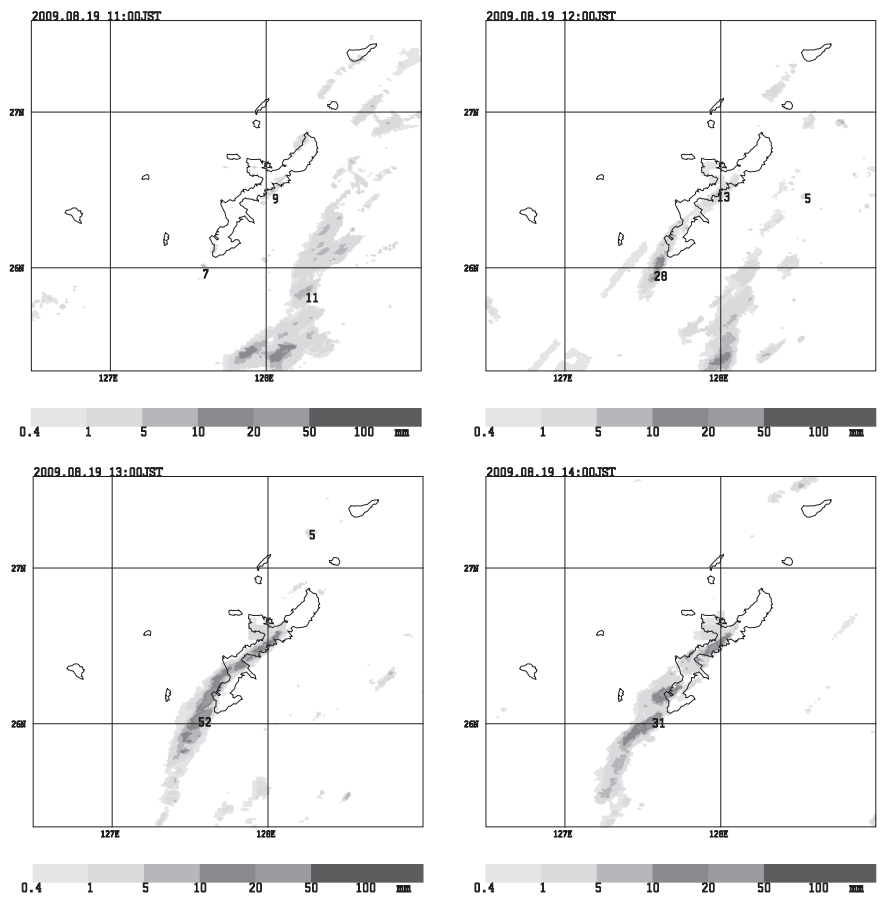
Fig. 5.2. Horizontal distributions of 1-h accumulated rainfall amounts from 1100 to 1400 JST on 19 August 2009.

operational radars and calibrated by the JMA surface rain gauge observations (Fig. 5.2) shows that the MCS was 200 km long and 30 km wide. The maximum rainfall intensity, observed at 1400 JST, was 52 mm h^{-1}.

The accident referred to in the introduction (Section 5.1) occurred on the Ga-bu River, 5 km east-northeast from Naha Airport (indicated by the cross in Fig. 5.3). The total rainfall amount recorded at Naha airport between 1210 and 1400 JST (Fig. 5.4) was 58.5 mm, and the maximum rainfall intensity was 13.5 mm per 10 minutes. The locally heavy rainfall around the Ga-bu River (Fig. 5.3) that led to the loss of human life was caused by this convective system. Near the headwaters of the Ga-bu River, the rainfall intensity reached 32 mm h^{-1} and caused freshet in the Ga-bu River, which flows between concrete walls, and the flood carried away four workers who were investigating the seismic capacity of a bridge. Similar disasters can occur along the many rivers located near cities in Japan, but because of the smallness of the temporal and spatial scales of such mesoscale events, predicting the development of similar convective systems by current numerical weather prediction systems is quite difficult.

83
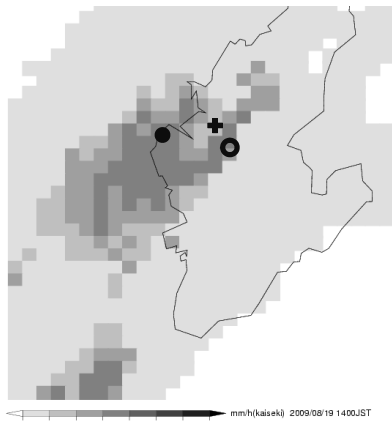
Fig. 5.3. Horizontal distribution of 1-h accumulated rainfall amounts around the Ga-bu River at 1400 JST. Size of each box is 1 km x 1 km. The cross mark indicates the accident point (on the Ga-bu River), and the open circle indicates the headwaters of the Ga-bu River. The solid black circle indicates Naha airport. The coastline of Okinawa Island is also shown.
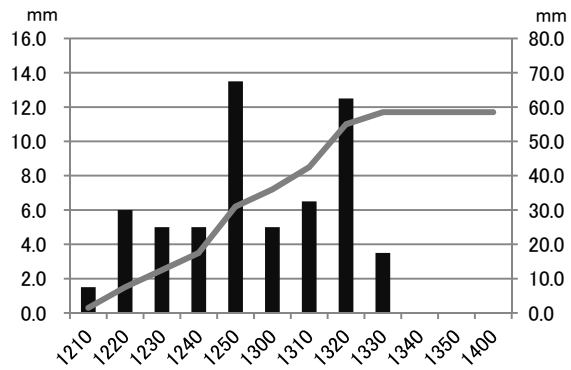
Fig. 5.4. Time series of 10-min rainfall amounts (bars; left axis) and accumulated amount (line; right axis) at Naha airport, shown as a solid black circle in Fig. 5.3.

5.3 Numerical experiments with downscaled initial conditions

5.3.1 Experimental design

To investigate the factors responsible for the rainband initiation over Okinawa, we performed three numerical simulations: (a) a control experiment using the actual orography and land-surface conditions (CTL), (b) a simulation in which all islands were treated as sea (Sea), and (c) a simulation in which all mountains were flattened and the roughness of the land surface was set to the same value as that of the sea (NoMt). The most important difference between Sea and NoMt is land-heating on the islands.

Initiation of a rainband on small islands is expected to be caused mainly by (i) uplift in mountainous regions, and (ii) land-sea wind circulation due to contrasting sea and land surface temperatures. In addition, (iii) frictional convergence caused by a difference in wind speed between the sea and land may affect rainband initiation. The NoMt experiment represents that updrafts due to uplift along mountain slopes and frictional convergence were eliminated as a cause. The difference in the simulation result between CTL and NoMt mainly represents the mountainous orography effect (i) and the difference between NoMt and Sea represents the surface heating and friction effect (ii and iii). In all three simulations, initial conditions were provided by the JMA mesoscale analysis at 2100 JST on 18 August 2009, and boundary conditions were given by the JMA global model forecasts until 1500 JST on 19 August. The horizontal resolution was 5 km. The JMA-NHM settings, including the Kain-Fritsch convective parameterization, were the same as those of the JMA operational

mesoscale model.

5.3.2 Results of the downscaled experiments

In CTL (Fig. 5.5a), convective systems developed over northern Okinawa Island at 1200 JST. By 1400 JST, they had organized into a rainband, similar to the observed one. In Sea (Fig. 5.5b), several convective systems persisted over the ocean for more than 3 h, but they did not organize into a rainband. The convective area in the northern part of the experimental domain had vanished by 1300 JST. In NoMt (Fig. 5.5c), the distribution and intensity of precipitation were similar to those in CTL. Surface temperatures over southern Okinawa in both CTL and NoMt reached 306 K, close to the observed value, whereas the surface temperature in Sea was fixed at 301 K, the sea surface
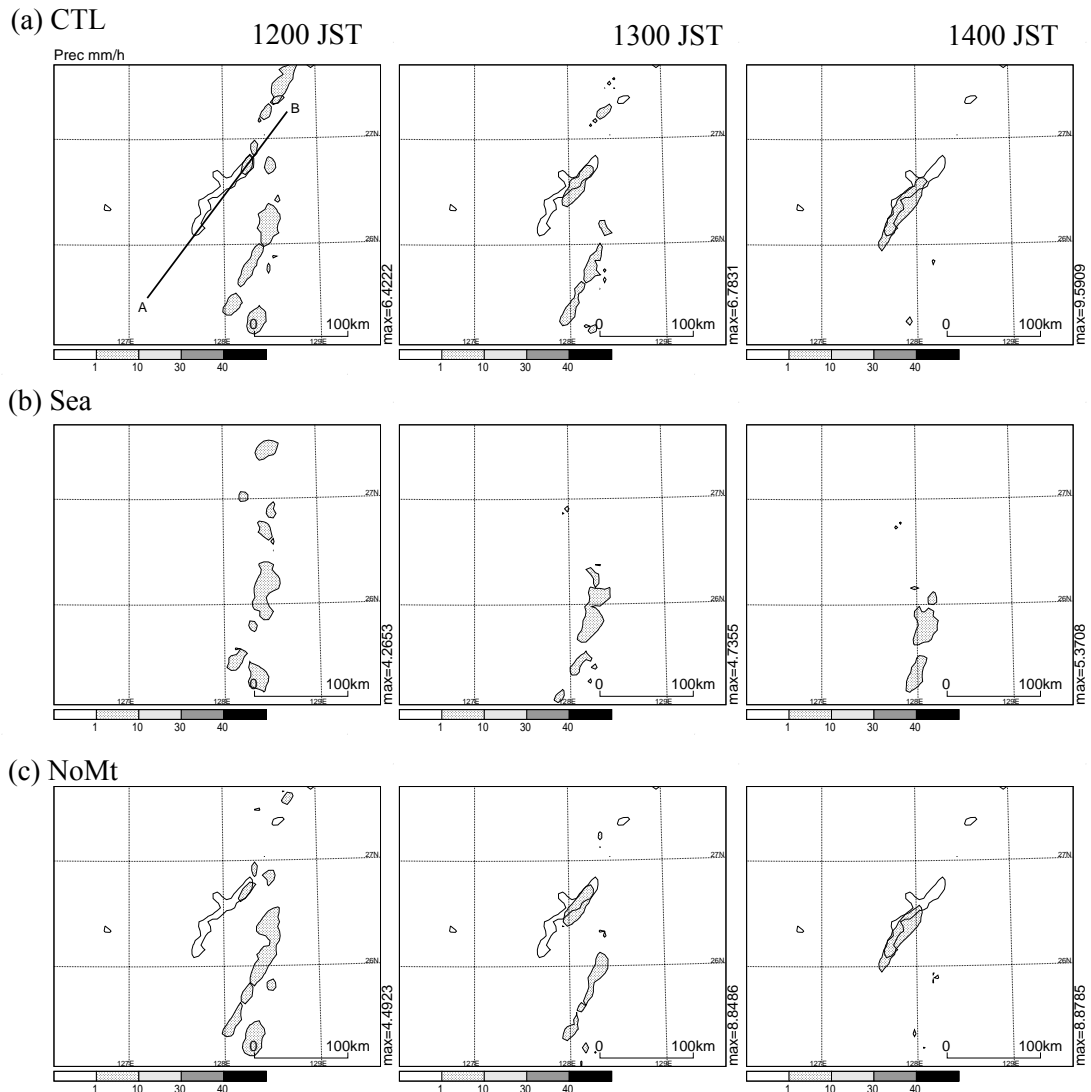
Fig. 5.5. 1-h rainfall intensity (mm h^{-1}) of CTL (a), Sea (b), and NoMt (c) from 1200 to 1400 JST on 19 August.

(a)

(b)

(c)
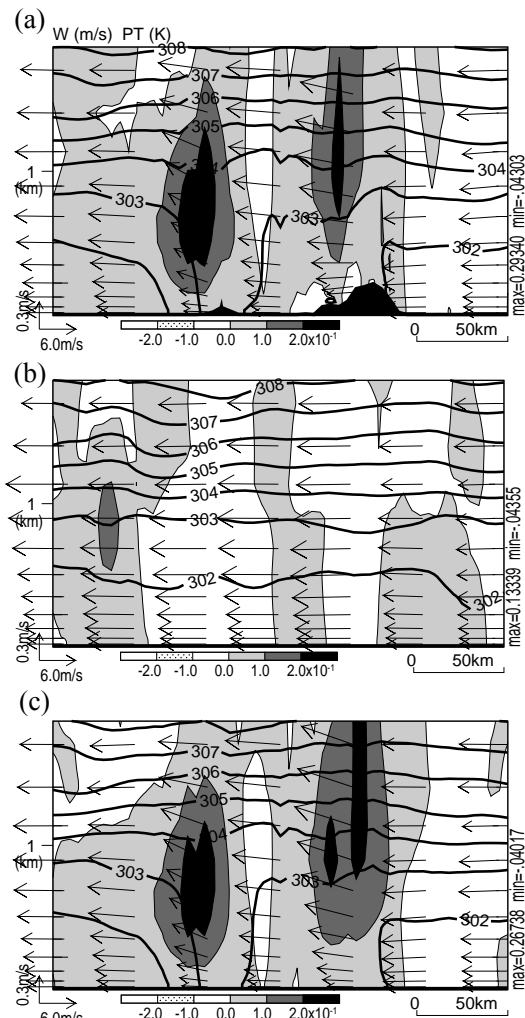
Fig. 5.6. Vertical cross sections along line A–B in Fig. 5.5a of potential temperature (contours), vertical wind speed (shades), and wind projected on the cross section (vectors). CTL (a), Sea (b), and NoMt (c) at 1200 JST.

Fig. 5.7. Horizontal distribution of the lifted condensation level (LCL) at z* = 128 m at 1200 JST in CTL.

temperature. From these results, it is reasonable to infer that surface heating was the key to the production of the rainband, whereas orographic effects and wind convergence due to surface roughness were not critical in initiating the rainband.

Examination of the results in vertical cross section along Okinawa's long axis showed that the boundary layer evolved to a height of 1 km over Okinawa in both CTL and NoMt (Figs. 5.6a, c), whereas in Sea (Fig. 5.6b), temperature was horizontally homogeneous, and no boundary layer was apparent. The similarity between CTL and NoMt indicates that the mountains in northern Okinawa did not play an important role in the evolution of the boundary layer over the island.

Two major updrafts of more than 0.2 m s^{-1} were simulated in CTL and NoMt, one to windward and the other to leeward over the island, where the top of the boundary layer was higher than it was over the sea. In addition, the wind in the lowest atmospheric layer over the central part of the island was clearly weaker in the CTL and NoMt results than in the Sea result. In NoMt, the roughness of the island land surface was the same as the sea surface roughness, so this weakening was not induced by surface friction. The wind distributions instead suggest the occurrence of land–sea circulation in the boundary layer in CTL and NoMt. Therefore, we inferred that the updrafts simulated in these

experiments led to the development of the convective system over the island.

In both CTL and NoMt (Fig. 5.6a and c), only the updraft over northern Okinawa induced a convective system, because vertical stability was greater over southern than over northern Okinawa (Fig. 5.7). In the north, the height of the lifted condensation level (LCL) was 500 to 600 m, whereas in the south it exceeded 900 m. The relatively stable atmospheric condition in the south depressed the development of convection.

At 1400 JST, the rainbands in CTL (Fig. 5.5a) and NoMt (Fig. 5.5c) appeared to be similar to the observed rainband (Fig. 5.2). These results indicate that the land–sea circulation caused by surface heating of the land initiated rainband development at the same location that the observed rainband was initiated. However, the timing of rainband initiation in CTL and NoMt was delayed compared with the observation. Moreover, the maximum observed rainfall intensity at 1300 JST was 52 mm h^{-1} and that at 1400 JST was 31 mm h^{-1}, whereas in CTL, they were 7 and 10 mm h^{-1}, respectively. In general, a high-resolution simulation with cloud microphysics can enhance the rainfall intensity forecast. The comparison of the vertical cross sections of CTL, NoMt, and Sea results suggests, however, that atmospheric instability greatly affected the initiation of the rainband. For further improvement of the rainfall forecast, data assimilation that modifies atmospheric instability conditions is necessary. Therefore, we conducted data assimilation experiments with a storm-scale assimilation system for assimilating GPS observations.

5.4 Data assimilation experiments

5.4.1 Design of actual 30-min assimilation experiments

We next conducted high-resolution data assimilation and forecast experiments using NHM-4DVAR with a horizontal grid spacing of 2 km and an assimilation window of 30 min. In these experiments, multiple actual observations were assimilated, and extended 3-h forecasts were produced by the 4D-Var analysis. The forecast result described in Section 5.3 (CTL) was used as the first-guess field and for the lateral boundary conditions. The 30-min assimilation was started at 1100 JST on 19 August, and the forecast was performed from 1100 to 1400 JST using the assimilation result as the initial conditions (Fig. 5.8). We conducted three experiments in which GPS-STD, GPS-ZTD, or GPS-PWV data were assimilated every 10 min (hereafter, STD, ZTD, and PWV, respectively). Only the observations listed above, and no other kinds, were assimilated. A fourth experiment, in which no data were assimilated, is called NODA. No cumulus parameterization was used in the data assimilation and 3-h forecasts. Figure 5.9 shows the assimilation and forecast domains and the distribution of GPS observation sites used for the experiment. The distributions of GPS-STDs in the model atmosphere at each assimilation time (1100, 1110, 1120, and 1130 JST; Fig. 5.10) show that, unlike the GPS-PWV and GPS-ZTD data sets, the GPS-STD data contain a great deal of horizontal infor-

mation.

5.4.2 Results of the multi-observation assimilations with a 30-min window and forecasts

The time evolution and horizontal distribution of rainfall in NODA from 1200 to 1400 JST (Fig. 5.11a) were similar to those in CTL (Fig. 5.5a), but the maximum rainfall intensity was enhanced to 21 mm h^{-1} at 1300 JST. This improvement in NODA resulted from the increase in the horizontal resolution and the removal of the cumulus parameterization. The horizontal rainfall distributions in ZTD and PWV (Figs. 5.11b and c) resembled the rainfall distributions in NODA, but in both ZTD and PWV a rainband formed near southern Okinawa at 1300 JST and, at the same time, the rainfall intensity over northern Okinawa was strengthened to 24 mm h^{-1}. These results demonstrate that increasing the horizontal resolution improves the rainfall intensity forecast and that assimilation of GPS-ZTD and GPS-PWV data slightly improves the timing of the subsequent rainband initiation.
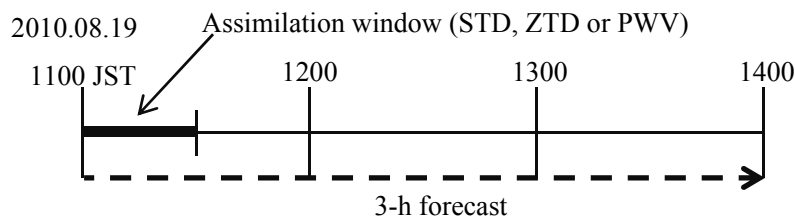
Fig. 5.8. Schematic diagram of the data assimilation and forecast experiment.
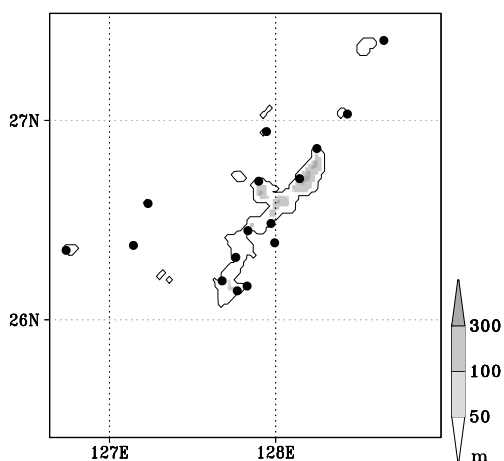
Fig. 5.9. The assimilation and forecast domain, topography and GPS observation stations.
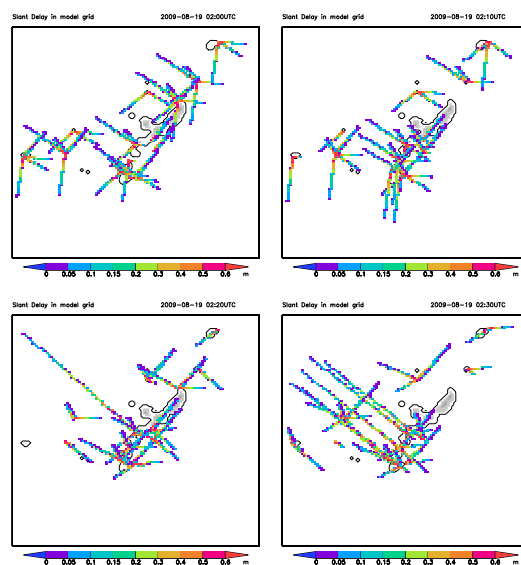
Fig. 5.10. Propagation paths of radio waves from GPS satellites to receivers in the model atmosphere, viewed in the horizontal plane. Real slant delay observations obtained over Okinawa Island at 1100 JST (upper left), 1110 JST (upper right), 1120 JST (lower left), and 1130 JST (lower right) on 19 August 2009.
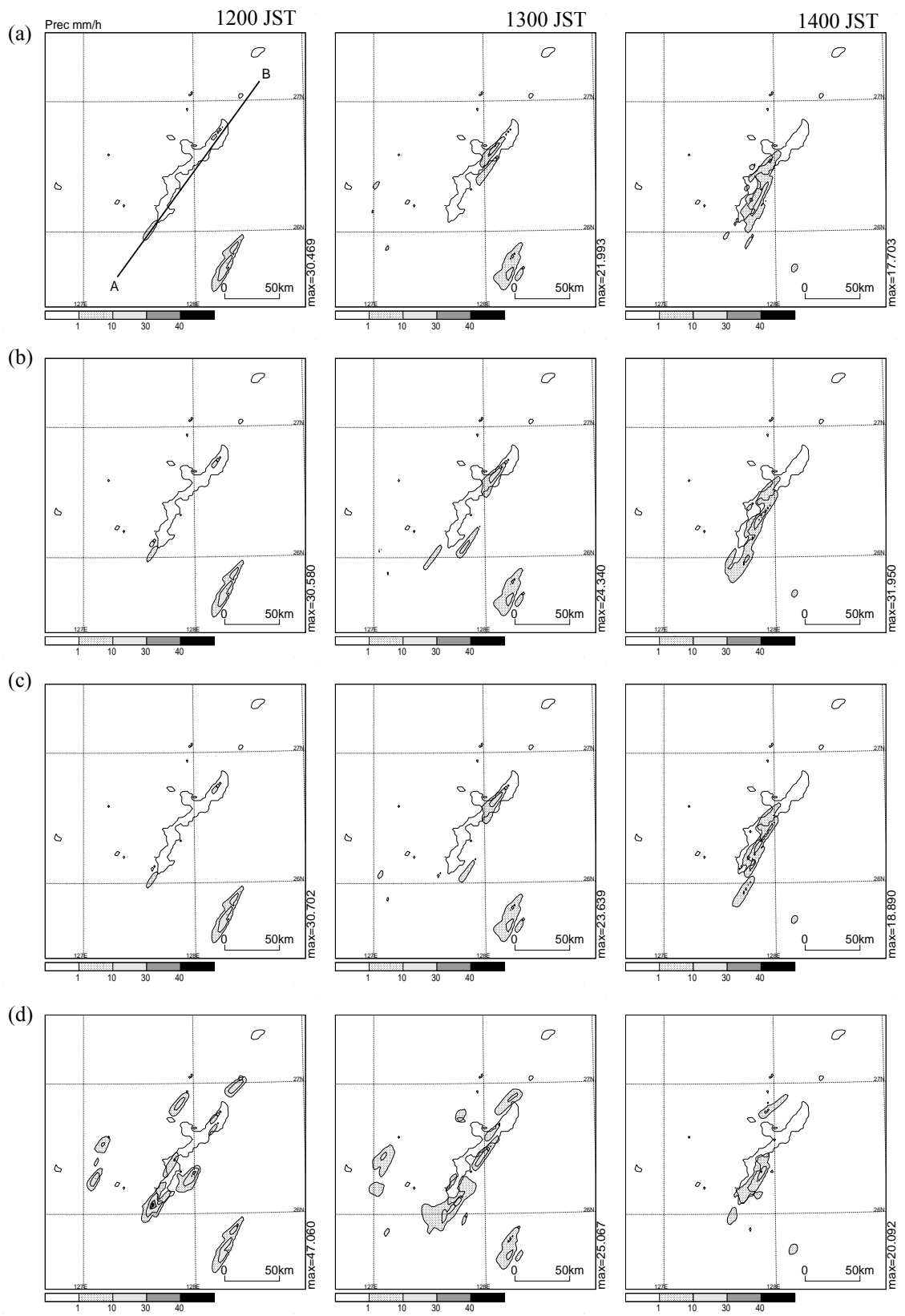
Fig. 5.11. Horizontal distribution of 1-h accumulated rainfall amount from 1200 (forecast time (FT) = 01) to 1400 (FT = 03) JST. NODA (a), PWV (b), ZTD (c), and STD (d).

In STD (Fig. 5.11d), regions of intense rainfall had already formed over southern and southwestern Okinawa at 1200 JST, and the maximum intensity reached 47 mm h^{-1}. By 1300 JST, a rainband had formed over the island, but rainfall intensity had weakened slightly to 25 mm h^{-1}. Thus, the assimilation of GPS-STD data improved the rainfall forecast with respect to both timing and intensity compared with the assimilation of GPS-PWV and GPS-ZTD data.

Comparison of θ differences between NODA and STD revealed an area of large positive increments at heights of 500 to 1500 m over the southern end of Okinawa Island and one of large negative increments at heights of 1000 to 2000 m over central Okinawa (Fig. 5.12a). Both Qv (Fig. 5.12b) and vertical wind speed (Fig. 5.12c) were increased where the mixing ratio of the cloud water was enhanced in STD. These modifications due to the assimilation of GPS-STD data led to the production of cloud water and an increase in θ due to condensation heating. Furthermore, there is an area of weak positive θ increments below the area of negative increments. This positive increment area is within the boundary layer, where it contributed to a decrease in vertical stability. In this positive θ region, the updraft was strengthened and Qv was increased in STD as well. These modi-
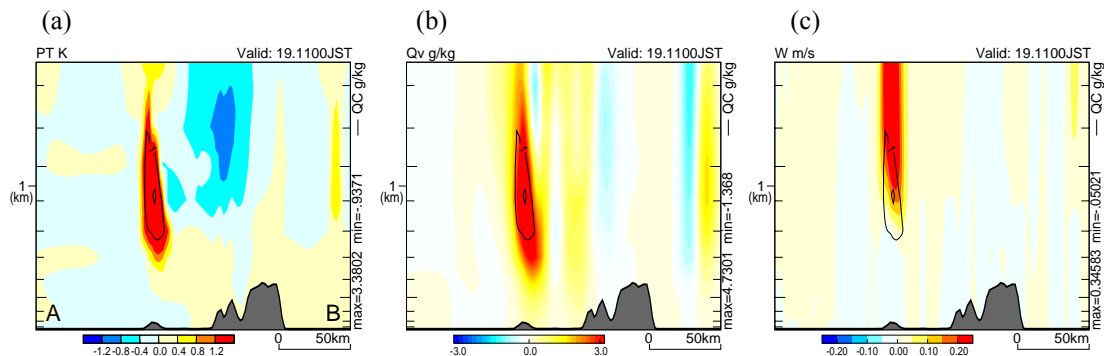
Fig. 5.12. Vertical cross sections along line A–B in Fig. 5.11a showing differences (STD minus NODA) of potential temperature (shaded) (a), the mixing ratio of water vapor (shaded) (b), and vertical wind speed (shaded) (c), and the mixing ratio of cloud water in STD (contours) (all panels), at 1100 JST (FT = 00).
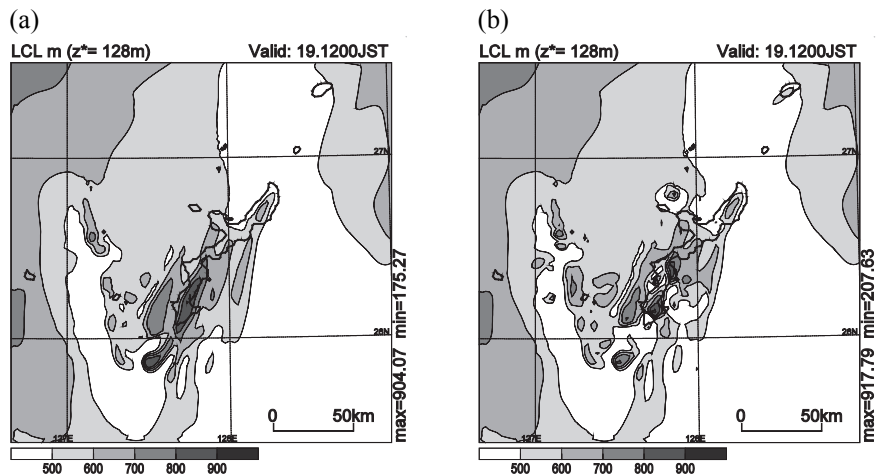
Fig. 5.13. Same as Fig. 5.7, but in NODA (a) and STD (b) at 1200 JST.

fications enhanced vertical instability and contributed to the improved timing of the rainfall forecast. The LCL results also show increased vertical instability in the GPS-STD assimilation over southern Okinawa. A stable region in NODA (Fig. 5.13a), indicated by LCLs of 800 to 900 m above southern Okinawa (similar to CTL, see Fig. 5.7), became less stable in STD (Fig. 5.13b). As a result of this increased instability in STD, convective regions began to develop over Okinawa, and the later rainfall forecast was improved compared with that in NODA.

From these results, we conclude that increasing the horizontal resolution and the removal of cumulus parameterization contributed to an improved rainfall intensity forecast (NODA), assimilation of GPS-PWV or GPS-ZTD slightly improved the timing of the rainfall forecast, and modifying the vertical thermodynamic profile by GPS-STD assimilation further improved the forecast with respect to both rainfall intensity and timing.

5.5 Summary

MCSs are often induced over Okinawa Island in summer. We therefore investigated the mechanisms responsible for the initiation of a rainband that formed on 19 August 2009. The rainband, which began to form at 1100 JST, had developed into a linear feature by 1200 JST, and it lasted until around 1600 JST.

We first investigated the factors affecting the initiation of the rainband by performing three experiments using JMA-NHM with a 5-km horizontal grid spacing: a downscaled numerical experiment (CTL), an experiment in which the islands in the model were replaced by sea (Sea), and one in which the islands were treated as flat planes and the surface roughness of the ground was set to the same value as that of the sea (NoMt). In Sea, a linear MCS did not form, whereas a rainband similar to the observed rainband developed in CTL and NoMt. The rainbands in CTL and NoMt were induced by boundary layer evolution and sea–land wind circulation over Okinawa. These results indicate that the primary factor inducing rainband formation over Okinawa is surface heating, and that updrafts caused by mountains and wind convergence caused by surface friction are not primary factors in rainband initiation. Though the rainbands were initiated in CTL and NoMt at the same location as the observed rainband, the predicted rainfall was delayed, and its intensity was weaker than the observed. Further, both CTL and NoMt failed to reproduce the observed rainfall over southern Okinawa.

To address these problems, we next conducted high-resolution simulations with data assimilation using NHM-4DVAR and a 2-km horizontal grid spacing with a horizontal resolution of 2 km using multiple actual observations from different sites. The forecast from the first-guess field (NODA) indicated that increasing the horizontal resolution resulted in greater rainfall intensity than in the 5-km downscaled experiment (CTL). The GPS-ZTD and GPS-PWV assimilations produced improved forecasts compared to NODA, but there remained timing and positional lags. The

GPS-STD assimilation clearly improved the forecast of both the timing and intensity of the rainfall. This improved forecast reflected the decreased atmospheric stability over Okinawa, especially over southern Okinawa, and the improvement of the initial conditions around the island that resulted from the assimilation of GPS-STD data.

GPS-STD data include information about temperature, dry atmospheric pressure, and water vapor pressure (see Eq. 2.29). In addition, GPS-STD data contain both horizontal and vertical information about those atmospheric elements. Atmospheric inhomogeneity is greatest in the lower troposphere (1–4 km height; see figure 1b of Shoji (2013)). Assimilating GPS-STD data that included information on the distribution of humid air improved the rainband forecasts. A GPS signal following a path with a 15° elevation angle travels about 11 km horizontally and propagates vertically 3 km. Therefore, the high-resolution data assimilation system used in this study was able to take advantage of the additional information in the GPS-STD data. Larger analysis increments were obtained in the lower troposphere by the high-resolution 4D-Var data assimilation system with GPS-STD assimilation than with GPS-ZTD or GPS-PWV assimilation (see Section 2.4.5d). As a result, in the subsequent experiments in which actual observation data were assimilated, GPS-STD assimilation resulted in improved simulation of atmospheric conditions compared with GPS-ZTD or GPS-PWV assimilation.

In future work, the observational error model and the data thinning method used in this study should be updated and made more sophisticated. In addition, the assumption of linear propagation (neglecting the bending effect) needs to be removed, because it introduces errors in low-elevation observations. In addition, this study shows that assimilating environmental filed observations can expand predictability of MCSs. More developments on assimilating other environmental observations (e.g., Doppler lidar, refractivity from radars) are needed.

Chapter 6

General Discussions

In this chapter, the scale of the environmental fields of initiation and sustainment of localized MCSs is discussed based on the results obtained in Chapters 3-5. Three case studies suggest that MCSs are initiated by a low-level convergence with a moist air over a horizontal scale of approximately 50 km. The predictability of meso β-γ MCSs is also found to depend on assimilating observations of wind, humidity, and temperature observations on a 50×50 km area around the MCS at low levels. On the other hand, due to nonlinearity, the assimilating rain water produces limited improvement. Thus, assimilating environmental information is important to improve the predictability of MCSs. Based on this discussion and the advanced data assimilation system (Chapter 2), the preferred observation systems (e.g., Doppler lidar, rapid scan by geostationary satellites) and assimilation systems for localized MCS forecasts (e.g., weak constraint 4D-Var, particle filter) are discussed.

6.1 Scales of environmental fields corresponding to initiation and sustainment of localized MCSs

As mentioned by Fujibe (2002), isolated thunderstorms that occurred over the Kanto Plain are often initiated with a meso β scale convergence between the southerly sea breeze from Tokyo Bay and the northeasterly sea breeze from the Pacific Ocean (the 'E-S type wind system' named by Fujibe (2002)). The Nerima heavy rainfall event was typical of this process. Due to the sunshine and the convergence caused by the sea breezes, a localized front with a horizontal scale of 100 km was formed (Fig. 3.5). A small air mass with high temperature and humidity existed over the convergence zone. The scale of the air mass was 50 km in east-west direction, 50 km in north-south direction (Fig. 3.18) and 1.5 km in height (Figs. 3.20, 6.1). Because the southerly sea breeze lifted the air mass, the thunderstorm initiated at its top. In these phenomena, the humid air mass and localized convergence were essential for the initiation process of the thunderstorm. Thus, detecting the scale and intensity

of the air mass were prerequisites for forecasting the thunderstorm.

The humid air that induced the heavy rainfall merits detailed discussion. Due to their small horizontal scale and a lack of appropriate observation methods, it has been difficult to even observe such small air masses. The recent development of GPS meteorology has allowed observation campaigns for observing small-scale water vapor distribution. The first campaign was the Tsukuba GPS dense net campaign observation (Shoji et al. 2004) in Japan, followed by the International H_2O Project (IHOP 2002; Weckwerth et al. 2008) in the U.S.A. In order to detect 3-dimensional water vapor distribution, GPS tomography techniques had to be developed. Seko et al. (2004c) used these methods to clarify that convection initiation first occurred in a small-scale (20×20 km) water vapor zone. In addition, Champollion et al. (2009) showed that a squall line was strengthened by water vapor, using a 100×100 km scale. GPS tomography techniques do however have some limitations, as they utilize broad assumptions; while water vapor distribution is analyzed, wind and temperature distributions are not. These limitations make it difficult to consider the interaction between water vapor and dynamical fields in detail. Numerical simulations also have difficulty in simulating the location and timing of MCSs, as described in Section 1.3.

This study first reviewed the precise behavior of the humid air when a convective cell initiates. The warm and humid air on the surface convergence zone is shown to have been lifted by the sea breeze from Tokyo Bay. The cumulonimbus then initiated and caused the heavy rainfall at Nerima. The GPS-PWV distribution (Fig. 3.14) and horizontal wind (Fig. 3.13) suggest that the water vapor advected from the northeast part of the Kanto Plain. The air mass was heated by high surface temperatures on the Kanto Plain, while the sea breeze was relatively cold. Moreover, the speed of the sea breeze was higher than that of the terrestrial air mass, and the warmer humid terrestrial air was therefore lifted over the relatively cooler air from the sea. If the humid air had advected from the sea, the air mass would have been heated by the land and the convection initiation would have been delayed and shifted northwards. The convection-initiating location is hence determined by the origin of the water vapor.

In the Naha heavy rainfall event, the initiation process of the line-shaped rain band progressed as follows. First, a boundary layer whose top reached a height of 1 km was formed in the morning over Okinawa Island, likely due to sunshine (Fig. 5.6). Next, updrafts were generated near the top of the boundary layer (1 km height), and finally convection was initiated. Because there was a sea breeze circulation atop the general wind field, two updrafts were generated at the windward and leeward of Okinawa Island. The leeward convection did not appear in NODA, PWV, and ZTD, illustrating why it is important to improve the atmospheric stability forecast in the boundary layer (Fig. 5.12) by assimilating GPS-STD to improve spatial and temporal accuracy of rainfall forecasts. It is suggested that the typical horizontal scale is approximately 30 km (see south of Okinawa in Fig. 5.13) and the typical vertical scale is approximately 2 km (Fig. 5.12). Temperature and humidity are

also major meteorological factors in the initiation of the convection. These two case studies allow the conclusion that small-scale thunderstorms initiate in unstable, humid, warm air over a horizontal scale of approximately 50 km when a localized convergence zone exists.

The sustainment mechanism of the Nerima and Suginami heavy rainfall events also merit discussion. In the Nerima event, a thunderstorm with an east-west scale of 30 km developed until the top of the thunderstorm reached 15 km height (Fig. 3.22). Because the humid and warm air flowing to the thunderstorm from the sea breeze was cooled by raindrop evaporation, the thunderstorm vanished. The wind speed of the sea breeze was approximately 10 m s^{-1}, allowing it to travel approximately 40 km in 1 h. This value is consistent with the scale of the air mass. The horizontal scale of the air mass and the speed of the inflow wind at low levels are clearly crucial to the evolution and sustainment of the thunderstorm.

On the other hand, the rain band already existed before the assimilation experiment in the Suginami heavy rainfall event. The initiation mechanism was therefore not examined in this study, but the sustainment of the rain band was investigated. The results showed that the rain band existed in the model for only 30 min after two assimilation windows (Fig. 4.7). This short sustainment time was mainly due to weak inflow in the model, as discussed in Sections 4.5.3 and 4.6.1. The sustainment period may be estimated to be 30 min using Figs. 4.8 and 4.12. Water vapor and potential temperature fields differ between ref and wo-ref primarily at low levels (1-2 km height). The scale of the difference is approximately 20 km on both sides of the rain band (Fig. 4.8). Figure 4.12 shows that the inflow-wind field differs on the east and south sides of the rain band; this scale is approximately 30 km. It is therefore suggested that sustainment of the rain band for 30 min requires a 30-km scale of environmental fields (inflow, water vapor and temperature). This scale, which derives from estimation using the analysis increments, is similar to the distance that the inflow traveled over its lifetime. These two case studies lead to the conclusion that the sustainment scale of a thunderstorm is determined by the wind speed of the inflow and the amount of water vapor.

6.2 Nonlinearity in MCS

As shown in Section 2.4.4, assimilating rainwater in a cloud-free region creates difficulty in reproducing convection in numerical models. The problem demonstrates that the relationships between rainwater and cumulonimbus and environmental fields (i.e., horizontal wind convergence, water vapor distribution, updraft in the cloud) are uncertain. When rainwater exists at a certain point in the atmosphere, a number of descriptive factors need to be ascertained, including whether the rainwater is ascending or descending, the amount of cloud water around the rainwater, convergence or divergence of horizontal wind on the surface, and the advection rate of water vapor into the cloud. If a sufficiently long time-assimilation window can be set up and rain water distribution assimilated

within it, the environmental field may be determined almost completely. As discussed by Wang et al. (2012), an assimilation window longer than 1 h is however very difficult to apply in convective situations due to the nonlinearity of MCSs and numerical models.

Existence of the nonlinearity can be confirmed by the differences between tangent linear and nonlinear model predictions. As discussed in section 4.6.2, the jump in Fig. 4.14 is caused by the differences between these models. The tangent linear model predicts meteorological phenomena along the trajectory predicted by the nonlinear model; where the nonlinear model fails, the tangent linear model therefore cannot predict precise phenomena, especially MCS with strong nonlinearity. Wang et al. (2013) succeeded in forecasting a squall line with the incremental WRF 4D-Var system with 4 km horizontal grid spacing. However, this success concerened a large-scale squall line of 200−400 km, and not each cumulonimbus was predicted precisely. The long assimilation window and the linearization of the nonlinear models still present difficulties.

These can be resolved by reducing the uncertainty of the environmental field. Innovative observations of environmental fields or advancement of existing observation operators are extremely important in this regard. In addition, nonlinearity might be somewhat alleviated by advancement of the 4D-Var system itself. A weak-constraint 4D-Var and a hybrid 4D-Var are potential candidates. These topics will be discussed in detail in the next section.

6.3 Data assimilation and observing systems for localized heavy rainfall forecasts

In this section, the suitable data assimilation and observation systems for localized heavy rainfall
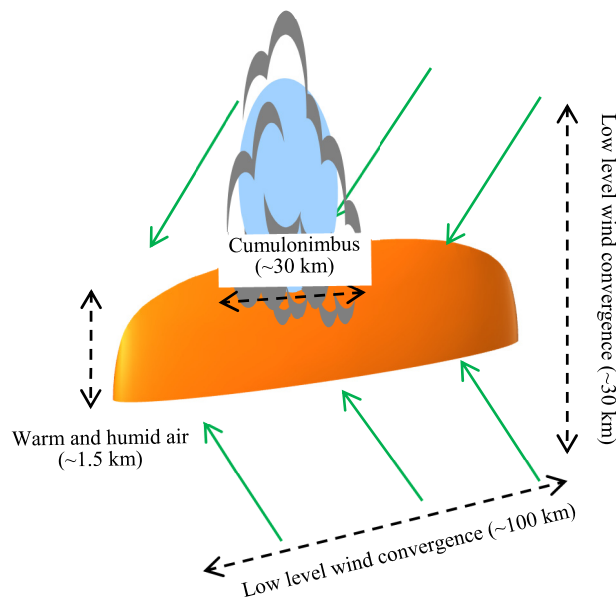
Fig. 6.1. Schematic of the horizontal scale of the Nerima heavy rainfall event. The warm, humid air mass (orange), horizontal wind convergence (green vectors), and cumulonimbus (gray and blue) are illustrated.

events are discussed. The initiation process of thunderstorms is only weakly nonlinear; if the environmental fields are well observed, the initiation of a thunderstorm can thus be accurately forecast as shown in Chapters 3 and 5. Furthermore, when the information pertaining to the environmental fields is given with sufficient range (50 km from the initiation point of the MCS), the development and sustainment process of thunderstorms can also be forecast as described in the previous sections. Observing environmental fields (wind, water vapor, and temperature) at the initiation stage of localized heavy rainfall events and assimilating them is therefore essential for the successful forecasting of localized MCSs. From the viewpoint of disaster prevention, these observation systems must be operated routinely and be deployed widely and at high density. Remotely sensing should be employed because the horizontal scale of localized heavy rainfalls is very small. In this thesis, Doppler radars were used to measure the wind field, GPS observations were used to measure water vapor and temperature fields, and surface observations were used to measure temperature and wind speed near the ground.

Doppler radars are subject to limitations in observing outside rainfall areas, as they cannot observe the surrounding airflow of cumulonimbus systems. In the Suginami heavy rainfall event, this disadvantage caused a lack of forecasts of the rain band (Section 4.6.1). In the Nerima heavy rainfall event however, the wind shear field derived from the clear air echoes is shown in Figs. 3.12 and 3.18. These echoes provided information on wind flow before the thunderstorm initiation. It is well known that clear air echoes are often observed on calm, clear days in warm seasons (Kusunoki 2002). In contrast, Doppler Wind Lidars (DWLs) observe the wind flow field in clear air, but not within rainfall regions. JMA operates two DWLs at the Haneda airport and one at the Narita airport. As of 2013, Hokkaido University operates one DWL at Ookayama, and the National Institute of Information and Communications Technology (NICT) operates a DWL at Koganei city, both west of Tokyo. These four DWLs cover an area over 50 km in length and 20 km in width. Kawabata et al. (2013a) demonstrated that assimilating the DWL at the NICT Koganei observatory effectively influenced the forecast of a localized heavy rainfall event (Fig. 6.2). Observation ranges of Doppler radars and DWLs are 100–200 km and 10–20 km, respectively. The range of DWLs may be too short to capture the environmental field, but when DWLs become a part of an observation network, data at unavailable locations can be inferred from other measurements. Clear-air echoes obtained by Doppler radars and DWLs thus have obvious potential as observing systems for the inflow wind field.

Water vapor and temperature observations for the Naha heavy rainfall event were provided by GPS-STD assimilation. These elements are difficult to observe over a wide range, but several improvements are currently being developed. One potential improvement, the estimation of the refractive index using Doppler radar, is an innovative way to observe water vapor. Fabry et al. (1997) estimated the near-surface refractive index using phase data from Doppler radar. The refractive index provides information on the horizontal distribution of water vapor and temperature in the radar ob-

servation range. Seko et al. (2009) estimated the temporal variation of the refractive index using a C-band Doppler radar and showed the impact on a rainfall forecast (Seko, personal communication). Another potential improvement comes from Furumoto et al. (2007), who developed a method to estimate humidity profiles from wind profiles, and Kawabata et al. (2011a) showed the effect of assimilation using virtual temperature profiles provided from RASS (radio acoustic sounding system) on a rainfall forecast. While there may be some difficulty in applying these techniques to a practical NWP, they have great potential. The observation densities of wind profilers and RASS may be coarse, but Doppler radars can estimate the refractive index over a 100–200 km range.

Rapid-scan observations by geostationary satellites can recognize the initiation of cumulonimbus over a very short time interval (1–5 min), minutes earlier than radar observations. It may prove easy to use high-frequency air motion vectors from rapid scans, but many problems in assimilating radiative data from rapid-scan observations (i.e. nonlinearity and radiation transfer models) still persist. The assimilation will however be useful for localized rainfall forecasts.

In discussing desirable assimilation systems for localized MCSs, 'multi-scale' and 'nonlinearity' must be important key words. Observational instruments represent various scales in time and space; because localized MCSs occur at very small scales and yet have wider environmental fields, multiple scales must be considered in assimilating observations. Seko et al. (2013) have been developing the two-way nested LETKF system, a useful solution to this 'multi-scale' problem. In this system, conventional observations are assimilated into the coarse domain of the LETKF system, while high-resolution observations (i.e., radar data) are assimilated into the fine domain.

Flow-dependency and model error are important in tackling nonlinearity. Statistical background errors were used in this thesis. Because background errors in localized MCSs vary with hourly atmosphere data, it is necessary to incorporate flow-dependency into the errors. A hybrid 4D-Var assimilation system has been proposed to address this (Hamill and Snyder 2000; Lorenc 2003;
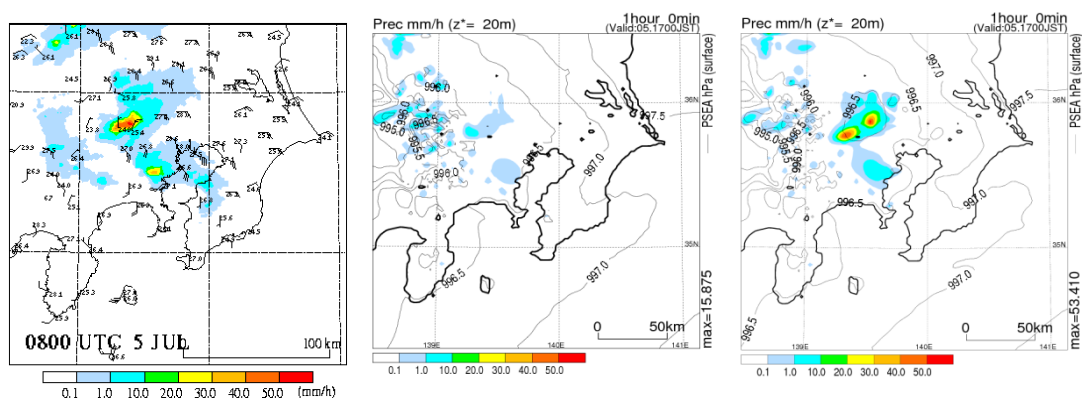
Fig. 6.2. Rainfall intensity (mm h^{-1}) from the radar observations (left), the forecast result without the DWL assimilation (middle), and the forecast result with the DWL assimilation (right). The rainfall intensity and distributions of the forecast result with the DWL assimilation are close to that of the observation. After Kawabata et al. (2013a).

Buehner 2005) and is under development for NHM-4DVAR.

A weak-constraint 4D-Var is valid as an advanced assimilation system that takes nonlinearity into account, and has operated in ECMWF (European Centre for Medium-Range Weather Forecasts; Fisher et al. 2005). This method uses model errors and has a variable-length assimilation window. These approaches are helpful for forecasting localized heavy rainfall events. As a fully nonlinear and non-Gaussian method, a particle-filtering system for such forecasts is likely in the future.

Chapter 7

General Conclusions

In this thesis, a prototype of a non-hydrostatic 4D-Var was advanced to a cloud-resolving non-hydrostatic 4D-Var (NHM-4DVAR). NHM-4DVAR is the first 4D-Var system (i) based on a full non-hydrostatic model, (ii) with a high horizontal resolution of 2 km, and (iii) equipped with many types of observation operators for remote-sensing observation networks. One existing 4D-Var system is cloud-resolving (VDRAS; Sun and Crook 1997) but adopts a simple forward model and only a few types of observation operators. Using NHM-4DVAR, three case studies were conducted to clarify the mechanisms of meso convective systems (MCSs) and improve predictability of heavy rainfall forecasts.

The first case study illustrated that a cumulonimbus initiated in a meso-γ scale atmosphere with high equivalent temperature, and that the cloud activity ended with the dispersal of the air mass. Here, NHM-4DVAR v1 was applied to the Nerima heavy rainfall event. Radial wind data from Doppler radars, precipitable water vapor data from GPS, and surface temperature and wind data were assimilated. The Nerima heavy rainfall event was well reproduced in the assimilation and the subsequent forecast with respect to the time series of 10-minute rainfall amounts and radar reflectivity, clarifying its formation mechanism. A surface convergence line of horizontal winds with a horizontal scale of 100 km was formed from a southerly sea breeze and northeasterly winds, and an air mass with high equivalent potential temperature accumulated at heights of up to 1.5 km over the Kanto Plain around Nerima. This air mass was lifted to generate cumulonimbi that caused the event. The result first showed that it is possible to predict MCSs of a meso-γ scale with accurate intensity, occurrence time and location predictions when suitable conditions are assimilated before convection initiation.

In the second study, an assimilation experiment was performed on the Suginami heavy rainfall event. Radar reflectivity, radial wind, GPS-PWV, and surface observation data were assimilated. NHM-4DVAR v2 reproduced a line-shaped rain band whose shape and intensity were consistent with observations; assimilation of radar reflectivity data intensified the rain band and suppressed false convection. Sustaining the low-level convergence produced by northerly winds in the western part of the rain band was the key to prolonging the predictability of the convective system. The result shows that the QPF with radar reflectivity assimilation was significantly superior to that without radar reflectivity. The nonlinearity of deep convection was also investigated. From single-observation

assimilations, we conclude that due to nonlinearity it is quite difficult to create and maintain modelled new convection from assimilation of individual observations of rainwater. This difficulty induced by nonlinearity in convections limited the influence of assimilating observations inside an MCS to areas outside of the MCS within a short range (30 km), reducing predictability.

NHM-4DVAR v2 incorporating the assimilation of GPS-STD data was applied to the Naha heavy rainfall event. Through simulations with JMA-NHM using a 5 km horizontal grid spacing, it was found that the primary factor affecting rain band initiation was land surface heating. Heating-induced instability of the atmosphere and MCS initiation are closely connected. Further simulations with a 2 km horizontal grid spacing and assimilations of GPS-PWV, ZTD and STD were also conducted. Comparison of these results showed that increased horizontal resolution improved predicted rainfall intensity. GPS-STD assimilation significantly improved the water vapor and temperature fields over a wide area and yielded a clearly improved forecast in terms of both rainfall timing and intensity compared with the GPS-ZTD and GPS-PWV assimilations. This result indicates that assimilating environmental information has the capability to improve the predictability of MCSs.

Based on the three case studies, this thesis showed that (i) MCSs producing heavy rainfall events the warm season in Japan initiate when low-level wind with a moist air converges over a horizontal scale of approximately 30–50 km;,(ii) the MCS could be predicted with some skill when wind, temperature, and humidity data at low levels are well assimilated; (iii) it is difficult to sustain strong convection in a model for long periods, because assimilating observations inside the MCS (i.e., radar reflectivity) does not reduce the analysis error over a sufficiently wide area due to the nonlinearity involved in the cloud microphysics. Obtaining observations outside MCSs (i.e., Doppler Wind Lidars and rapid-scanning observations derived from geostationary satellites) is important to solve this problem. Due to nonlinearity, assimilating environmental observations rather than inside information within the MCSs is the key to improve the predictability of the MCS. A data assimilation system addressing nonlinearity and multi-scale treatments has to be developed to tackle these issues.

References

Aksoy, A., D. C. Dowell, and C. Snyder, 2009: A multicase comparative assessment of the ensemble Kalman filter for assimilation of radar observations. Part I: Storm-scale analyses. *Mon. Wea. Rev.*, **137**, 1805–1824.

Andrews, A., 1968: A square root formulation of the Kalman covariance equations. *AIAA J.*, **6**, 1165-1168.

Barker, D. M., W. Huang, Y.-R. Guo, A. J. Bourgeois, and Q. N. Xiao, 2004: A three-dimensional variational data assimilation system for MM5: Implementation and initial results. *Mon. Wea. Rev.*, **132**, 897–914.

Bauer, H.-S., V. Wulfmeyer, T. Schwitalla, F. Zus, M. Grzeschik, 2011: Operational assimilation of GPS slant path delay measurements into the MM5 4DVAR system. *Tellus*, **63A**, 263-282.

Bean, B. R., and G. D. Thayer, 1959: Central Radio Propagation Laboratory Exponential Reference Atmosphere. *J Res Natl Bur Stand*, **64D**, 315-317.

Bergthorsson, P. and B. Doos, 1955: Numerical weather map analysis, *Tellus*, **7**, 329-340.

Bishop, C.H., B. Etherton and S.J. Majumdar, 2001: Adaptive sampling with the ensemble transform Kalman filter. Part I: Theoretical aspects. *Mon.Wea.Rev.*, **129**, 420-436.

Blumberg, A.F. and G.L. Mellor. 1987: A description of a three-dimensional coastal-circulation model. In: Heaps N ed. Three-Dimensional Coastal Ocean Models, *American Geophysical Union*, **4**, 208.

Boudouris, G., 1963: On the index of refraction of the air, the absorption and dispersion of centimeter waves by gasses. *J. Res. Natl. Bur. Stand.*, **67,** 631–684.

Buehner, M., 2005: Ensemble-derived stationary and flow-dependent background-error covariances: Evaluation in a quasi-operational NWP setting. *Quart. J. Roy. Meteor. Soc.*, **131**, 1013–1043.

Chang, C., and M. Yoshizaki, 1991: A Numerical study of the mesoscale convective system observed over Okinawa Island in Jun 1987. *Mon. Wea. Rev.*, **119**, 2724-2733.

Charney, J.G., R. Fjørtoft, and J. von Neumann, 1950: Numerical integration of the barotropic vorticity equation. *Tellus*, **2**, 237-254.

Courtier, P., J. N. Thepaut, and A. Hollingsworth, 1994: A strategy for operational implementation of 4D-Var, using an incremental approach. *Q. J. R. Meteorol. Soc.*, **120**, 1367–1387.

Daley, R., 1991: *Atmospheric Data Analysis*. Cambridge University Press, 457pp.

Deardorff, J. W., 1980: Stratocumulus-capped mixed layers derived from a three-dimensional model, *Boundary-Layer Met.*, **18**, 495-527

Dee, D. P. and A. M. Da Silva, 2003: The choice of variable for atmospheric moisture analysis. *Mon. Wea. Rev.*, **131,** 155-171.

Doms, G. and U. Schaettler, 1999: The Nonhydrostatic Limitedarea Model LM of DWD. Part I. *Scientific Documentation*, DWD.

Dudhia, J., 1993: A nonhydrostatic version of the Penn State-NCAR mesoscale model: Validation tests and simulation of an Atlantic cyclone and clold front. *Mon. Wea. Rev.*, **121**, 1493–1513.

Eliassen, A. 1954: *Provisional report on calculation of spatial covariance and autocorrelation of the pressure field.* Inst. Weather and Climate Res., Acad. Sci. Oslo, Rep. No. 5. Reprinted in: Data assimilation methods. Ed. L. Bengtsson, M. Ghil, E. Kdlen, Springer Verlag, 319-330.

Evensen, G., 1994: Sequential data assimilation with a nonlinear quasi-geostrophic model using Monte Carlo methods to forecast error statistics. *J. Geophys. Res.*, **99 (C5)**, 10143-10162.

Fabry, F., C. Fruch, I. Zawadzki, and A. Kilambi, 1997: On the extraction of near-surface index of fraction using radar phase measurements from ground targets. *J. Atmos. Oceanic. Technol.*, **14**, 978-987.

Fisher, M., M. Leutbecher, and G. A. Kelly, 2005: On the equivalence between Kalman smoothing and weak-constraint four-dimensional variational data assimilation. *Q. J. R. Meteor. Soc.*, **131**, 3235-3246.

Fujibe, T., 2002: Surface wind patterns preceding short-time heavy rainfall in Tokyo in the afternoon of midsummer days, *Tenki*, **49**, 393-405 (in Japanese).

Furumoto, J., S. Imura, T. Tsuda, H. Seko, T. Tsuyuki, K. Saito, 2007: The variational assimilation method for the retrieval of humidity profiles with the wind-profiling radar. *J. Atmos. Oceanic Technol.*, **24**, 1525–1545.

Gal-Chen, T. and R. C. J. Somerville, 1975: On the use of a coordinate transform for the solution of the Navier-Stokes equation. *J. Comp. Phys.*, **17**, 209-228.

Gandin, L. S., 1963: *Objective Analysis of Meteorological Fields*, Gidrometeorologicheskoe Iz-datelstvo, Leningrad (in Russian), English translation by Israeli Program for Scientific Translations, Jerusalem, 1965.

Gilchrist, B. and G. Cressman, 1954: An experiment in objective analysis. *Tellus*, **6**, 309-318.

Guo, Y.-R., Kuo, Y.-H., Dudhia, J., Parsons, D., Rocken, C., 2000: Four-dimensional variational data assimilation of heterogeneous mesoscale observations for a strong convective case. *Mon. Wea. Rev.*, **128**, 619-643.

Gustafsson, N., L. Berre, S. Hörnquist, X-Y., Huang, M. Lindskog, B. Navascués, K. S. Mogensen, S., Thorsteinsson, 2001: Three-dimensional variational data assimilation for a limited area model. Part I: General formulation and the background error constraint. *Tellus*, **53A**, 425–446.

Gustafsson, N., X. Huang, X. Yang, K. Mogensen, M. Lindskog, O. Vignes, T. Wilhelmsson, and S. Thorsteinsson, 2012: Four-dimensional variational data assimilation for a limited area model. *Tellus*, **64**, 1-29.

Ha, S., Y.-H. Kuo, Y.-R. Guo, and G.-H. Lim, 2003: Variational assimilation of slant-path wet delay measurements from a hypothetical ground-based GPS network. Part I: Comparison with precip-itable water assimilation. *Mon. Wea. Rev.*, **131**, 2635-2655.

Hamill, T. M., and C. Snyder, 2000: A hybrid ensemble Kalman filter–3D variational analysis scheme. *Mon. Wea. Rev.*, **128**, 2905–2919.

Honda, Y., T. Kawabata, K. Tamiya, K. Aonashi, T. Tsuyuki, K. Koizumi, 2003: A nonhydrostatic 4-dimensional variational analysis model without moist processes – The development report of the JNoVA-4DVAR (1st) -. *Preprints of autumn meeting of Meteorological Society of Japan*, **84,** 63 (in Japanese).

Honda, Y., M. Nishijima, K. Koizumi, Y. Ohta, K. Tamiya, T. Kawabata, T. Tsuyuki: 2005, A pre-operational variational data assimilation system for a nonhydrostatic model at Japan Mete-

orological Agency: Formulation and preliminary results, *Q. J. R. Meteor. Soc.*, **131**, 3465-3475.

Honda, Y. and K. Sawada, 2009: Upgrade of the operational mesoscale 4D-Var at the Japan Meteorological Agency. *CAS/JSC WGNE Res. Activ. Atmos. Oceanic Modell.*, **39**, 01.11-01.12.

Huang, X., and Coauthors, 2009: Four-dimensional variational data assimilation for WRF: Formulation and preliminary results. *Mon. Wea. Rev.*, **137**, 299–314.

Hunt, B. R., E. Kalnay, E. J. Kostelich, E. Ott, D. J. Patil, T. Sauer, I. Szunyogh, J. A. Yorke, and A. V. Zimin, 2004: Four-dimensional ensemble Kalman filtering. *Tellus*, **56A**, 273-277.

Ikawa, M. and K. Saito, 1991: Description of a non-hydrostatic model developed at the Forecast Research Department of the MRI. *Tec. Rep. MRI*, **28**, 238 pp.

Japan Meteorological Agency, 1961: *Official Report of Typhoon Vera.* Japan Meteorological Agency 891p.

Japan Meteorological Agency, 1968: Chapter 4: The routine of the numerical weather prediction, *The report of the Numerical Prediction Division of the Japan Meteorological Agency*, **10**, 77-96 (in Japanese).

Järvinen, H., R. Eresmaa, H. Vedel, K. Salonen, S. Niemelä, and J. de Vries, 2007: A variational data assimilation system for ground-based GPS slant delays. *Q. J. R. Meteorol. Soc.*, **133**, 969–980.

Kalman, R. E., 1960: A new approach to linear filtering and prediction problems. *Trans. ASME, Ser. D, J. Basic Eng.*, **82**, 35-45.

Kalnay, E., 2003: *Atmospheric Modeling, Data Assimilation and Predictability*, Cambridge University Press, 341p.

Kashiwagi, K., 1983: The troposphere analysis system. *The report of the Numerical Prediction Division of the Japan Meteorological Agency*, **29**, 5-17. (in Japanese).

Kato, T., 1998: Numerical simulation of the band-shaped torrential rain observed over southern Kyushu, Japan on 1 August 1993. *J. Meteor. Soc. Japan*, **76**, 97-128.

Kato, T., and K. Aranami, 2005: Formation factors of 2004 Niigata-Fukushima and Fukui heavy rainfalls and problems in the predictions using a cloud-resolving model, *SOLA*, **1**, 1-4.

Kawabata, T., Y. Honda, K. Tamiya, K. Aonashi, T. Tsuyuki, K. Koizumi, 2003: The observation assimilation experiment by using NHM-4DVAR – The development report of the JNoVA-4DVAR (2nd) -. *Preprints of autumn meeting of Meteorological Society of Japan*, **84,** 420. (in Japanese).

Kawabata, T., T. Kuroda, Y. Honda, K. Tamiya, K. Aonashi, T. Tsuyuki, and K. Koizumi, 2004: A 4DVAR data assimilation system for the JMA Nonhydrostatic model to assimilate water vapor data, *Preprints of spring meeting of the Meteorological Society of Japan*, **85**, 106 (in Japanese).

Kawabata, T., H. Seko, K. Saito, T. Kuroda, K. Tamiya, T. Tsuyuki, Y. Honda, and Y. Wakazuki, 2007: An assimilation and forecasting experiment of the nerima heavy rainfa11 with a cloud-resolving nonhydrostatic 4-dimensional variational data assimilation system. *J. Meteor. Soc. Japan,* **85,** 255–276.

Kawabata, T., J. Furumoto, S. Satoh, 2011a: The impact of RASS observations on a rainfall forecast in the Okinawa heavy rainfall event. *Preprints of autumn meeting of Meteorological Society of Japan*, **99,** 170. (in Japanese).

Kawabata, T., T. Kuroda, H. Seko, and K. Saito, 2011b: A cloud-resolving 4D-Var assimilation experiment for a local heavy rainfall event in the Tokyo metropolitan area. *Mon. Wea. Rev.*, **139**,

1911-1931.

Kawabata, T., M. Kunii, K. Bessho, T. Nakazawa, N. Kohno, Y. Honda, K. Sawada, 2012: Reanalysis and reforecast of Typhoon Vera (1959) using a mesoscale four-dimensional variational assimilation system. *J. Meteor. Soc. Japan*, **90**, 467-491.

Kawabata, T., H. Iwai, H. Seko, Y. Shoji, K. Saito, S. Ishii, and K. Mizutani, 2013a: Impact of Doppler wind lidar assimilation on a heavy rainfall forecast at a meso-beta scale. *Mon. Wea. Rev.*, (submitted).

Kawabata, T., Y. Shoji, H. Seko, and K. Saito, 2013b: A numerical study on a mesoscale convective system over a subtropical island with 4D-Var assimilation of GPS slant total delays. *J. Meteor. Soc. Japan*, **91**, 705-721.

Koizumi, K., Y. Ishikawa, and T. Tsuyuki, 2005: Assimilation of precipitation data to the JMA mesoscale model with a four-dimensional variational method and its impact on precipitation forecasts. *SOLA*, **1**, 45–48.

Kondo, J., 1975: Air-sea bulk transfer coefficients in diabatic conditions. *Boundary-Layer Meteor.*, **9**, 91-112.

Kuroda, T., T. Kawabata, Y. Wakatsuki, 2005: The forecast error correlations of a high resolution meso-scale nonhydrostatic model. *Preprints of autumn meeting of Meteorological Society of Japan*, **88,** 479. (in Japanese).

Kusunoki, K., 2002: A Preliminary Survey of Clear-Air Echo Appearances over the Kanto Plain in Japan from July to December 1997. *J. Atmos. Oceanic Technol.*, **19**, 1063–1072.

Lewis, M.J. 2009: Sasaki's Pathway to deterministic data assimilation, *Data Assimilation for Atmospheric, Oceanic and Hydrologic Applications,* Park and Xu (Eds,), Springer, 1-20.

Lions, J. L., 1971: *Optimal Control of Systems Governed by Partial Difference Equations*, Springer, 396pp.

Lorenc, A., 1981: A global three-dimensional multivariate statistical interpolation scheme. *Mon. Wea. Rev,.* **109**, 701–721.

Lorenc, A. C., 2003: The potential of the ensemble Kalman filter for NWP - a comparison with 4D-Var. *Quart. J. Roy. Meteor. Soc.*, **129**, 3183–3203.

Lynch, P., 2006: *The Emergence of Numerical Weather Prediction: Richardson's Dream.* Cambridge University Press, Cambridge, 279p.

Marchuk, G.I., 1975a: Formulation of the theory of perturbations for complicated models. *Appl. Math. Optimi.*, **2**, 1-33.

Marchuk, G. I., 1975b: Formulation of the theory of complicated models. Part II: Weather prediction. *Geofisica International*, **2**, 1-33.

Mikami, A., T. Kawabata, S. Satoh, J. Furumoto, S. Nagai, Y. Murayama, and T. Tsuda, 2011: Meso-γ-scale convective systems observed by a 443-MHz wind-profiling radar with RASS in the Okinawa subtropical region. *J. Atmos. Solar-Terrestrial Phys.*, **73**, 996-1009.

Minda, H., F. A. Furuzawa, S. Satoh, and K. Nakamura, 2010: Convective boundary layer above a subtropical island observed by C-band radar and Interpretation using a cloud resolving model. *J. Meteor. Soc. Japan*, **88**, 285-312.

Mitchell, H., 2012: *Intercomparisons of 4D-Variational Assimilation and the Ensemble Kalman Filter*, *Mon. Wea. Rev.*, http://journals.ametsoc.org/page/Ensemble_Kalman_Filter.

Miyoshi, T., 2003: Development of a 3-dimensional variational assimilation system (JNoVA0), *Annual report of the Numerical Prediction Division of JMA*, **49**, 148-155. (in Japanese)

Murakami, M., 1997: The outer stratosphere analysis, *The report of the Numerical Prediction Division of the Japan Meteorological Agency*, **43**, 87-101. (in Japanese).

National Imagery and Mapping Agency 1997: Department of Defense World Geodetic System 1984, Its Definition and Relationships with Local Geodetic Systems, Third Edition, 4 July 1997, *NIMA Technical Report TR8350.2*.

Nishijima, M., Y. Honda, 2005: Assimilation of surface observation with nonhydrostatic 3DVAR, preprints. *Sixth International SRNWP-Workshop on Non-Hydrostatic Modelling*.

Ott, E., B. R. Hunt, I. Szunyogh, A. V. Zimin, E. J. Kostelich, M. Corazza, E. Kalnay, D. J. Patil, and J. A. Yorke, 2004: A local ensemble Kalman filter for atmospheric data assimilation. *Tellus*, **56A**, 415-428.

Owada, H., 2006: Predicted Satellite Images, *Meteorological Research Note 'Meteorology in Satellite'*, **212**, 105-120. (in Japanese)

Panofsky, H., 1949: Objective weather-map analysis. *J. Appl. Meteor.*, **6**, 386-392.

Park, S. K., and L. Xu (Eds.), 2009: *Data Assimilation for Atmospheric, Oceanic and Hydrologic Applications*, Springer, 475p.

Parrish, D. F, and J. C. Derber, 1992: The National Meteorological Center's spectral statistical-interpolation analysis system. *Mon. Wea. Rev.*, **120,** 1747-1763.

Purser, R. J., W. Wu, D. F. Parrish and N. M. Roberts, 2003: Numerical aspects of the application of recursive filters to variational statistical analysis. Part I: Spatially homogeneous and isotropic Gaussian covariances. *Mon. Wea. Rev.*, **131,** 1524-1535.

Richardson, L.F., 1922: *Weather Prediction by Numerical Process.* Cambridge University Press, Cambridge, 236p.

Saito, K., T. Kato, H. Eito, and C. Muroi, 2001: Documentation of the Meteorological Research Institute / Numerical Prediction Division Unified Nonhydrostatic Model. *Technical Reports of the Meteorological Research Institute*, Vol. 42, 133p.

Saito, K., T. Fujita, Y. Yamada, J. Ishida, Y. Kumagai, K. Aranami, S. Ohmori, R. Nagasawa, S. Kumagai, C. Muroi, T. Kato, H. Eito Y. Yamazaki, 2006: The operational JMA nonhydrostatic mesoscale model. *Mon. Wea. Rev.*, **134,** 1266-1298.

Saito, K., J. Ishida, K. Aranami, T. Hara, T. Segawa, M. Narita and Y. Honda, 2007: Nonhydrostatic atmospheric models and operational development at JMA. *J. Meteor. Soc. Japan.*, **85B**, 271-304.

Saito, K., 2012: The Japan Meteorological Agency nonhydrostatic model and its application to operation and research. *InTech, Atmospheric Model Applications*, 85-110. doi: 10.5772/35368.

Sasaki, Y., 1958: An objective analysis based on the variational method. *J. Meteor. Soc. Japan*, **36**, 77-88.

Sasaki, Y., 1970: Some basic formalisms in numerical variational analysis. *Mon. Wea. Rev.*, **98**, 875-883.

Seko, H., T. Kawabata, T. Tsuyuki, H. Nakamura, K. Koizumi, and T. Iwabuchi, 2004a: Impacts of GPS-derived water vapor and radial wind measured by Doppler radar on numerical prediction of precipitation, *J. Meteor. Soc. Japan*, **82**, 473-489.

Seko, H. T. Tsuyuki, M. Nishijima, T. Miyoshi, 2004b: An assimilation experiment of Doppler radial wind by JNoVA0 (NHM-3DVAR system) part 2. *Preprints of autumn meeting of Meteorological Society of Japan*, **86,** 391. (in Japanese).

Seko, H., Y. Shoji, F. Fujibe, 2007: Evolution and airflow structure of a Kanto thunderstorm on 21 July 1999 (the Nerima heavy rainfall event). *J. Meteor. Soc. Japan*, **85**, 455-477.

Seko, H., H. Yamauchi, O. Suzuki and K. Saito, 2009: Estimation of temporal variation of refractive index using C-band Doppler radar equipped with magnetron transmitter, *SOLA*, **5**, 145-148.

Seko, H., T. Tsuyuki, K. Saito, and T. Miyoshi, 2013: Development of a Two-way Nested LETKF System for Cloud Resolving Model, *Data assimilation workshop*, http://daweb.ism.ac.jp/DAWS/workshopJan2013.html.

Shoji, Y., H. Nakamura, T. Iwabuchi, K. Aonashi, H. Seko, K. Mishima, A. Itagaki, R. Ichikawa, and R. Ohtani, 2004: Observation Improvement in GPS analysis of slant path delay by stacking one-way postfit phase residuals. *J. Meteor. Soc. Japan*, **82,** 301-314.

Shoji, Y., 2009: A Study of near real-time water vapor analysis using a nationwide dense GPS network of Japan. *J. Meteorol. Soc. Japan*, **87**, 1–18.

Shoji, Y., 2013: Retrieval of Water Vapor Inhomogeneity using the Japanese Nationwide GPS Array and its Potential for Prediction of Convective Precipitation. *J. Meteor. Soc. Japan*, **91**, 43-62.

Snyder, C. and F. Zhang, 2003: Assimilation of simulated Doppler radar observations with an ensemble Kalman filter. *Mon. Wea. Rev.*, **131**, 1173–1185.

Sokol, Z. and D. Rezacova, 2009: Assimilation of the radar-derived water vapour mixing ratio into the LM COSMO model with a high horizontal resolution. *Atmospheric Research*, **92**, 331–342.

Sommeria, G.., 1976: Three0dimensional simulation of turbulent processes in an undisturbed trade wind boundary layer. *J. Atmos. Sci.*, **33**, 216-241.

Sugi, M., K. Kuma, K. Tada, K. Tamiya, N. Hasegawa, T. Iwasaki, S. Yamada and T. Kitade, 1990: Description and performance of the JMA operational global spectral model (JMA-GSM88). *Geophys. Mag.*, **43**, 105-130.

Sun, J. and A. Crook, 1997: Dynamical and microphysical retrieval from doppler radar observations using a cloud model and its adjoint. Part I: Model development and simulated data experiments. *J. Atmos. Sci.*, **54,** 1642–1661.

Sun, J. and A. Crook, 1998: Dynamical and Microphysical Retrieval from Doppler radar observations using a cloud model and its adjoint. Part II: Retrieval experiments of an observed Florida convective storm. *J. Atmos. Sci.*, **55**, 835–852.

Sun, J., 2005: Initialization and numerical forecasting of a supercell storm observed during STEPS, *Mon. Wea. Rev.*, **133**, 793-813.

Sun, J. and Y. Zhang, 2008: Analysis and prediction of a squall line observed during IHOP using multiple WSR-88D observations. *Mon. Wea. Rev.*, **136**, 2364–2388.

Swinbank, R., V. Shutyaev, W. A. Lahoz, 2003: *Data Assimilation for the Earth System*, Kluwer Academic Publishers, 377pp. (NATO science series IV: Earth and Environmental Sciences)

Tsuyuki, T., 1996a: Variational data assimilation in the tropics using precipitation data. part I: Column model. *Meteor. Atmos. Phys.*, **85,** 255–276.

Tsuyuki, T., 1996b: Variational data assimilation in the tropics using precipitation data. part II: 3d model. *Mon. Wea. Rev.*, **124,** 2545–2561.

Tsuyuki, T., and T. Kawabata (Eds.), 2008: *Data assimilation on Meteorology*, Meteorological Society of Japan, 277p. (Meteorological Research Note, Vol. 217) (in Japanese)

Wang, H., T. Auligné, H. Morrison, 2012: Impact of Microphysics Scheme Complexity on the Propagation of Initial Perturbations. *Mon. Wea. Rev.*, **140**, 2287‑2296.

Wang, H., J. Sun, X. Zhang, X.-Y. Huang, and T. Auligné, 2013: Radar data assimilation with WRF 4D-Var: Part I. System development and preliminary testing. *Mon. Wea. Rev.*, **141**, 2224‑2244.

Weckwerth, T.M., H. V. Murphey, C. Flamant, J. Goldstein, C.R. Pettet, 2008: An Observational Study of Convection Initiation on 12 June 2002 during IHOP_2002. *Mon. Wea. Rev.*, **136**, 2283‑2304.

Whitaker, J. S. and T. M. Hamill, 2002: Ensemble data assimilation without perturbed observations. *Mon. Wea. Rev.*, **130**, 1913-1924.

Xiao, Q., Y.-H. Kuo, J. Sun, W.-C. Lee, and D. M. Barker, 2007: An approach of radar reflectivity data assimilation and its assessment with the inland QPF of Typhoon Rusa (2002) at landfall. *J. Appl. Meteor. Climatol.*, **46**, 14–22.

Xu, Q., 1996: Generalized adjoint for physical processes with parameterized discontinuities. part I: Basic issues and heuristic examples. *J. of Atmos. Sci.*, **53,** 1123–1142.

Xue, M., M. Tong, and K. K. Droegemeier, 2006: An OSSE framework based on the ensemble square root Kalman filter for evaluating the impact of data from radar networks on thunderstorm analysis and forecasting. *J. Atmos. Oceanic Technol.*, **23**, 44–66.

Zou, X., Navon, I. M., Berger, M., Phua, Paul K. H., Schlick, T. and Le Dimet, F. X., 1993: Numerical experience with limited-memory quasi-Newton and truncated Newton methods. *SIAM J. on Optimization*, **3,** 582-608.

Zou, X. and Y. H. Kuo, 1996: Rainfall assimilation through and optimal control of initial and boundary conditions in a limited-area mesoscale model. *Mon. Wea. Rev.*, **124**, 2859–2882.

Zupanski, M., 2005: Maximum likelihood ensemble filter: Theoretical aspects. *Mon. Wea. Rev.,* **133**, 1710–1726.

Publication list

Note: This thesis is based on articles marked with an asterisk (No. 2, 4, 7) of the following list. Each article is listed in chronological order.

Refereed papers

1. Seko, H., <u>T. Kawabata</u>, T. Tsuyuki, H. Nakamura, K. Koizumi and T. Iwabuchi, 2004: Impacts of GPS-derived water vapor and radial wind measured by Doppler radar on numerical prediction of precipitation, *J. Meteor. Soc. Japan*, **82**, 473-489.

2. * <u>Kawabata, T.</u>, H. Seko, K. Saito, T. Kuroda, K. Tamiya, T. Tsuyuki, Y. Honda and Y. Wakazuki, 2007: An Assimilation and forecasting experiment of the Nerima heavy rainfall with a cloud-resolving nonhydrostatic 4-dimensional variational data assimilation system. *J. Meteor. Soc. Japan*, **85**, 255-276. doi: http://dx.doi.org/10.2151/jmsj.85.255

3. Mikami, A., <u>T. Kawabata</u>, S. Satoh, J. Furumoto, S. Nagai, Y. Murayama and T. Tsuda, 2011: Meso-γ-scale convective systems observed by a 443-MHz wind-profiling radar with RASS in the Okinawa subtropical region. *J. Atmos. Solar-Terrestrial Phys*, **73**, 996-1009.

4. * <u>Kawabata, T.</u>, T. Kuroda, H. Seko, and K. Saito, 2011: A cloud-resolving 4dvar assimilation experiment for a local heavy rainfall event in the Tokyo metropolitan area. *Mon. Wea. Rev.*, **139**, 1911-1931. doi: http://dx.doi.org/10.1175/2011MWR3428.1

5. <u>Kawabata, T.</u>, M. Kunii, K. Bessho, T. Nakazawa, N. Kohno, Y. Honda, K. Sawada, 2012: Reanalysis and reforecast of typhoon Vera (1959) using a mesoscale four-dimensional variational assimilation system. *J. Meteor. Soc. Japan*, **90**, 467-491. doi: http://dx.doi.org/10.2151/jmsj.2012-403

6. Ito, K., <u>T. Kawabata</u>, T. Kato, Y. Honda, Y. Ishikawa, and T. Awaji, 2013: Simultaneous optimization of air-sea exchange coefficients and initial conditions near a tropical cyclone using JNoVA. *J. Meteor. Soc. Japan*, **91**, 337-353.

7. * <u>Kawabata, T.</u>, Y. Shoji, H. Seko, and K. Saito, 2013: A numerical study on a mesoscale convective system over a subtropical island with 4d-var assimilation of GPS slant total delays. *J. Meteor. Soc. Japan*, **91**, 705-721.

Unrefereed articles

8. <u>Kawabata, T.</u>, Y. Honda, K. Tamiya, K. Aonashi, T. Tsuyuki, K. Koizumi, 2003: The observation assimilation experiment by using NHM-4DVAR – The development report of the JNoVA-4DVAR (2nd) -. *Preprints of autumn meeting of Meteorological Society of Japan*, **84,** 420. (in Japanese).

9. <u>Kawabata, T.</u>, H. Seko, T. Kuroda, Y. Wakatsuki, Y. Honda, K. Tamiya, K. Aonashi, Y. Shoji, K. Saito, T. Tsuyuki, 2004: Development of a cloud resolving 4DVAR data assimilation system

based on the JMA non-hydrostatic model. *Proc. Remote Sensing of the Atmosphere, ocean, Environment, and Space.* **5661**, 46-56.

10. Kawabata, T., H. Seko, T. Kuroda, Y. Wakatsuki, Y. Honda, K. Tamiya, K. Aonashi, Y. Shoji, K. Saito, and T. Tsuyuki, 2005: A cloud resolving 4D-Var data assimilation system based on the JMA non-hydrostatic model. *CAS/JSC WGNE Research Activities in Atmospheric and Oceanic Modelling*, **35**, 1.21-1.22.

11. Kawabata, T., 2008a: A study on deep convections using a cloud-resolving data assimilation system, *Meteorological Research Note*, **217**, 207-223. (in Japanese)

12. Kawabata, T., H. Seko, T. Kuroda, and K. Saito, 2008b: An assimilation experiment of a heavy rainfall event around Tokyo with a cloud-resolving nonhydrostatic 4D-Var assimilation system, *CAS/JSC WGNE Research Activities in Atmospheric and Oceanic Modelling*, **38**, 1.13-1.14.

13. Bessho, K., T. Nakazawa, T. Kawabata, H. Kamahori, N. Kohno, E. Shindo, M. Kunii, M. Hara, K. Takahashi, A. Ebita, Y. Ohta, S. Kobayashi, M. Moriya, Y. Honda, and K. Sawada, 2010: Re-analysis/forecast of Typhoon Vera project: ReVera. *Tenki*, **57**, 57-64. (in Japanese)

14. Kawabata, T., J. Furumoto, S. Satoh, 2011a: The impact of RASS observations on a rainfall forecast in the Okinawa heavy rainfall event. *Preprints of autumn meeting of Meteorological Society of Japan*, **99,** 170. (in Japanese).

15. Kawabata, T., Y. Shoji, H. Seko, K. Saito, 2011b: An assimilation experiment of GPS-derived water vapor observations on a local heavy rainfall event, *CAS/JSC WGNE Research Activities in Atmospheric and Oceanic Modelling*, **41**, 1.15-1.16.

16. Kawabata, T., K. Saito, H. Iwai, Y. Shoji, H. Seko, 2013a: Assimilation experiment on a local heavy rainfall event using Doppler lidar observations, *93rd American Meteorological Society Annual Meeting*.

17. Kawabata, T., and M. Kunii, 2013b: Re-forecast of Typhoon Vera (1959), *Meteorological Research Note*, **227**, 54-66. (in Japanese)